國立臺灣大學理學院地理環境資源學系

碩士論文

Department of Geography

College of Science

National Taiwan University

Master's Thesis

利用 PSInSAR 監測臺灣西南部關鍵基礎設施相關之地表變形

Using PSInSAR to monitor the surface deformation of critical infrastructure in SW Taiwan

蔣友維

You-Wei Jiang

指導教授：莊昀叡 博士

Advisor: Ray Y. Chuang, Ph.D.

中華民國 113 年 1 月

January, 2024

doi: 10.6342/NTU202400130

國立臺灣大學碩士學位論文
口試委員會審定書
MASTER'S THESIS ACCEPTANCE CERTIFICATE
NATIONAL TAIWAN UNIVERSITY

利用 PSInSAR 監測臺灣西南部關鍵基礎設施相關之地表變形

Using PSInSAR to monitor the surface deformation of critical infrastructure in SW Taiwan

本論文係 蔣友維（學號：R10228014）在國立臺灣大學地理環境資源學系完成之碩士學位論文，於民國 112 年 7 月 24 日承下列考試委員審查通過及口試及格，特此證明。

The undersigned, appointed by the Department / Institute of Geography on 24 July 2023 have examined a Master's thesis entitled above presented by You-Wei, Jiang (Student ID: R10228014) candidate and hereby certify that it is worthy of acceptance.

口試委員 Oral examination committee:

莊昀叡　　李國慶　　許珮琦

（指導教授 Advisor）

陳柏春　　曾國欣

系主任/所長 Director: 黃瑞仁

doi: 10.6342/NTU202400130

誌謝

感謝本研究的指導老師莊昀叡老師。感謝擔任口試委員的陳松春老師、張午龍老師、景國恩老師以及曾國欣老師。感謝科技部的臺灣西南部泥貫入體活動速率之機制及其之社會衝擊研究－子計畫五：偵測台灣西南部快速地表變形於基礎設施與區域衝擊之研究支持本研究，計畫編號：MOST 110-2116-M-002-009。感謝國科會的建構 SAR 衛星多時序與近即時海岸帶整合監測平台－建構 SAR 衛星多時序與近即時海岸帶整合監測平台(2/3)支持本研究，計畫編號：NSTC 112-2119-M-008-009。感謝地質調查所的重要活動斷層地區地表變形觀測與斷層潛勢評估（2/2）支持本研究，計畫編號：B11130。

感謝 ESA Sentinel-1 衛星與 NASA ASF 平台提供的雷達衛星影像。感謝 ESA Copernicus 的 30 米數值高程模型。感謝經濟部地質調查測繪之活動斷層與構造。感謝臺灣地震模型測繪之活動斷層與構造。感謝開源功能的 Interferometric Synthetic Aperture Radar Scientific Computing Environment (ISCE)、Stanford Method for Persistent Scatterers (StaMPS/ MTI)、The Generic Mapping Tools (GMT)以及 QGIS 協助本研究。感謝 Matlab 協助本研究。

本研究階段性研究成果曾發表於以下研討會：2022 臺灣地球科學聯合學術研討會、2022 中華民國測地學會年會暨學術研討會、2023 中華民國地理學會年會暨國際學術研討會、中華民國地球物理學會與中華民國地質學會 112 年年會暨學術研討會、2023 Japan-Taiwan Workshop on Crustal Dynamics、2023 中華民國測地學會學術研討會。

此外，也要特別感謝在這段時間幫助過我的所有人，包括研究室成員林耕霈學長、豐傑、子昕、立學、昭蓉、荃敏、靜儀、向倢、冠至、聿修、皓媜、佑璇、耀萱、李旻、勝煒、正標，還有睿桓、郁安、允文、恩如、皓雲、佩容、學國、郁霖等友人，最後是最支持我的父母以及家人們，謝謝你們。

doi: 10.6342/NTU202400130

摘要

台灣造山帶位於弧陸碰撞帶，由菲律賓海板塊的呂宋島弧向西以及歐亞板塊向東斜向碰撞在此造成褶皺逆衝帶，形成一系列南北走向的活動斷層。台灣西南部位於褶皺逆衝帶的前緣位置，並且在 2016 年受到美濃地震的影響，使得此區域的斷層活動變得更加不穩定。台灣西南部境內包含台南與高雄都會區，有台灣高鐵公司（以下稱「高鐵」）鐵路、台灣鐵路管理局（以下稱「台鐵」）鐵道以及國道高速公路通過。近年來也陸續設立了多個產業園區以及數條預計建設的交通設施。而先前的研究透過 GNSS 等測地資料發現，在台灣西南部跨斷層兩側有明顯速度落差，支持現今的地表斷層潛移的現象，跨越活動斷層的交通設施與產業園區就可能受到跨斷層速度差受到影響甚至是破壞。因此為了要獲取台灣西南部的速度場，本研究使用歐洲太空總署（European Space Agency, ESA）的 Sentinel-1A 的 SAR 影像，在升軌方向使用 146 幅影像，觀測時間從 2016 年 3 月到 2021 年 11 月；在降軌方向使用 130 張影像，觀測時間從 2016 年 5 月到 2022 年 2 月。我們使用永久散射體雷達干涉（Persistent Scatterer InSAR, PSInSAR）的 StaMPS/MTI (Stanford Method for Persistent Scatterers/ Multi-Temporal InSAR)演算法，針對目標區域的活動斷層造成的地表變形以及關鍵基礎設施的變形製作時間序列觀測資料。本研究結果顯示在中央地質調查所的後甲里斷層兩側的速度落差在垂直方向上約為 3~6 毫米/年，呈現由北向南遞增的情形；在車瓜林斷層兩側的速度落差在東西方向上約為 4~8 毫米/年；而在台灣地震模型（Taiwan Earthquake Model, TEM）右昌斷層兩側的速度落差在東西方向上約為 5 毫米/年。並在斷層兩側的位移在時間序列上也可以明顯見到相反的變形趨勢，足見這些斷層可能存在斷層潛移的情形。針對關鍵基礎設施高鐵沿線以及台鐵沿線，在部分跨越活動斷層路段兩側也同樣取得時間序列變形趨勢。在高鐵沿線變形最大處即跨越地調所車瓜林斷層處，達到橫向水平位移的容許規範約為 7 年；而台鐵沿線變形最大處即跨越右昌斷層處，達到縱向水平位移的容許規範約為 10 年；國道 7 號等規劃路線，其沿線跨越斷層

doi: 10.6342/NTU202400130

處的變形量也將在 10 年內達到 H 等級。產業園區類的基礎設施，雖然不像交通系統容易受到地表變形立即的危害，但部分園區接近有潛移活動的活動斷層敏感區，亦需要更多的觀測來留意。本研究比對前人針對斷層特性的研究，在斷層處的變形趨勢皆符合，並且也與前人利用測地技術測得之可能存在斷層潛移之結果符合。因此，本研究建議未來在台灣西南部地區活動斷層附近設置之關鍵基礎設施能更加留意活動斷層活動性帶來的影響。

關鍵字：永久散射體差分干涉技術、關鍵基礎設施、台灣西南部、活動斷層

doi: 10.6342/NTU202400130

Abstracts

The Taiwan mountain belt features many active faults resulting from the oblique collision between the two tectonics (Suppe, 1984). Geodetic observations in previous studies show that sharp velocity gradients across active faults in SW Taiwan, suggesting the presence of surface fault creep. Synthetic Aperture Radar (SAR), which is an active system that transmits microwaves to surface targets and receives backscatters from them, has a lot of benefits such as cloudy-free, day-and-night monitoring, and all-weather detection. In this study, SAR images derived from the ESA's Sentinel-1A satellite were used. 166 SAR images from March 9, 2016, to November 14, 2021, in the ascending direction (ASC) and 133 SAR images from May 10, 2016, to February 8, 2022, in the descending direction (DES), which cover the whole study area are used to detect surface deformation. I use the PSInSAR algorithm of StaMPS/MTI to create time series data of surface deformation and target deformation of the critical infrastructure. At the maximum deformation place along the Taiwan High Speed Rail Corporation (THSR) railroad, which crosses the Chekualin fault, will reach the allowable level for lateral horizontal displacement within 7 years. Along the Taiwan Railway Administration MOTC. (TR) railroad, at the maximum deformation place, which crosses the Youchang fault, will reach the allowable level for longitudinal horizontal displacement within 10 years. For planned routes like National Highway No. 7, the deformation at locations where active fault

doi: 10.6342/NTU202400130

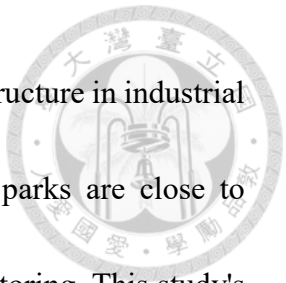

crosses is expected to reach Class H within 10 years. Although infrastructure in industrial parks is not affected by surface deformations immediately, some parks are close to sensitive areas with potential active fault creep, requiring more monitoring. This study's findings are consistent with previous research on fault characteristics and are in line with the results obtained through geodetic techniques indicating potential fault creep. Therefore, it is recommended that future critical infrastructure near active fault zones in southwestern Taiwan should pay more attention to the impact of fault creep.

Keywords: PSInSAR, Critical infrastructures, SW Taiwan, Active faults

doi: 10.6342/NTU202400130

Contents

doi: 10.6342/NTU202400130

doi: 10.6342/NTU202400130

doi: 10.6342/NTU202400130

List of tables

doi: 10.6342/NTU202400130

List of Figures

doi: 10.6342/NTU202400130

doi: 10.6342/NTU202400130

doi: 10.6342/NTU202400130

doi: 10.6342/NTU202400130

doi: 10.6342/NTU202400130

doi: 10.6342/NTU202400130

Chapter 1 Introduction

1.1 Motivations

The Taiwan mountain belt features many active faults resulting from the oblique collision between the two tectonics (Suppe, 1984). This collision produces a series of N–S trending active fold-and-thrust belt with destructive earthquakes (Shyu et al., 2005; Lin et al., 2010; Ching et al., 2011). South Western (SW) Taiwan at the southwestern foreland of the Taiwan fold-thrust belt, which has a series of active faults (Fig. 1.1), is influenced by the 2016 Meinong earthquake showing that fault activity in this region has become more unstable (Huang et al., 2016). Within SW Taiwan, it encompasses the metropolitan areas of Tainan and Kaohsiung, traversed by the THSR railroad, TR railroad, and the National Freeway network. In recent years, multiple industrial parks and several planned transportation facilities have also been established in this area, such as National Freeway no.7, Kaoping Expressway, and THSR extending routine to Pingtung (高鐵延伸屏東新闢路線可行性評估，2020) (Fig. 1.2).

In SW Taiwan, active faults have shown complicated deformation patterns based on geodetic observations (Huang et al., 2006, 2009; Ching et al., 2007, 2011; Huang et al., 2016). Rapid surface velocities and sharp velocity gradients across some active faults suggest the presence of surface fault creep. There are many active faults in SW Taiwan, including the Houchiali fault, Chekualin fault, Chishan fault, and Hsiaokangshan fault

doi: 10.6342/NTU202400130

(林啟文等, 2000). When the active faults with creeping, which pass through critical infrastructures and population-dense areas, the accumulation of damage in a structure will cause a change in the dynamic characteristics of the structure (Rytter, 1993); for example, the Chihshang fault in eastern Taiwan with a total 4.8 mm/yr velocity change across a fault creeping site with broken embankment (Lee et al., 2003), the Hayward fault in California, USA with a 2 mm/yr velocity difference across fault which causes street displacement (Lanari et al., 2007), and the Central San Andreas fault in California, USA with a creep rate 2.5 ± 0.2 cm/yr, which causes the potential damage on the fault-crossing canal (Tymofyefyeva et al., 2019; Scott, 2021).

doi: 10.6342/NTU202400130

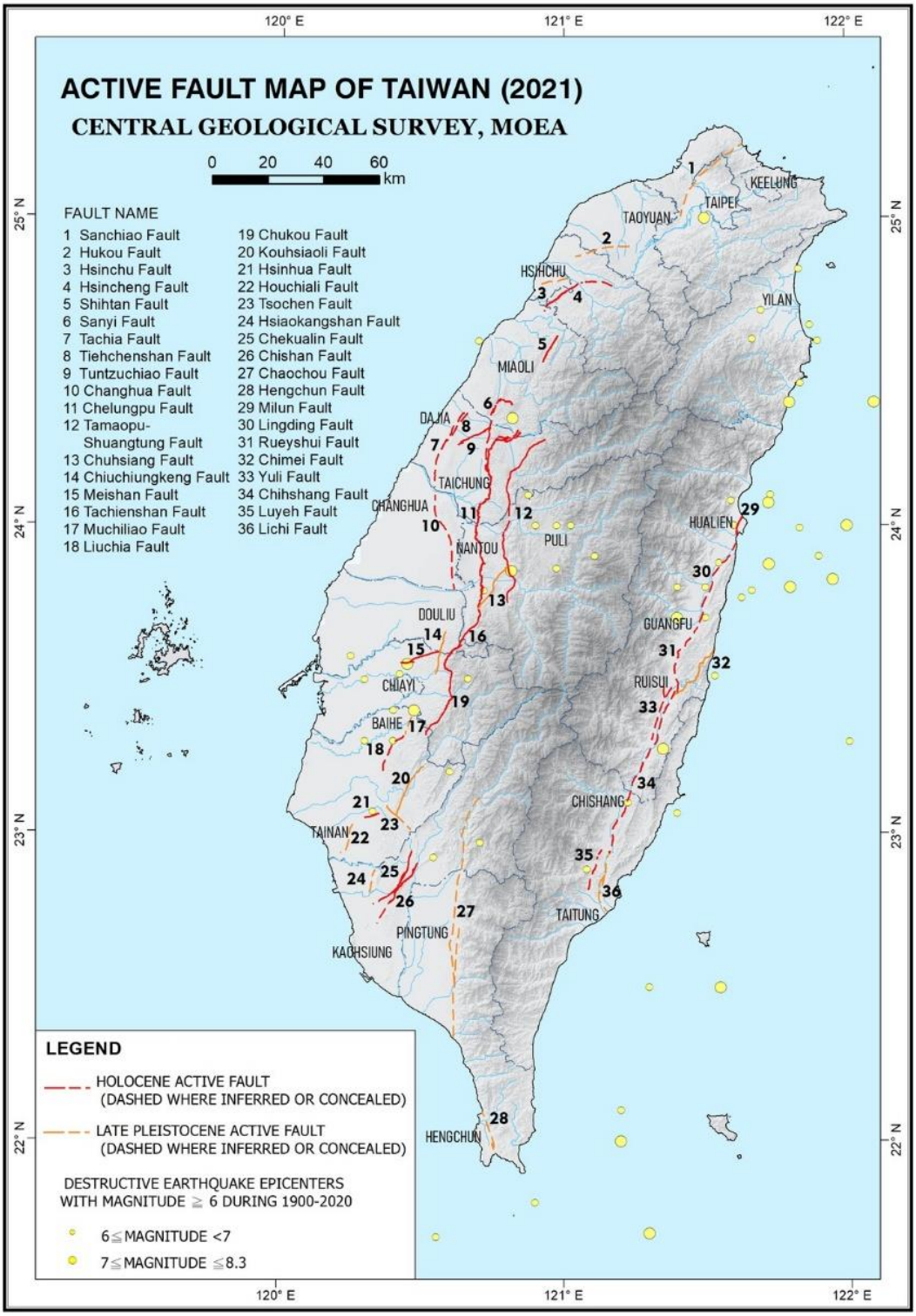

Fig. 1.1. Active fault map of Taiwan published in 2021. Different colors represent different types of active faults Central Geological Survey, CGS).

doi: 10.6342/NTU202400130

1.2 Purposes

Using creepmeter and GNSS observations were the common way to estimate creeping motion in the past; however, these traditional methods can only provide sparse point data. This will cause greater errors during interpolation when we try to get dense data. In recent years, the form of radar processing method called Synthetic Aperture Radar (SAR) technique, which can be used to produce wide-range observations and use the PSInSAR algorithm to pick a more stable point relatively to grab more stable scatterers on the surface, such as roads, buildings, and bridges. Through this method, we can estimate surface displacements in line of sight (LOS) of right-looking satellite mean velocity in a specific period and do decomposition to get uplift rates around critical infrastructure in SW Taiwan.

In this study, I calculated velocity difference across active structures, which have large surface deformation, along transportation systems and industrial parks to classify the allowable deformation time of these critical infrastructures in SW Taiwan.

doi: 10.6342/NTU202400130

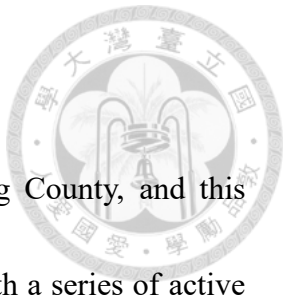

1.3 Study area

SW Taiwan spans approximately from Tainan City to Pingtung County, and this region is located at the southwestern front of the western foothill with a series of active faults. A lot of critical infrastructures were built, such as the THSR railroad, TR railroad, National Freeway, Science Park, Industrial Park, and some planned routines. These critical infrastructures are very close to or transected by active faults (Fig 1.2; Fig. 1.3). Except of these existing humanmade buildings, there are other infrastructure under planning (e.g., Freeway no. 7, THSR extending plan). There are more detailed descriptions of those active faults and the factors of deformation in the next chapter.

Except for the active faults, there are other tectonic features such as mud diapirs and mud volcanoes in this area. A mud diapir is defined as an intrusive structure marked by the slow upward migration of clay-rich sediments and fluid emissions (Kopf, 2002; Chen et al., 2014). Cone-shaped mud volcanoes represent the last manifestation of diapirism, which is a well-known geological phenomenon near the area of ongoing collisional tectonics (Brown and Westbrook, 1988; Brown, 1990; Pérez-Belzuz et al., 1997; Kopf, 2002; Chen et al., 2014). Ching et al. (2016) found that the GNSS geodetic observations here do not fit their 2D dislocation model. Thus, they inferred the mechanism of vertical deformation is not fully contributed from active faults but an onshore mud diapir (Fig. 1.4). The distribution of these onshore mud tectonics (Fig. 1.5) is near the critical

doi: 10.6342/NTU202400130

infrastructures such as THSR railroad, Dashe Park, and Nanzi Park so that can cause the damage to infrastructures due to its active mud flow underground (Tanaka et al., 2020; Lo et al., 2023).

doi: 10.6342/NTU202400130

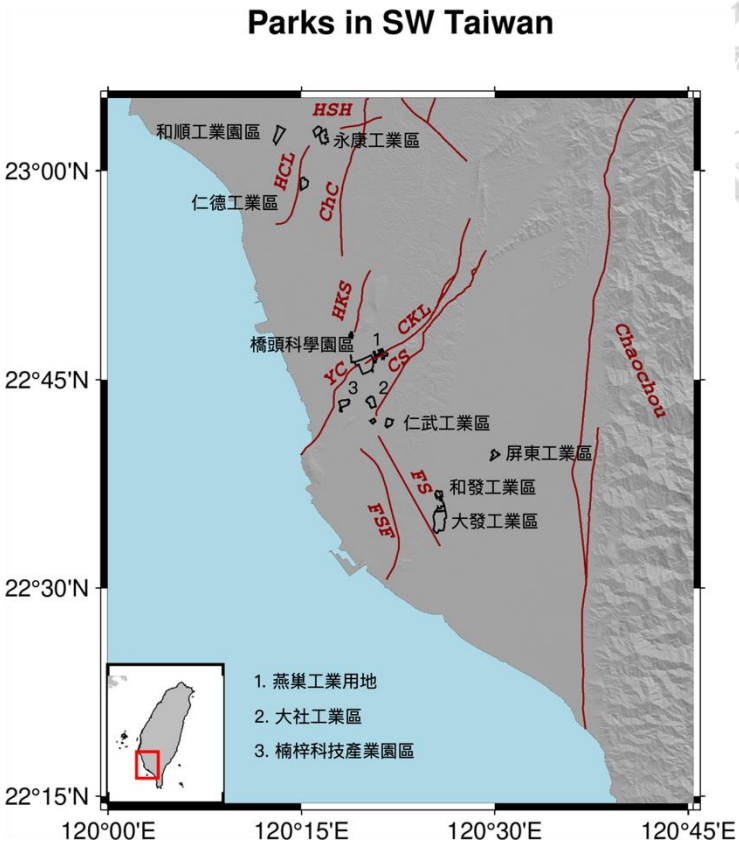

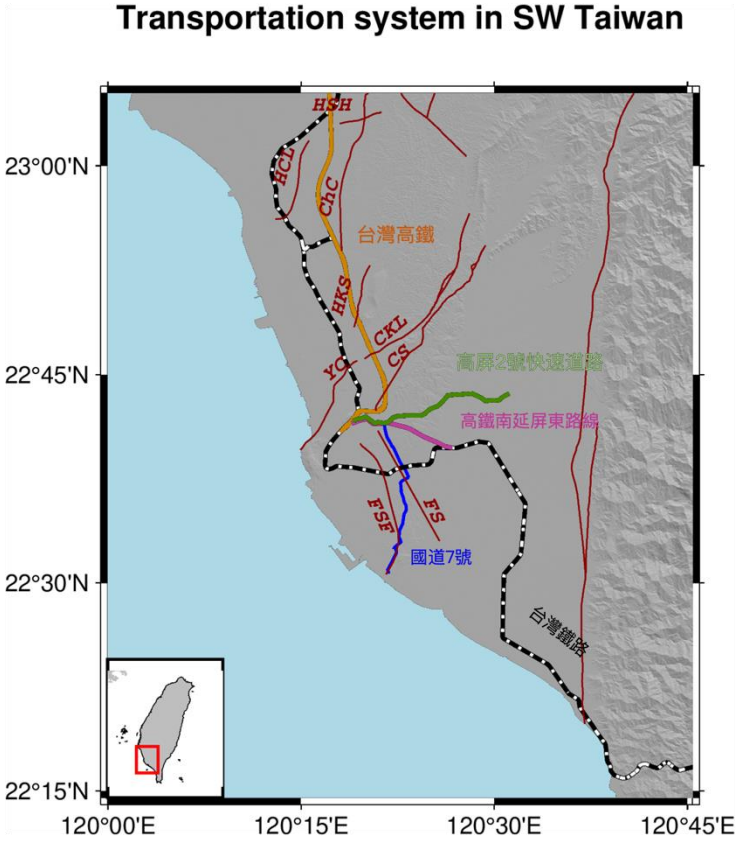

Fig. 1.2. Critical Infrastructure in SW Taiwan (Chinese ver.)

doi: 10.6342/NTU202400130

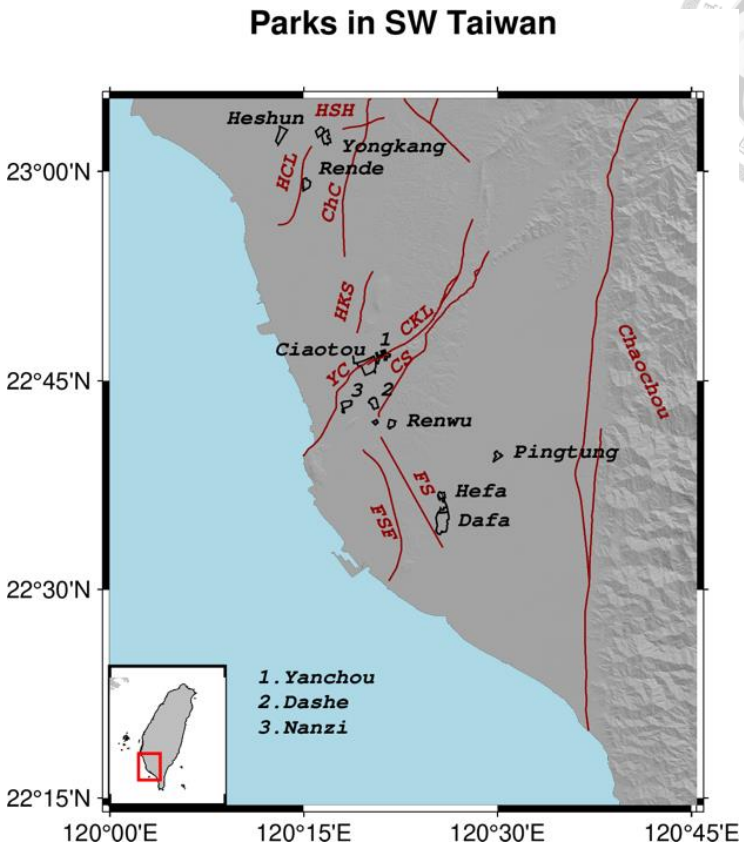

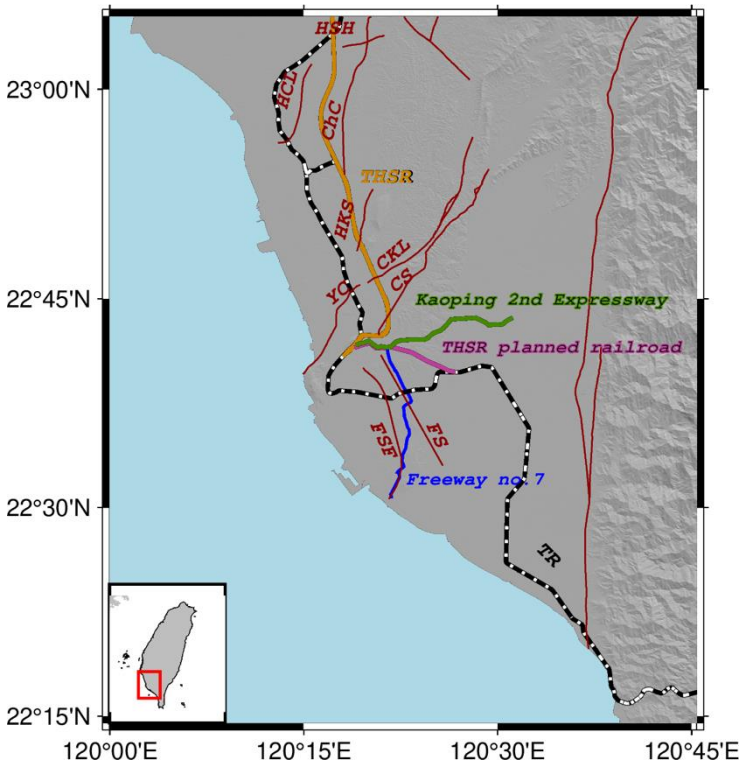

doi: 10.6342/NTU202400130

Fig. 1.3. Critical Infrastructure in SW Taiwan. Left is Science Parks and Industrial Parks. Right is linear (transportation) systems. The orange line is THSR railroad. The black line with white dot is TR railroad. The black polygon is Science Park and Industrial Park. The blue line is planning route of Freeway No.7. The dark red line is active structures. HSH is Hsinhua fault, ChC is Chungchou fault, HCL is Houchiali fault, HSK is Hsiaokangshan fault, CKL is Chekualin fault, YC is Youchang fault, FS is Fengshan fault, FSF is Fengshan hill frontal structure, and CS is Chishan fault.

doi: 10.6342/NTU202400130

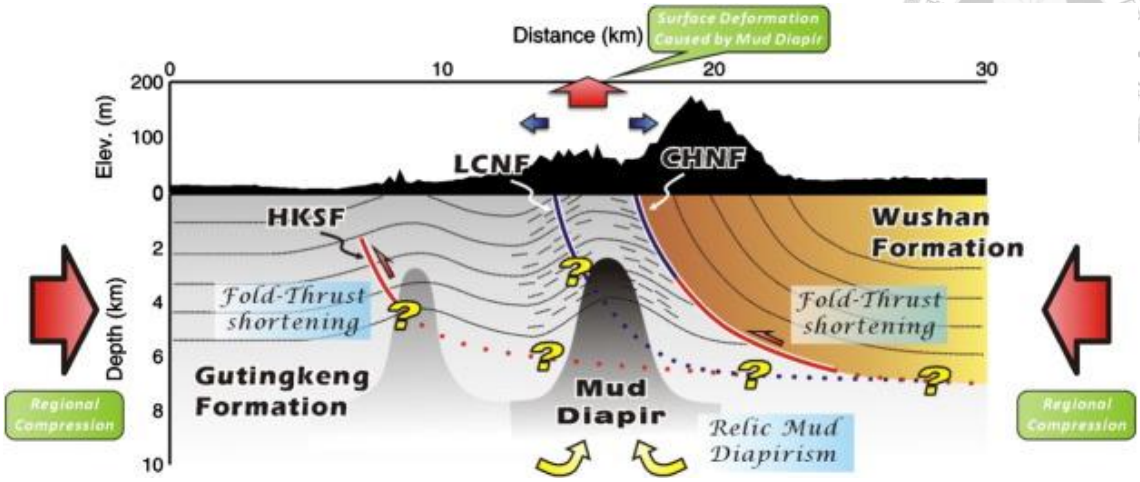

Fig. 1.4. 2D tectonic kinematic model for SW Taiwan (Ching et al., 2016).

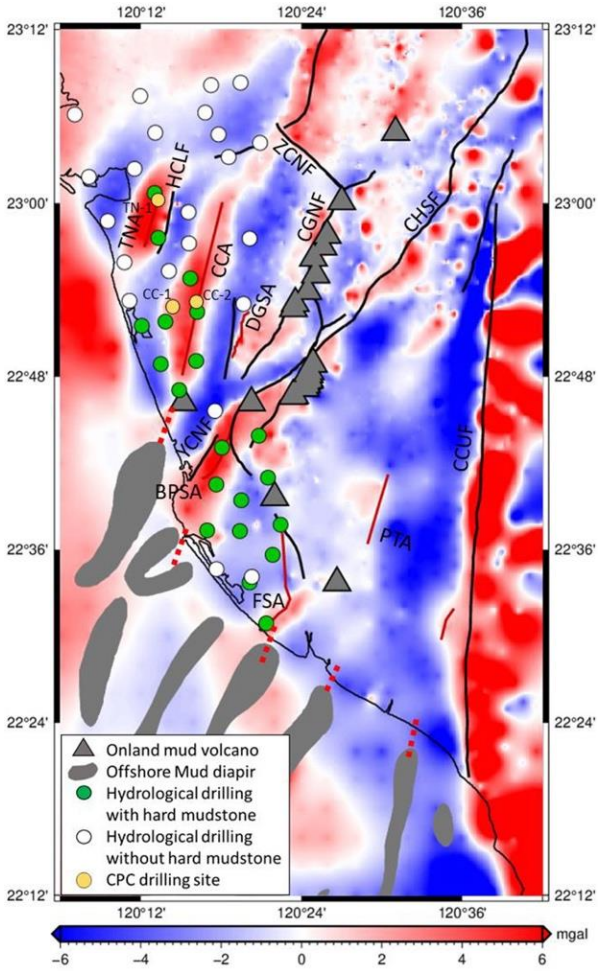

Fig. 1.5. The distribution of mud volcanoes onshore and mud diapirs offshore superimposed on the 0-5 km residual gravity anomaly map (Lo et al., 2023) and critical infrastructures in SW Taiwan.

doi: 10.6342/NTU202400130

Chapter 2 Literature review

2.1 Geology setting

This study suggests the presence of surface fault creep based on previous studies, which showed the sharp velocity gradients and complicated deformation patterns in SW Taiwan on the basis of geodetic result. The following section introduces the geology and faults of the study area.

Taiwan is on the site of the collision belt between the Philippine Sea plate and the Eurasian plate (Fig. 2.1) (Suppe, 1984; Ching et al., 2007). The Philippine Sea plate is advancing northwestward at a rate of 82 mm/yr towards the Eurasian plate. (Yu et al., 1997). SW Taiwan is located at the fold-and-thrust belts, consisting of many active faults. This region is one of the areas with the most active structures activity (Ching et al., 2011). The vertical velocities from the Western Foothills to the Central Range in SW Taiwan had been estimated to uplift rate of 10 to 20 mm/yr (Ching et al., 2007). Because the Eurasian plate performed subduction to the Philippine Sea plate, there were a series of N-S trending faults in this area. The active faults include the Houchiali fault, the Hsiaokangshan fault, the Chishan fault, the Chaochou fault, the Youchang fault, the Chungchou fault, and the Fengshan fault from east to west in this area (Shyu et al., 2016; Shyu et al., 2020).

doi: 10.6342/NTU202400130

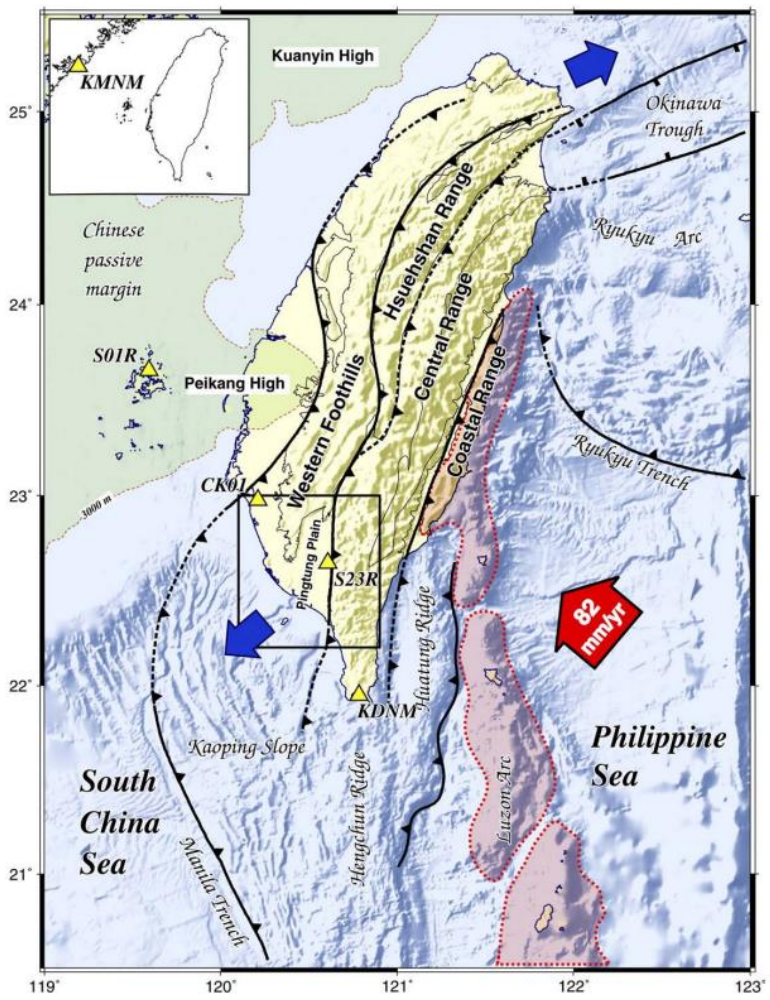

Fig. 2.1. The geotectonic framework of Taiwan (Yu et al., 1997; Ching et al. 2007).

doi: 10.6342/NTU202400130

2.1.1 Stratigraphy of SW Taiwan

The stratigraphy we used here is obtained from stratigraphic columns and reflection profiling data (Chi, 1981; Wu et al., 2002; Huang et al., 2004). The stratigraphy in our study area is as following (Fig. 2.2; Table 2.1):

(1) Liushuang Formation

It is mainly composed of dark gray to bluish-gray mudstone and interbedded shale with sandstone and siltstone. The thickness is approximately 1040 meters (何春蓀，1975).

(2) Erhchuangchi Formation

It is composed of interbedded shale and fine to medium-grained sandstone. The sandstone contains abundant marine mollusk fossils and fragments of driftwood with an exposed thickness is about 750 meters (何春蓀，1975).

(3) Gutingkeng Formation

This formation can be divided into upper and lower layers. The upper layer is primarily composed of dark gray, fine-grained sandy siltstone or sandy mudstone, with localized thin lenses of convex-shaped sandstone layers. The thickness is about 540 to 1000 meters, and it contains abundant fossils of soft-bodied animals (孫習之等，1960). The lower layer has a similar composition to the upper layer but has better sorting and the thickness is about 4000 meters.

doi: 10.6342/NTU202400130

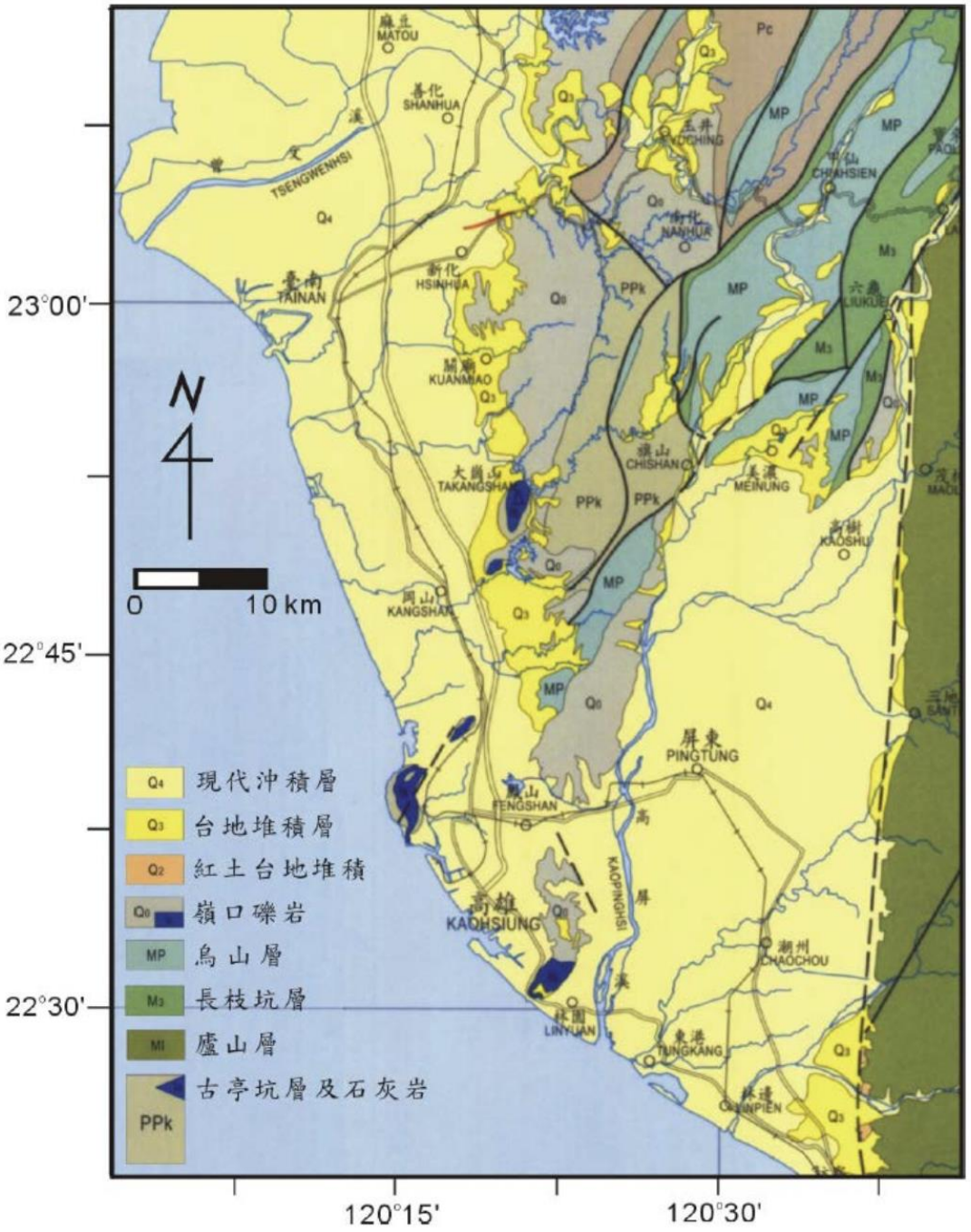

Fig. 2.2. The stratigraphy map in SW Taiwan (Central Geological survey, 2002).

doi: 10.6342/NTU202400130

Table 2.1: Stratigraphy in SW Taiwan (Chi, 1981; Wu et al., 2002; Huang et al., 2004). Fm. = Formation, Sh. = Shale, Ss. = Sand stone.

Time		Tainan area	Kaohsiung area
Period	Epoch		
Quarternary	Holocene	Terrace deposit	Terrace deposit
	Pleistocene	Liushuang Fm.	Liushuang Fm.
		Erhchuangchi Fm.	Erhchuangchi Fm.
		Yuching Sh.	
		Chinmen Ss.	Gutingkeng Fm.
		Peiliao Sh.	
Tertiary	Pliocene	Chutou Chi Fm.	
		Maupu Sh.	
		Ailiaochiao Fm.	
		Yenshui keng Sh.	
		Tangen Shan Ss.	Mucha Fm.
	Miocene	Chanchih Keng Fm.	
		Hunghuatzu Fm.	
		Shanmin Sh.	

doi: 10.6342/NTU202400130

2.1.2 Active faults

According to the map of active fault map of Taiwan published in 2021 derived by Central Geological Survey, MOEA (Fig. 1.1), the active faults can be divided into the Holocene active faults (第一類活動斷層) and the Late Pleistocene active faults (第二類活動斷層). We also use Taiwan Earthquake Model (TEM) fault map (Fig. 2.3), the main faults in this study area are included below:

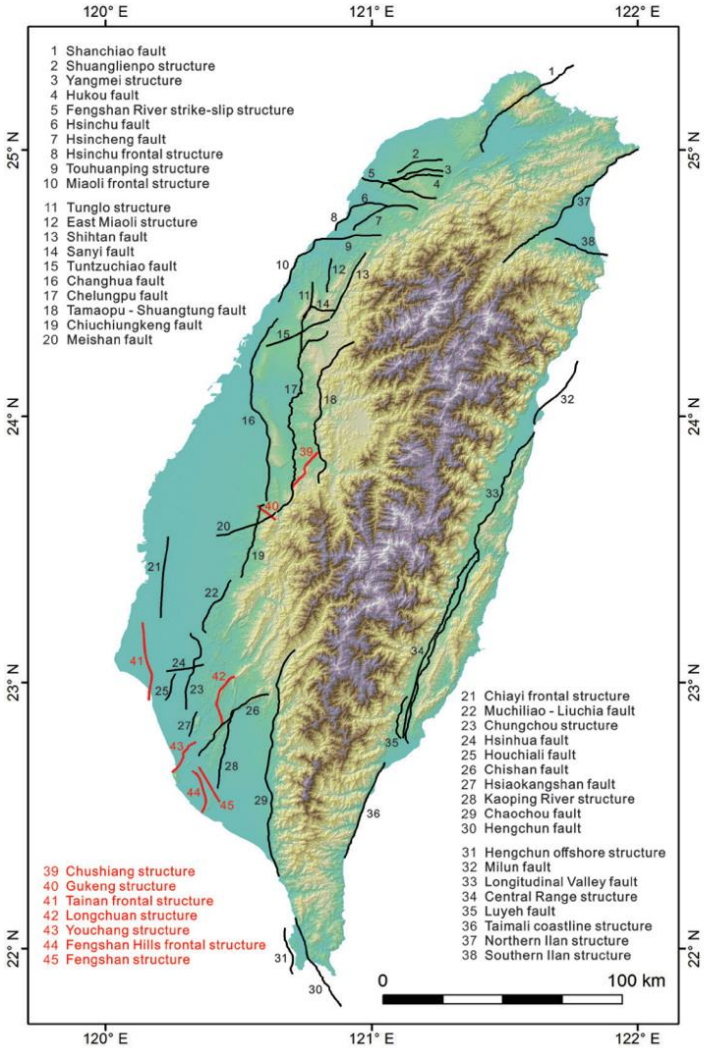

Fig. 2.3. Major on-land seismogenic structures of Taiwan. There are 45 structures in Taiwan. The black lines are the original structures (Shyu et al., 2016). The red lines show the new structures in Taiwan.

doi: 10.6342/NTU202400130

1. Hsinhua fault (HSH)

The Hsinhua fault extending from Naba to Beishi, Hsinhua Dist., Tainan with 6 km length. This fault is dominated by right-lateral motion with vertical motion with ENE trending (張麗旭等，1947). According to the borehole result, the Hsinhua fault has high dipping angle (陳文山等，2011). Huang et al. (2004) proposed that the Hsinhua fault is a back thrusting fault with 70∘dipping angle from the equilibrium profile result. The parallel-fault horizontal velocity is -9.7 mm/yr and the uplift rate is 2.8 mm/yr based on GPS observations (饒瑞鈞等，2005). It is a Holocene active fault.

2. Houchiali fault (HCL)

The length of this fault is about 12 km (林朝棨，1957; Sun, 1964) with a 45∘dip (Shyu et al., 2016). This fault is dominated by the reverse and right-lateral motion. By using the aerial photograph analysis, the Houchiali fault is identified at eastern wedge of the Tainan Tableland (Sun, 1964). This tectonic is assumed a blind fault with detachment (Fruneau et al., 2001). The long-term uplift rate of Tainan tableland upthrown side is about 4 mm/yr based on the regional Holocene relative sea-level curve (Chen and Liu, 2000). The short-term uplift rate, according to precise leveling data, is about 11~13 mm/yr on the Tainan Tableland (Huang et al., 2009). It is a Late Pleistocene active fault.

3. Fengshan fault (FS)

Sun (1964) inferred the scarp with NNW trending to Fengshan Hill northeast is the

doi: 10.6342/NTU202400130

evidence of Fengshan fault by aerial photograph analysis. The Fengshan fault is a left-lateral dominated with a minor reverse structure. Its length is 16.8 km and dip at 85∘in the East direction (Sun, 1964; Deffontaines et al., 1997; Shyu et al., 2020). The slip rate is about 10 mm/yr based on GPS data (Ching et al., 2007).

4. Hsiaokangshan fault (HKS)

Sun (1964) found the scarps along the west of Dagang Shan and Hsiaokangshan by aerial photograph analysis. The Hsiaokangshan fault is a blind fault that has a reverse motion with NNE trending (Hsu and Chang, 1979). The flexure scarp on the top of this fault is the evidence to prove that the Hsiaokangshan fault is a blind fault (Suppe, 1983; 陳文山等，2010). Its depth is 8 km (Sun, 1964) with east-dipping at 30∘ (Chen et al., 2008b; Shyu et al., 2016). The long-term slip rate is 5.7±1.4 mm/yr at the central part of the HKS fault based on borehole data (陳文山等，2010). It is a Late Pleistocene active fault.

5. Chekualin fault (CKL)

The Chekualin fault is a reverse fault with right-lateral motion. Its length is about 25 km and extends from Neimen Dist. to Ciaotou Dist., Kaohsiung. According to field survey data, the Chekualin fault locate at the foot-wall of the Chishan fault, the nearest distance between two faults is about 0.5~1 km (陳文山等，2012). The velocities related to the SR01 GPS station decrease from 50~60 mm/yr (near the Chishan fault) to 40 mm/yr (east

doi: 10.6342/NTU202400130

of the Hsiaokangshan fault), which shows that the Chishan fault and Chekualin fault are absorbing a shortening rate of approximately 10 to 20 mm/yr (饒瑞鈞，2006；胡植慶等，2012，2016). The average long-term uplift rate 3.4±1.6 mm/yr based on calibrated ^{14}C age (Ding et al., 2017). It is a Holocene active fault.

6. Chishan fault (CS)

The Chishan fault extends from Chishan Dist. to Renwu Dist., Kaohsiung. The fault is divided into two different faults called Neyin and Chishan because of different features (陳文山等，2005). Its length is 34.8 km (Lin et al., 2007). Its dip are 75◦ and 80◦ in the north and south parts, respectively (耿文溥，1967; Chen et al., 2012; Shyu et al., 2016). Based on geologic observations, the Chishan fault is a left-lateral strike-slip fault (Lacombe et al., 2001), and some branch faults show the strain on the slickenside (陳柏村，2005). Based on geodetic data, however, the Chishan fault is a reverse fault with minor right-lateral motion (Ching et al., 2007; Hu et al.,2007; Lacombe et al., 2001) and the main fault remains locked (陳柏村，2009). The slip rate of this fault is about 1.10±0.36 mm/yr (Shyu et al., 2016). It is a Holocene active fault.

7. Chaochou fault

The Chaochou fault is a reverse fault with left-lateral motion which is located at the boundary between the western foothill and southern central range. Its length is about 89 km (詹新甫，1964) and dip at 75° (Shyu et al., 2016) in the eastern side. There are small

doi: 10.6342/NTU202400130

bulges at northern bank of the Laonong River by field survey (楊貴三，1986). The GPS measurements show that the perpendicular velocity across fault decrease from 53.7 mm/yr to 49.8 mm/yr from east to west (饒瑞鈞等，2008). It is a Late Pleistocene active fault.

8. Chungchou fault (ChC)

The Chungchou fault is near the Hsinhua fault. Its length is 29.7 km with 30∘dip. It's an NNE-SSW striking structure. The uplift rate of the hanging wall is ranges from 5-8 mm/yr determined from borehole data (Chen and Liu, 2000; Chen, 2010), and slip rate at 12.20 ± 0.60 mm/yr (Shyu et al., 2016).

9. Youchang fault (YC)

The previous study found there are fault scarps with NE-SW striking between Youchang and Shoushan villages based on the photogeology method (Sun, 1964) so Cheng et al. (2007) inferred that there is a fault named Youchang fault. The Youchang fault is a reverse dominated fault with minor left-lateral motion and with NE-SW striking (Shyu et al., 2020). Its length is 4 km and dip at 75∘in the SW direction (Sun, 1964; Ching et al., 2007; Shyu et al., 2020). The slip rate is at 0.92~5.46 mm/yr (Shyu et al., 2020).

doi: 10.6342/NTU202400130

2.2 Region surface deformation in SW Taiwan

Ching et al. (2007) used 103 continuous GNSS stations data in SW Taiwan with respect to a stable continental margin station S01R, which is located at Penghu Island, to estimate the vertical velocities in SW Taiwan. They found that the uplift rate of 10 to 20 mm/yr is distributed in the Western Foothills and the Central Range. The subsidence rate of 5 to 20 mm/yr is concentrated in the coastal area north of Kaohsiung City, especially in the southernmost area of the Pingtung Plain. In Ching et al. (2011), there are 1843 leveling and 199 continuous GNSS measurements from 2000 to 2008 used to measure vertical deformation rates. At the southern part of the Western Foothills, the rate of ~18.5 mm/yr was measured. In addition, the short-term and long-term rates are consistent.

Ching et al. (2016) found the sharp velocities gradients in the region of Hsiaokangshan fault (HKSF) and Chishan fault (CHNF) by campaign-mode GNSS observations and CGS precise leveling measurements between 2002 and 2010 to understand the crustal deformation in SW Taiwan (Fig. 2.4). They found the velocities on the west side of the HKSF are subsidence. The velocity eastward is up to ~ 18 mm/yr between the HKSF and the CHNF. The velocities on the east side of CHNF are then subsidence again.

Currently, with satellite provide high-resolution images, Huang et al. (2016) used ERS and Envisat images to estimate the surface deformation in SW Taiwan (Fig. 2.5). East of

doi: 10.6342/NTU202400130

the Chiayi land subsidence area, there is 5–15 mm/yr surface uplift between the Meishan fault and the Tsochen fault detected by InSAR and CGNSS, and the area of uplift roughly outlines the shallow seismicity zone in the Western Foothills. According to foresaid, there are significantly deformation near active faults and coast area in SW Taiwan. We can focus on place that with high uplift rate, and discuss the mechanisms of surface deformation. Lu et al. (2023) found the postseismic deformation rates are 1.5 and 2 times higher than the interseismic period in E-W and vertical directions, respectively. The significant linear deformation in the E-W direction located at the southern part of SW Taiwan, such as HKS, CS, and YC faults; while HCL, HSH, and HKS faults have linear deformation in the vertical direction by using advanced multi-temporal InSAR which constrained by continuous GNSS data during 2016 to 2018.

Tsukahara and Takada (2018) further use L-band SAR images to process PSInSAR, which is corrected by GNSS data to remove ionospheric error, and leveling data to detect aseismic growth of Tainan tableland in SW Taiwan (Fig. 2.6). They found the very rapid uplift velocity at the eastern flank of the Tainan tableland. The maximum velocity reaches 37 mm/yr in the northern part. They interpret that the main cause of this uplift rate contributed by mud diapirs and also have a shallow fault motion which adds a short-wavelength perturbation before and during the Meinong earthquake.

doi: 10.6342/NTU202400130

2.3 Critical infrastructure monitoring in Taiwan

In Taiwan, there are some studies about Critical infrastructures. 張中白等 (2004) and Wang et al. (2011) used leveling, GPS, and DInSAR observations to monitor the subsidence at Zhongli Industrial Park, Taoyuan, which has 4 cm in cumulative subsidence and 4 mm/yr subsidence rate (Fig. 2.9); Hwang et al. (2008) used GPS and leveling data to monitor the section of THSR that pass through an area of Yunlin County (Fig. 2.10). They found the largest cumulative subsidence is about 22 cm from 210K to 240K of THSR. Recently, Lu et al. (2023) found 7 active faults around their study area with different deformation rate. The critical infrastructure in his study area, 45% of total lengths of Freeway were faced with higher than 10mm/yr in the E-W component and 50% of total lengths of Railway were in the face of higher 10mm/yr in the vertical component. According to these studies, we can know that there is the surface deformation near these critical infrastructures. In SW Taiwan, most studies only focus on individual critical infrastructure, lacking of deformation for a wide range of critical infrastructure by InSAR.

doi: 10.6342/NTU202400130

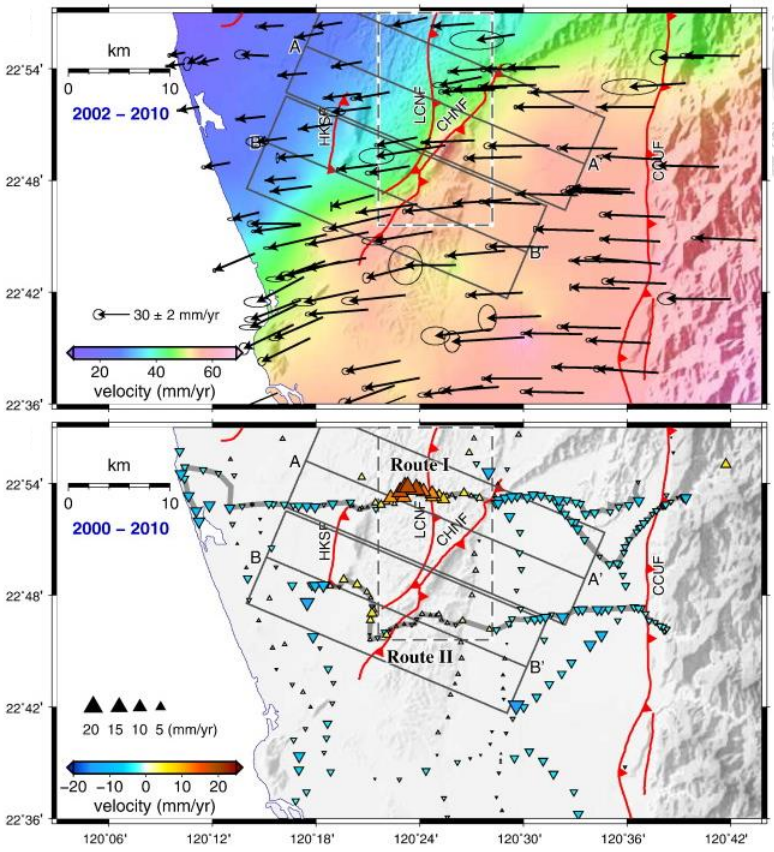

Fig. 2.4. GNSS and leveling observations. Top is horizontal velocities relative to S01R from 2002 to 2010. Bottom is vertical velocity field during the period from 2000 to 2010 (Ching et al., 2016).

doi: 10.6342/NTU202400130

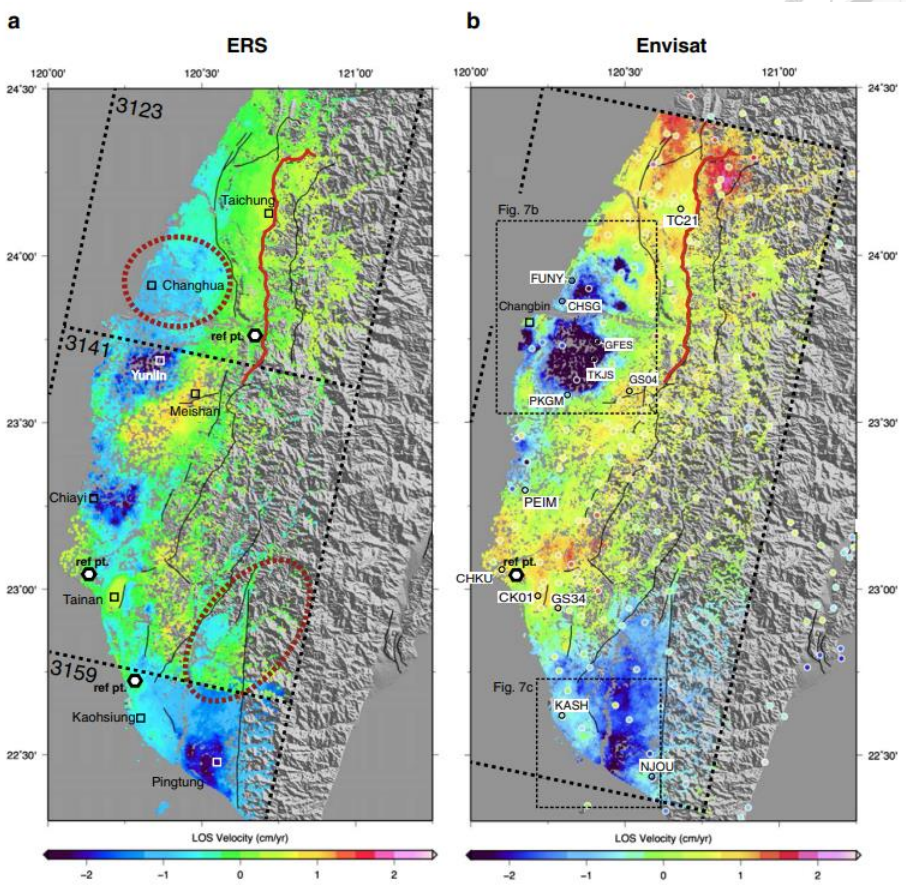

Fig. 2.5. InSAR results from Huang et al. (2016) (a) Mean annual line of sight (LOS) velocity during 1995–1999 (frame 3123) or 1995–2001 (frames 3141 and 3159). (b) Mean annual LOS velocity during 2005–2008. The circles are continuous GNSS (CGNSS) stations and the color in the circles indicates the CGNSS derived LOS velocity in the same time period as InSAR.

doi: 10.6342/NTU202400130

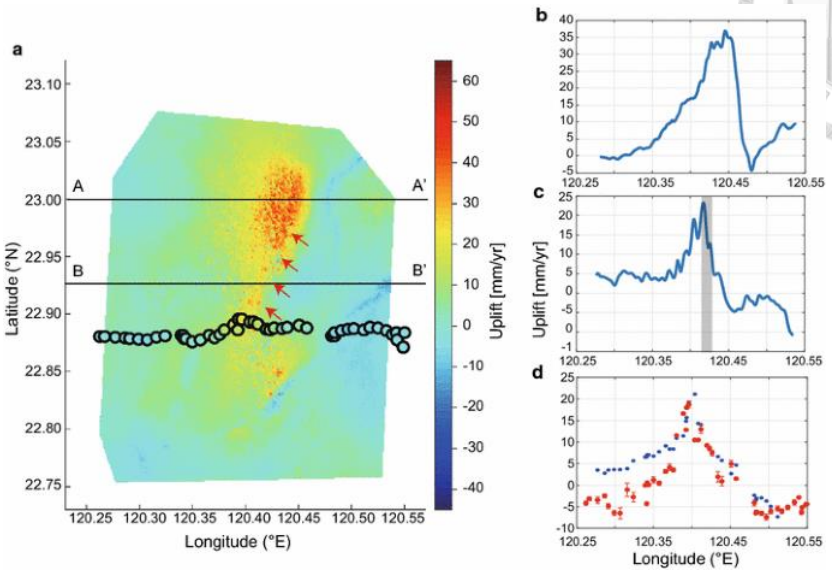

Fig. 2.6. Uplift rate calculated by using ALOS data. Colored circle is uplift rate obtained from leveling survey (Ching et al., 2016; Tsukahara and Takada, 2018).

doi: 10.6342/NTU202400130

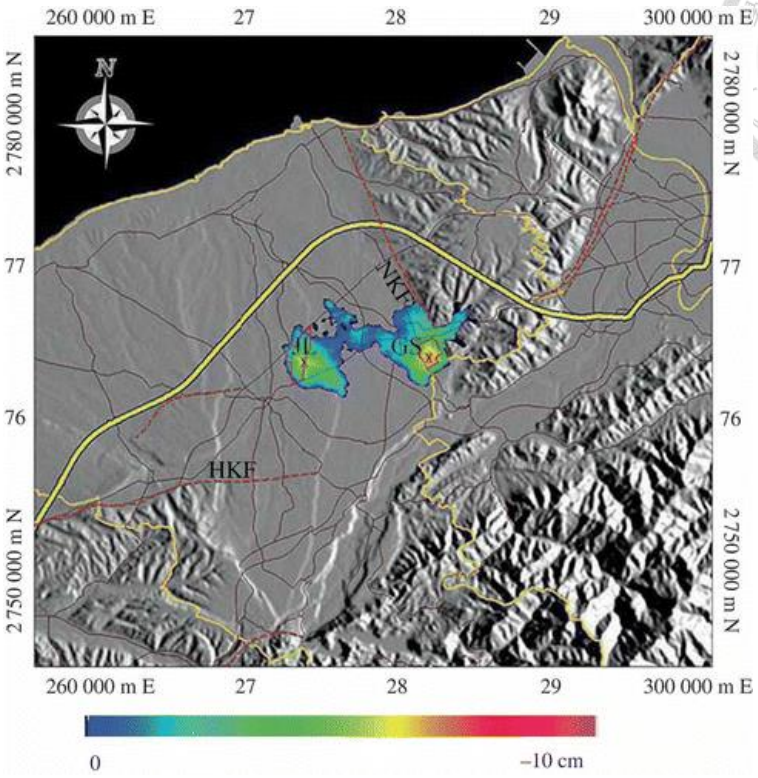

Fig. 2.7. The subsidence along LOS, showing a duplet deformation pattern at Jhon-Li (JL) and Guei-Shan (GS) Industrial Parks (Wang et al., 2011).

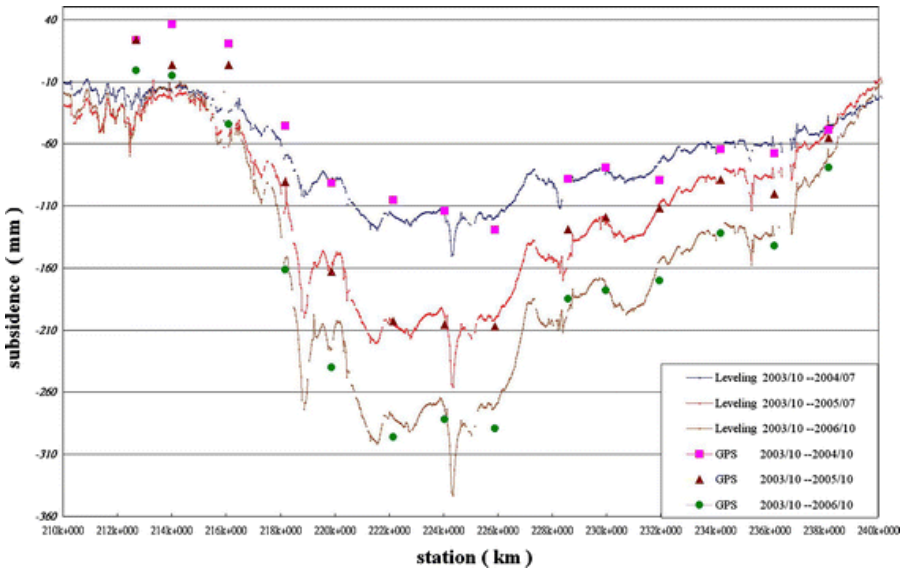

Fig. 2.8. Subsidence from GPS and leveling with respect to THSR stations (Hwang et al., 2008).

doi: 10.6342/NTU202400130

Chapter 3 Method

In recent years, primary detecting methods such as GNSS, leveling, and InSAR have been used in surface deformation. To get a wide range of time-series displacements and the velocity field near critical infrastructure across active faults in SW Taiwan, I acquired Sentinel-1 SAR images processed by the PSInSAR algorithm and verified the PS observations by using GNSS stations data.

3.1 Radar (RAdio Detection And Ranging)

Radar (Radio Detection and Ranging) is an active system that emits microwaves to detect a target on the surface. When measuring the bounce back energy, the radar sensor can be separated into two systems. One is a non-imaging system and the other is an imaging system. The former system can only range the distance between a target and the satellite, and the latter not only can range distance but can be processed in a 2D image. This study uses Synthetic Aperture Radar (SAR), which is one of the imaging systems.

With different purposes, there are different wavelengths and frequencies on SAR satellites (Table 3.1). These microwaves with a longer wavelength, which can penetrate through clouds and vegetation. The C-band Sentinel-1 satellite with 5.6 cm is used in this study.

doi: 10.6342/NTU202400130

Table 3.1: Microwave frequency and wavelength used on satellite (data from ESA).

Band	Frequency (GHz)	Wavelength (mm)	Satellites
Ka-band	26-40	5-11.3	
Ku-band	12-18	16.7-25	
X-band	8-12	25-37.5	TerraSAR-X
C-band	4-8	37.5-75	Sentinel-1
S-band	2-4	75-150	
L-band	1-2	150-300	ALOS-1, ALOS-2

3.2 Side-Looking Airborne Radar (SLAR) and Synthetic Aperture Radar (SAR)

3.2.1 SLAR

The traditional type of sensing geometry is nadir-looking radar, which can only distinguish targets from arrival time (echolocation) so that this sensing geometry cannot distinguish between two objects that are equal distances from the sensor. To avoid echolocation that is produced from nadir-looking radar, a radar had been installed airborne to monitor targets, and this type was called Side-Looking Aperture Radar (SLAR). In the geometry of SLAR, satellite get the echoes from different objects at different times so that we can identify them clearly (Fig. 3.1). To get a large scope of surface, radars have been installed on satellites; however, resolution decreases accordingly.

The slant-range resolution (R_{range}) means the minimum unit that can distinguish the

doi: 10.6342/NTU202400130

distance between two points in the ranging direction. In the theoretical value, the resolution is half of pulse length (PL) (Fig. 3.1) which is equal to half of $c * \tau$;

$$R_{range} = \frac{PL}{2} = \frac{c\tau}{2}$$

where R_{range} is slant-range resolution, c is the speed of light, and τ is pulse duration; however, the slant-range resolution is determined by the incidence angle in a real situation (Fig. 3.2).

$$R_{range} = \frac{c\tau}{2sin\theta}$$

where θ is incidence angle.

The azimuth resolution (R_{azi}) is the width of swath in the flight direction which is determined by the beam width of the antenna and slant range distance (Fig. 3.3). The equation is following:

$$R_{azi} = SR \times \beta \quad \beta = \frac{\lambda}{AL}$$

where SR is slant-range distance, β is beam width, λ is wavelength, and AL is the length of antenna. According to the equation, the longer the antenna, the better the azimuth resolution.

3.2.2 SAR

With the demand for high-resolution radar images, the concept of SAR has been established. Each pixel in the SAR image has the phase and amplitude information, which is the mean of whole backscatters in the LOS direction. The receiving antenna on the

doi: 10.6342/NTU202400130

satellite receives echo in a different position due to platform motion (Fig. 3.4) (Moreira et al., 2013). This concept is to increase a virtual aperture antenna longer than the physical antenna length. SAR uses side-looking to decrease Doppler frequency shifts from platform motion. By overlapping these signals, it can increase the Signal-to-Noise Ratio (SNR) to provide better resolution than traditional radar image. It offers high-resolution and weather-independent images day and night to monitor surface targets. The radar image with SAR processing has better resolution and can be used to separate surface objects more clearly (Fig.3.5).

3.3 InSAR and DInSAR

Interferometry SAR (InSAR) uses two SAR images, which are acquired on different dates, to process phase interferometry and to produce Digital Elevation Model (DEM) (Fig. 3.6). After the success of differential interferometry technique to process the Landers earthquake to obtain displacements (Massonnet et al., 1993), the Differential interferometry SAR (DInSAR) technique have been widely used in estimate surface deformation (Prati et al., 2010; Stramondo et al., 2016; Pepe and Calò, 2017). The DInSAR technique is to calculate the phase difference in two images of the same area that were collected at different periods to get an interferogram. The phase difference will be displayed in a fringe pattern, and we can get displacement by unwrapping (Fig. 3.7).

doi: 10.6342/NTU202400130

The phase of deformation can be monitored by removing the phase contributed by terrain, orbit, and atmospheric effects. The interferometric phase can be formulated as:

$$\emptyset^{total} = \emptyset^{topography} + \emptyset^{def} + \emptyset^{orbit} + \emptyset^{aps} + \emptyset^{noise}$$

where $\emptyset^{total}$ is the total phase change of two SAR images, $\emptyset^{def}$ is the phase due to surface deformation in the line-of-sight (LOS) direction, $\emptyset^{orbit}$ is the phase of orbit inaccuracies, $\emptyset^{aps}$ is the phase due to tropospheric delay, and $\emptyset^{noise}$ is the phase error.

The traditional DInSAR method has some limits such as the decorrelation caused by temporal error and low SNR due to noise in the vegetation area, which would lead to low coherence to produce an interferogram. To solve these problems aforesaid, Persistent Scatterers InSAR (PSInSAR) has been proposed.

3.4 Persistent Scatterers Interferometry (PSInSAR)

PSInSAR is one of the most famous techniques in the InSAR method. This method can get stable ground objects to improve the low SNR situation. The Persistent Scatterers (PSs) concept in SAR had been proposed by Ferretti et al. (2000) called Permanent Scatterer™ or Persistent Scatterer Interferometry (PSI). The PSI uses amplitude to choose objects, which have stable signals as PSs. This parameter is called the Amplitude Dispersion Index (ADI). Scatterers with an ADI lower than 0.25 can be chosen as PSs for obtaining surface displacement.

doi: 10.6342/NTU202400130

3.4.1 Produce interferogram

In this study, we use the StaMPS/MTI (Stanford Method for Persistent Scatterers/ Multi-Temporal InSAR) algorithm which is based on PSI concept proposed by Hooper et al. (2003, 2007a, 2007b, 2008). This algorithm uses single look complex (SLC) which are image in the same image plane of satellite data acquisition. Then, we use Interferometric synthetic aperture radar Scientific Computing Environment (ISCE) software. The initial development of this project received funding from NASA's Earth Science Technology Office (ESTO) through the Advanced Information Systems Technology (AIST) 2008. Currently, funding is provided through the NASA-ISRO SAR (NISAR) project. In this step, all of SAR images are paired with the reference image to create interferograms and remove the contribution of terrain. Finally, we use orbital data and DEM to geocode interferograms.

3.4.2 Phase stability analysis

The StaMPS method uses a higher ADI threshold (lower than 0.4) and phase analysis, which is based on the spatial correlation between displacements and other errors, to select PS (Fig. 3.8). The concept of PS is to choose the surface objects, which have a more stable signal such as building, road, or other anthropogenic structures. In Fig. 3.9, Hooper simulates 100 measurements in different situations, the pixel has a strong reflection object

doi: 10.6342/NTU202400130

which can provide a more stable signal (right) than a non-PS pixel (left). Using these stable objects, we can filter noise and get a more reliable time series result.

$$D_A = \frac{\sigma_A}{\mu_A}$$

where D_A is the amplitude parameter of a pixel; μ_A is the average amplitude of each pair; σ_A is the standard deviation of amplitude of each pair. In StaMPS, Hooper suggests default D_A value is 0.4. We use the default value to select PSs. The ADI (D_A) of pixel is higher than 0.4 means the signal is unstable and will be abandoned; conversely, it will be retained as PSC (Persistent Scatterers Candidate) for further analysis.

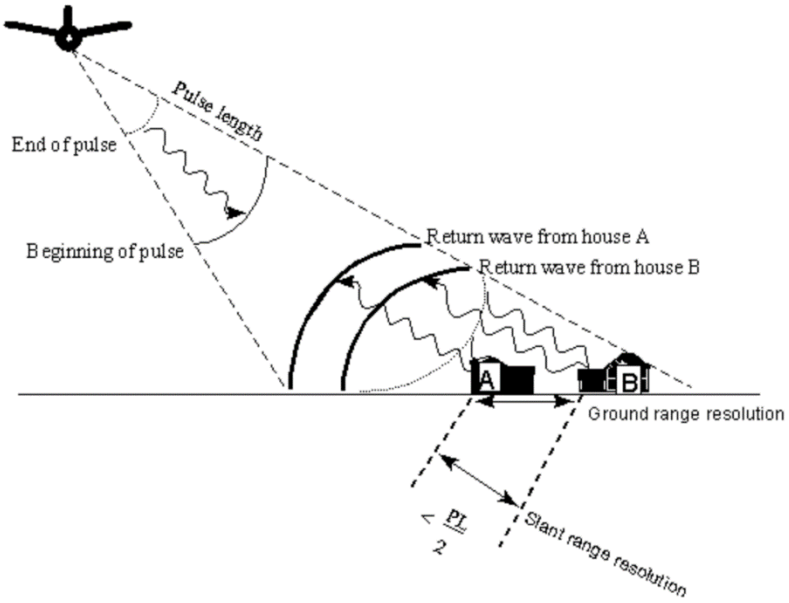

Fig. 3.1. The geometry of SLAR LOS direction (Lillesand and Kiefer., 1994). The echoes of house A and house B return to antenna at different time.

doi: 10.6342/NTU202400130

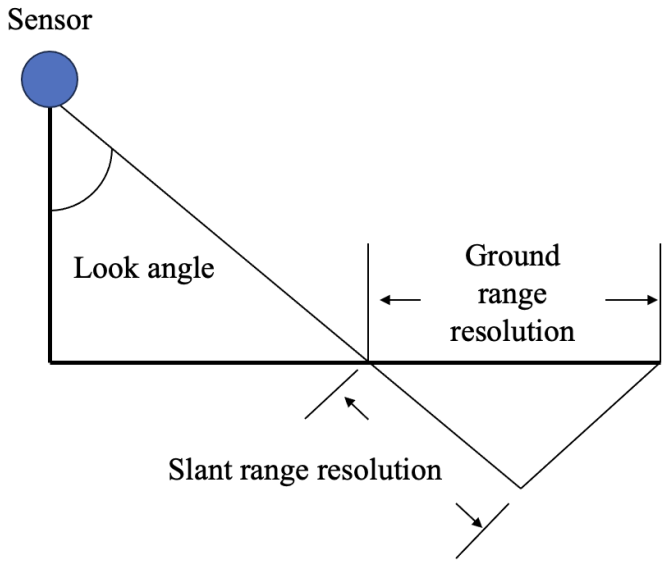

Fig. 3.2. The geometry of slant-range and ground range. (Modified from Ezeoke et al., 2014).

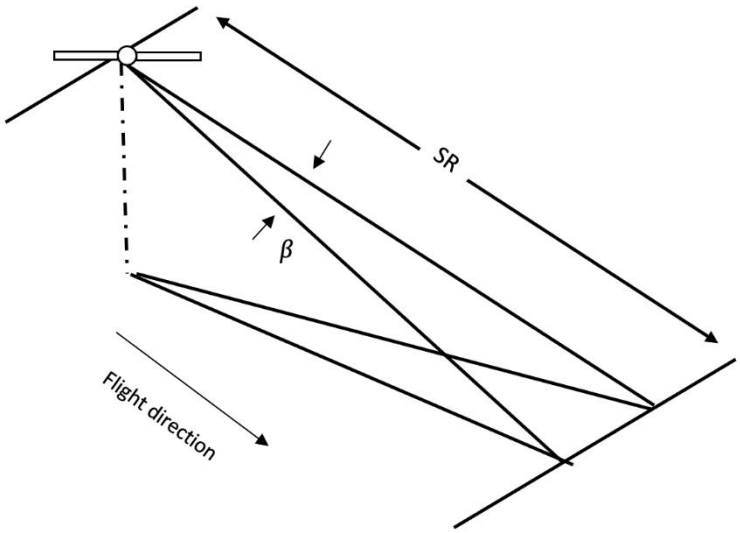

Fig. 3.3. The schematic figure of azimuth resolution. β is beam width. SR is slant-range.

doi: 10.6342/NTU202400130

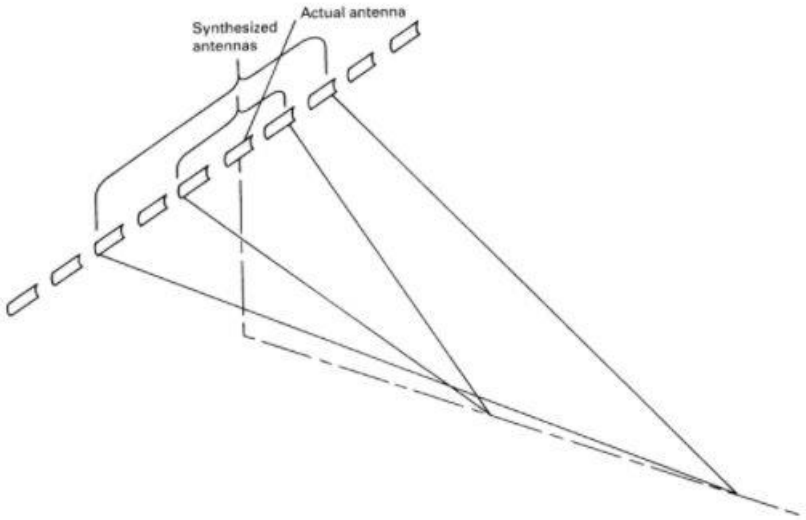

Fig. 3.4. Concept of an array of real antenna position forming a synthetic aperture (Lillesand et al., 2015)

Fig. 3.5. The comparation between amplitude images. Left is the signal from one receiving. Right is improved by SAR technique (derived by Massonnet and Feigl, 1998).

doi: 10.6342/NTU202400130

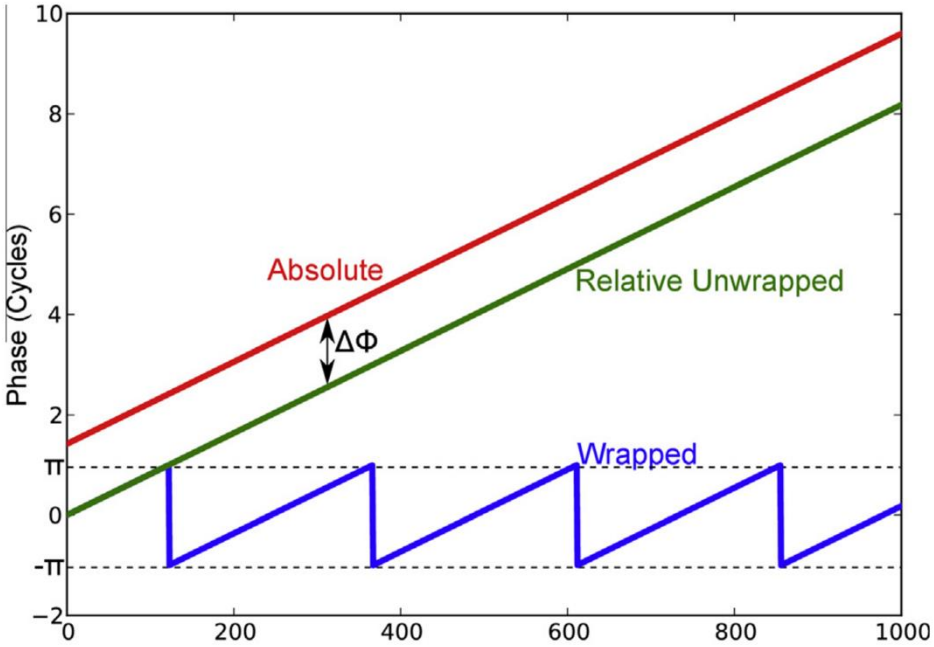

Fig. 3.6. The concept of phase unwrapping (Osmanoğlu et al., 2016).

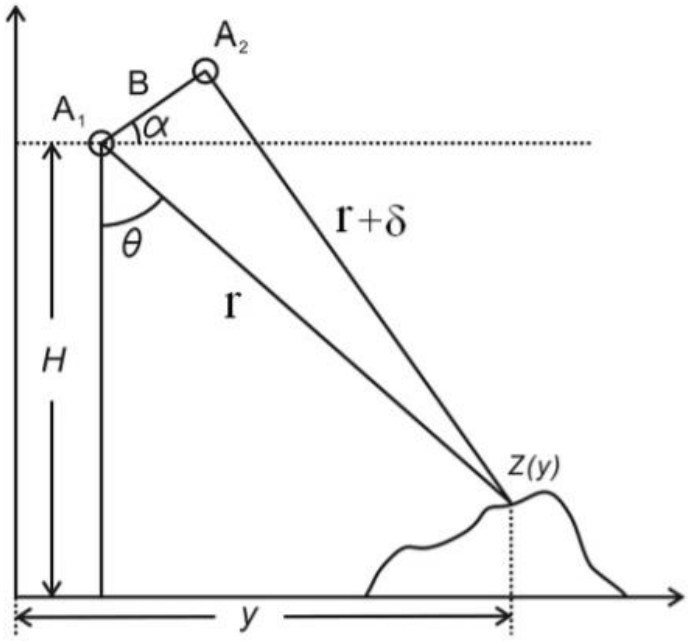

Fig. 3.7. Radar interfering schematic diagram (謝嘉聲，2006). A1 and A2 is location of antenna at different time. B is distance between two antennas. H is flying height. “r” is distance at first antenna and ground. r + δ is distance between second antenna and ground. α is angle between B and horizontal line. θ is look angle.

doi: 10.6342/NTU202400130

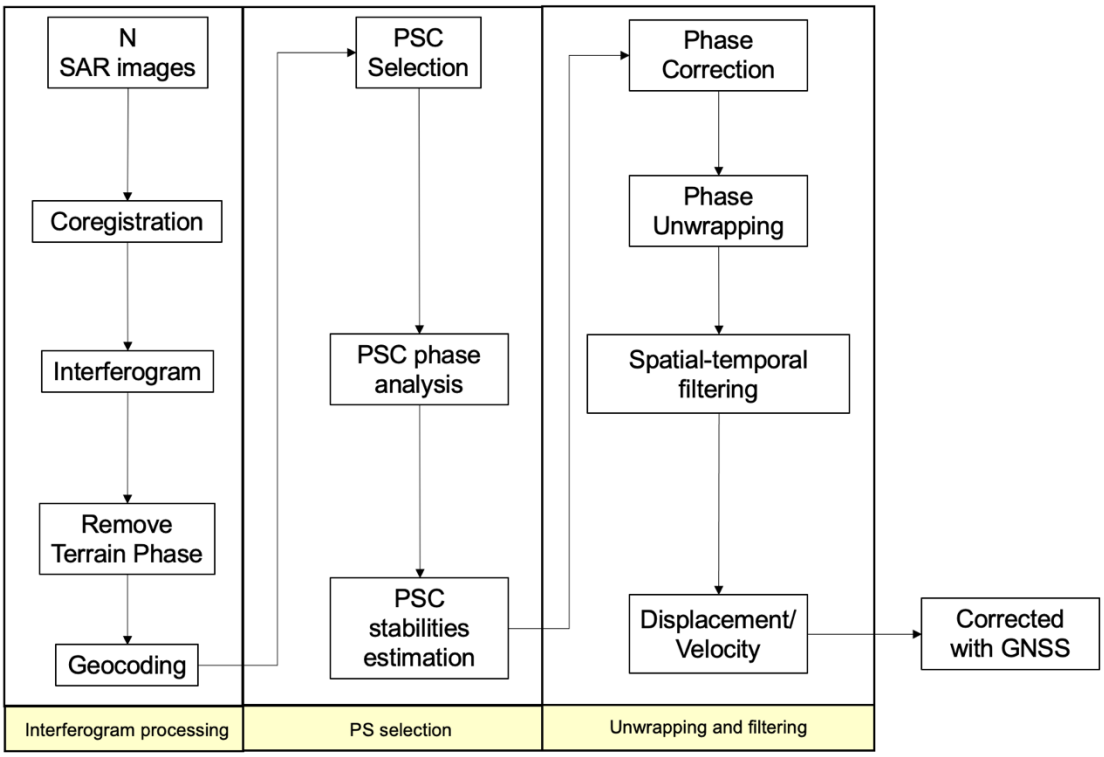

Fig. 3.8. PSInSAR workflow

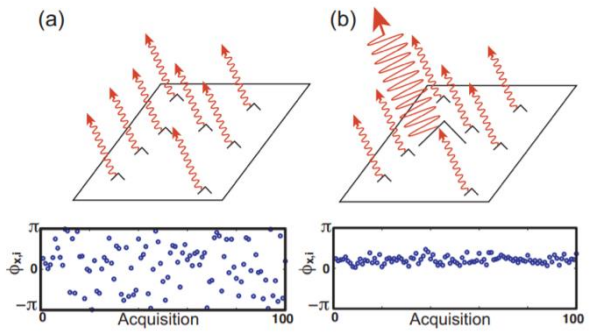

Fig. 3.9. Persistent Scatterer feature (Hooper, 2007). (a) The stability of surface object signal when there are no PS in pixel. (b) The stability of surface object signal when there are PS in pixel.

doi: 10.6342/NTU202400130

3.5 Data collection

A set of data provided by the C-band Sentinel-1 satellite from the ESA acquired during the period from March 9, 2016 to November 14, 2021, are used in this study. To detect this area, Sentinel-1 data used in this study are from ASC (path 69) and DES (path 105) which cover the SW Taiwan from Tainan to Pingtung (Table 3.2). To process PSInSAR, we need to choose one reference image. In the ASC and DES tracks, we choose the reference image acquired on January 17, 2019 (Figure 3.10) and January 7, 2019 (Figure 3.11), respectively.

Table 3.2: Sentinel-1 satellite information

Satellite	Sentinel-1	
Direction	Ascending	Descending
Heading angle	-10.59∘	-169.49∘
Incidence angle	29.1° - 46.0°	
Path no.	69	105
Reference image	2019/01/17	2019/01/07
Band	C-band (5.6 cm)	

doi: 10.6342/NTU202400130

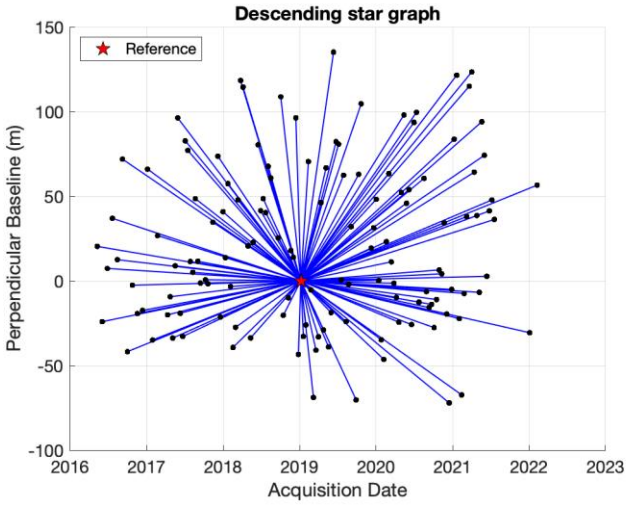

Fig. 3.10. The PSInSAR baseline graph shows the temporal/ perpendicular baseline distribution of data of the orbit path 105. Blue lines represent the interferogram of two SAR acquisitions in black dots.

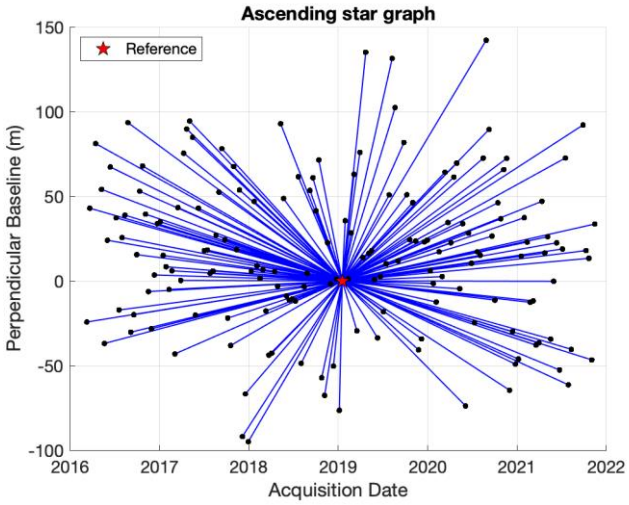

Fig. 3.11. The PSInSAR baseline graph shows the temporal/ perpendicular baseline distribution of data of the orbit path 69. Blue lines represent the interferogram of two SAR acquisitions in black dots.

doi: 10.6342/NTU202400130

The Global Navigation Satellite System (GNSS) consists of the United States' GPS (Global Positioning System), Russia's GLONASS (Global Navigation System), China's BeiDou Navigation Satellite System, and the European Union's Galileo system. GNSS is based on some real-time positioning, navigation, and time calibration. The global geocentric coordinate system is adopted and the origin of the coordinates is the center of the Earth, and the distance between the surface observation point and the technical satellite is obtained by measurement, and the coordinates of the surface position are obtained. GNSS can provide the three-dimensional coordinate location (longitude, latitude, and elevation) so that GNSS can be used to detect surface deformation (Segall and Davis, 1997).

The continuous GNSS data from 2016 to 2021 used in this study were processed by the GPS lab at the Institute of Earth Sciences, Academia Sinica. And GPS lab uses GIPSY to calculate the resolution of GNSS data. To calculate the surface deformation, this study used GNSS time-series data to compare the InSAR result. GNSS time-series is the resolution of everyday location. For long-term observations, the GNSS time-series includes many signals from different sources. This study used Matlab to calculate the best fit of E-W direction, N-S direction, and Vertical direction of GNSS. There are 70 GNSS stations in our study area (Fig. 3.12). The workflow for producing GNSS data is below. In the first step, I checked the statistical dispersion of raw data and then we get rid of the

doi: 10.6342/NTU202400130

data out of 3 standard deviations in each direction. In the second step, I used the result produced in the first step to calculate the best-fit velocity. Then, I removed the values caused by antenna change, coseismic displacement, and secular (season) variation we can decrease error and get more precise GPS velocity data to correct PSInSAR data.

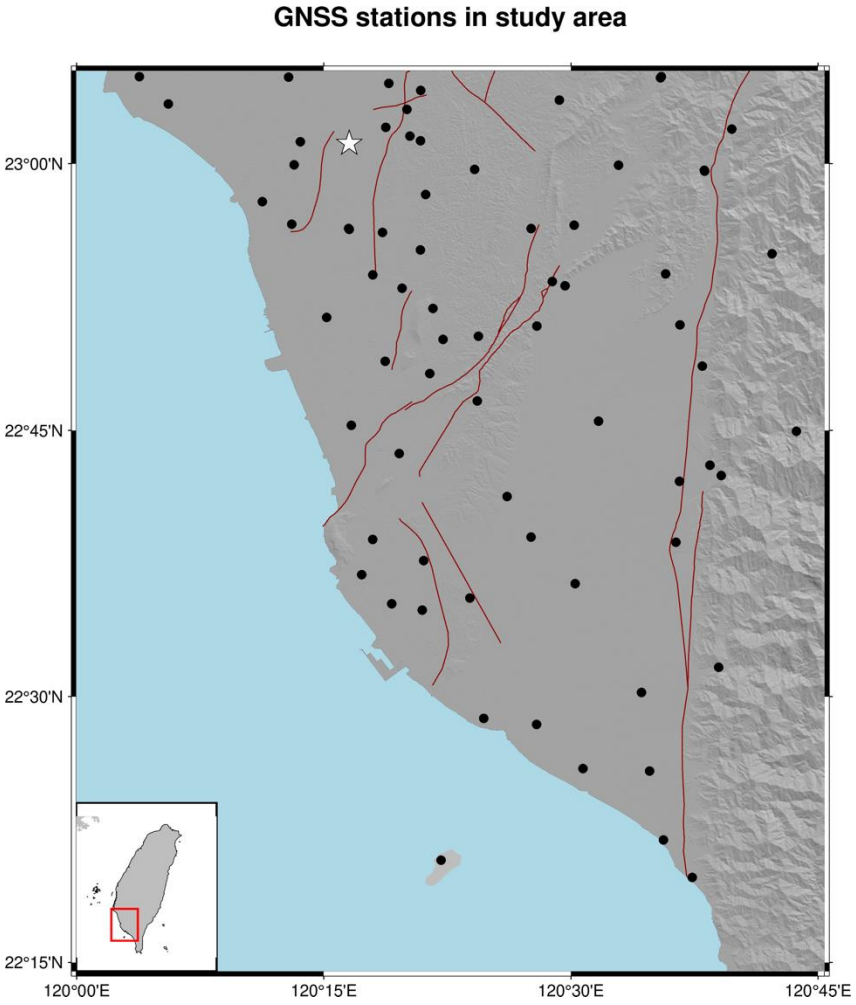

Fig. 3.12. GNSS stations in our study area. Black dots represent GNSS stations. Dark red lines represent active structures.

doi: 10.6342/NTU202400130

Chapter 4 Result

4.1 PS velocity fields in LOS direction

In this section, we would show the PSInSAR result in LOS direction with GNSS reference, and inversion to vertical direction result. I carefully checked all the interferograms and removed weird ones to reduce errors (see supplementary 1). The result of this study shows the sharp velocity across primary active faults in SW Taiwan.

The first result is PSInSAR velocity in the ASC track and the reference image is 2019/01/07. The velocity on the south side of the CKL fault is about 10 mm/yr and about 5 mm/yr on the north side of the CKL fault, the velocity on the west side on the south section of the HCL fault is about 4 mm/yr and about 2 mm/yr at the east side of the HCL fault, and the velocity on the south side of the YC fault is about 8 mm/yr and about 5 mm/yr on north side of the YC fault (Fig 4.1). The standard deviation (STD) of PS LOS velocities at the ASC track. We can see that the value of man-made buildings, such as railways, roads, and bridges is lower than 2 mm/yr (Fig. 4.2).

The second result is PSInSAR velocity in the DES track, and the reference image is 2019/01/17. The velocity at the west side on the south section of the HCL fault is about 5 mm/yr and about 3 mm/yr at the east side of the HCL fault; the velocity on the west side of the FS fault is about -2 mm/yr and about 5 mm/yr on the north side of the FS fault (Fig 4.3). Fig. 4.4 shows the STD of the LOS velocities at the DES track. We can also see that

doi: 10.6342/NTU202400130

the value of man-made buildings, such as railways, roads, and bridges is lower than 2 mm/yr.

doi: 10.6342/NTU202400130

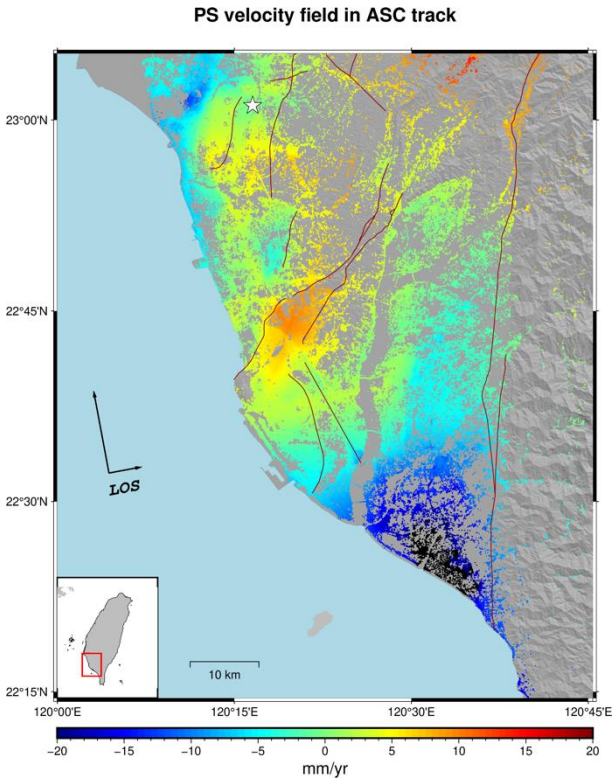

Fig. 4.2. PSInSAR result in LOS direction at ASC track. Dark red lines represent active structures.

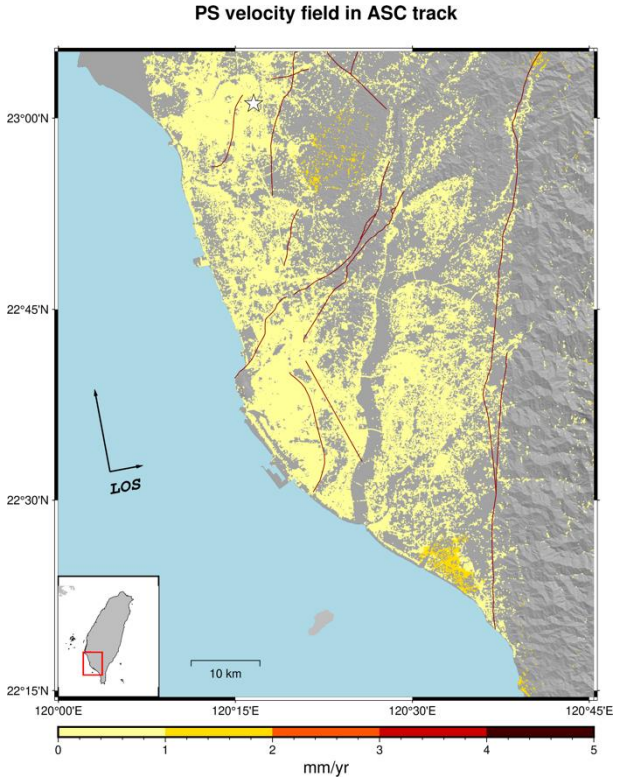

Fig. 4.1. The standard deviation in ASC track. Dark red lines represent active structures.

doi: 10.6342/NTU202400130

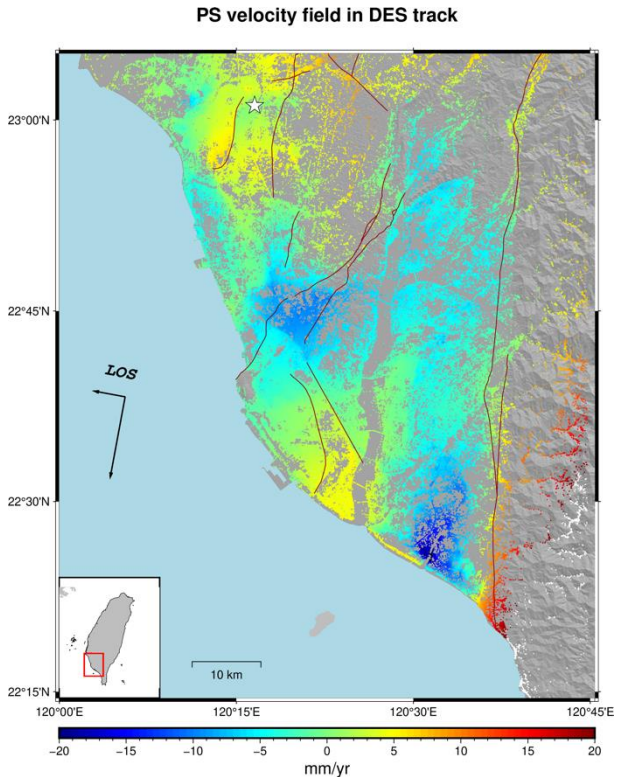

Fig. 4.3. PSInSAR result in LOS direction at DES track. Dark red lines represent active structures.

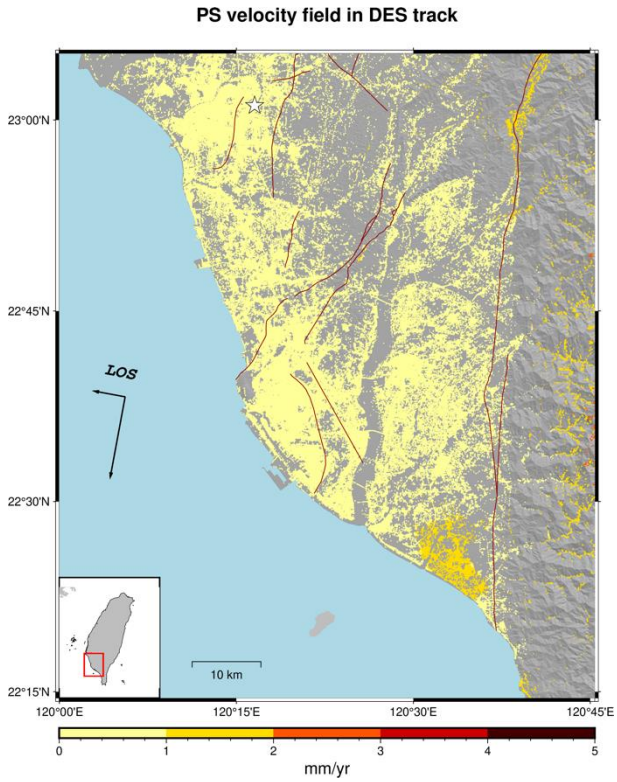

Fig. 4.4. The standard deviation in DES track. Dark red lines represent active structures.

doi: 10.6342/NTU202400130

4.2 Correct PSInSAR by GNSS velocity

To assess PSInSAR results, we use GNSS stations data to correct. The PSInSAR shows displacements in LOS directions; however, GNSS measurements show displacements in E, N, and U directions. Therefore, to compare these two data, we projected GNSS data to LOS direction. The projection equation is following (Miller, 2015):

$$\mathrm{GNSS_{LOS}} = [\,-\sin\theta * \sin(\alpha - 270) - \sin\theta * \cos(\alpha - 270)\ \cos\theta] * \begin{bmatrix} VE \\ VN \\ VU \end{bmatrix}$$

where $\mathrm{GNSS_{LOS}}$ is projected GNSS velocity in LOS direction, θ is incline angle, VE is GNSS velocity in East-West direction, VN is GNSS velocity in North-South direction, VU is GNSS velocity in uplift direction, and α is heading angle of azimuth direction (angle values see Table 4.1). The selected reference point is GS31, which has relatively stable time-series velocity in three directions (Fig. 4.5). The period here is from 2016 after Meinong to 2020. Presumably, the stable area is considered as a spatial reference (low variation displacement value near GNSS station GS31), and PSInSAR results were compared to GNSS observations.

doi: 10.6342/NTU202400130

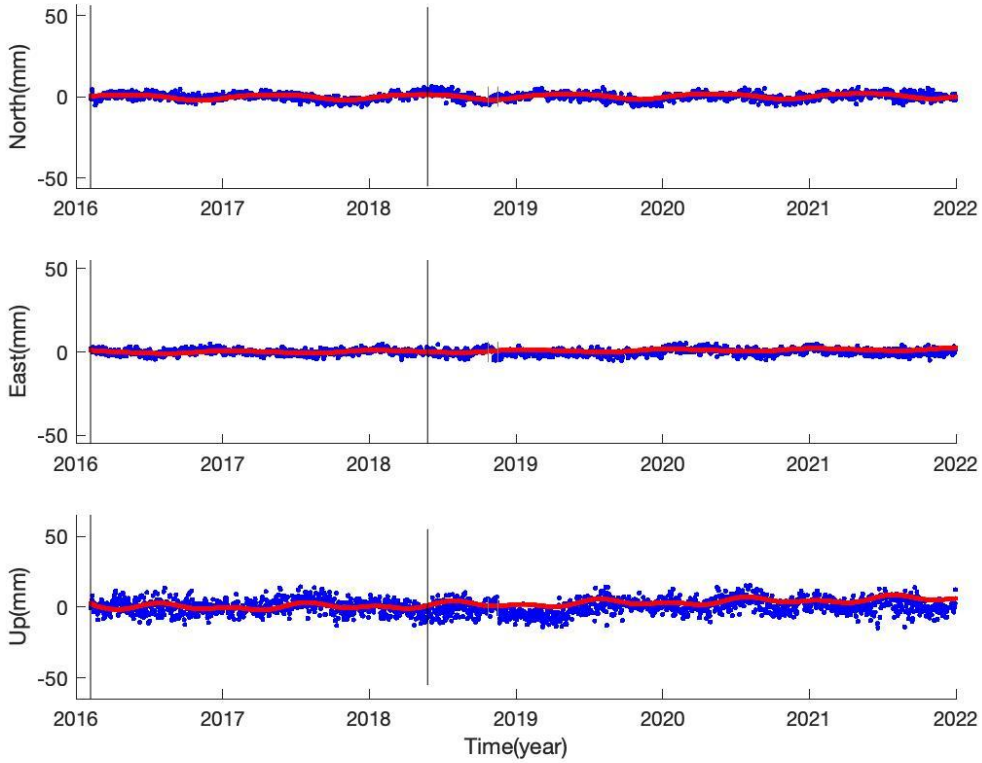

Fig. 4.5. GNSS station GS31 time-series and best-fit velocities in E, N, and U directions. Blue dots represent time-series velocities. Red line is the best-fit velocity. Black vertical lines represent the 2016 Meinong earthquake and the antenna change.

The following result is the velocity of PS and GNSS observations in the LOS direction, and the reference point is GNSS station GS31. In the ASC track, we can see the pattern of two observations has the same trending at GS31 station and near active faults (Fig 4.6). In the DES track, there is also have good comparison of PS and GNSS observations (Fig 4.7).

doi: 10.6342/NTU202400130

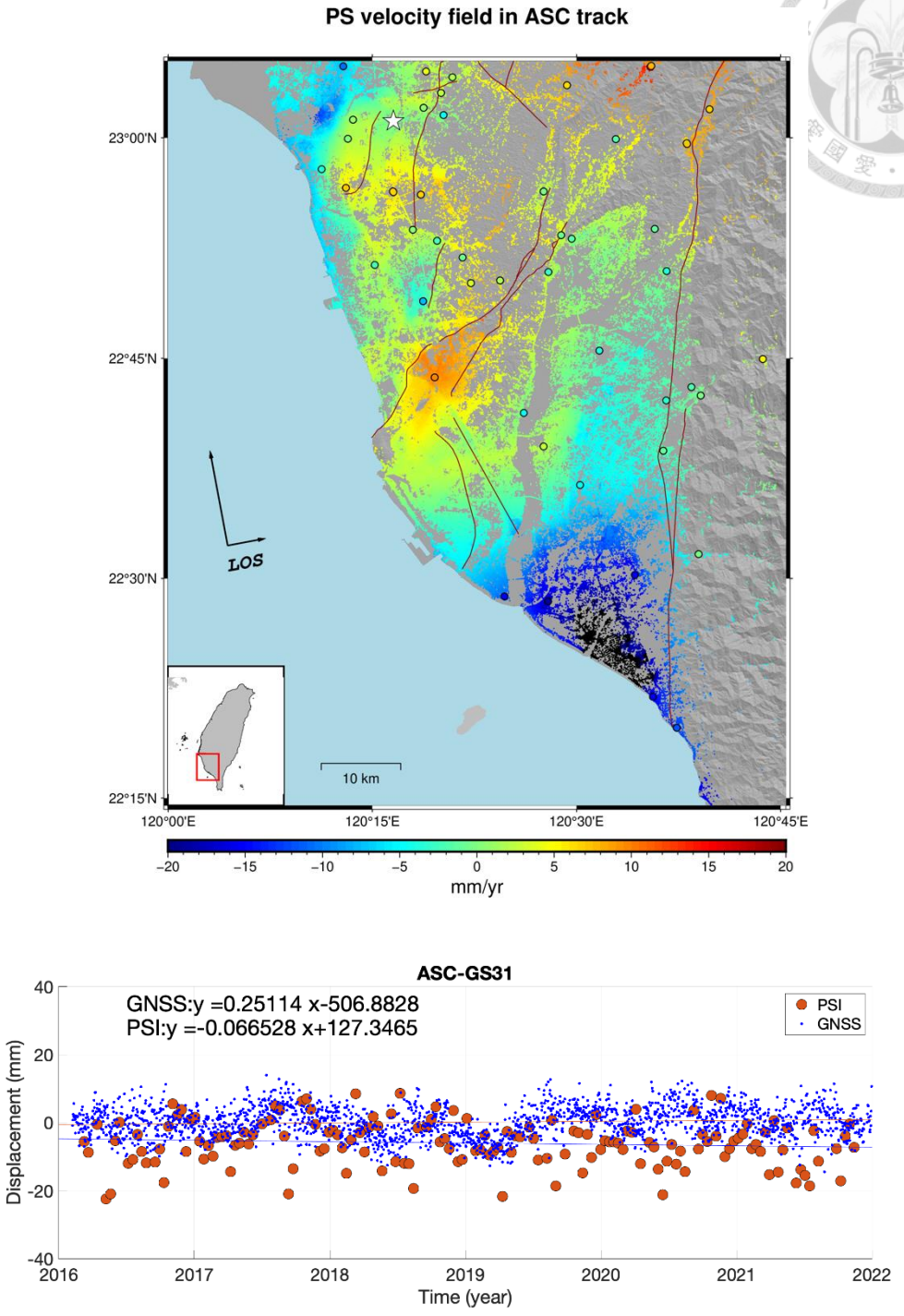

Fig. 4.6. PSInSAR result reference to GNSS observations and the comparison of both data at GS31 station in ASC track. The white star is the reference point (GS31 station). The dots are GNSS stations in the study area.

doi: 10.6342/NTU202400130

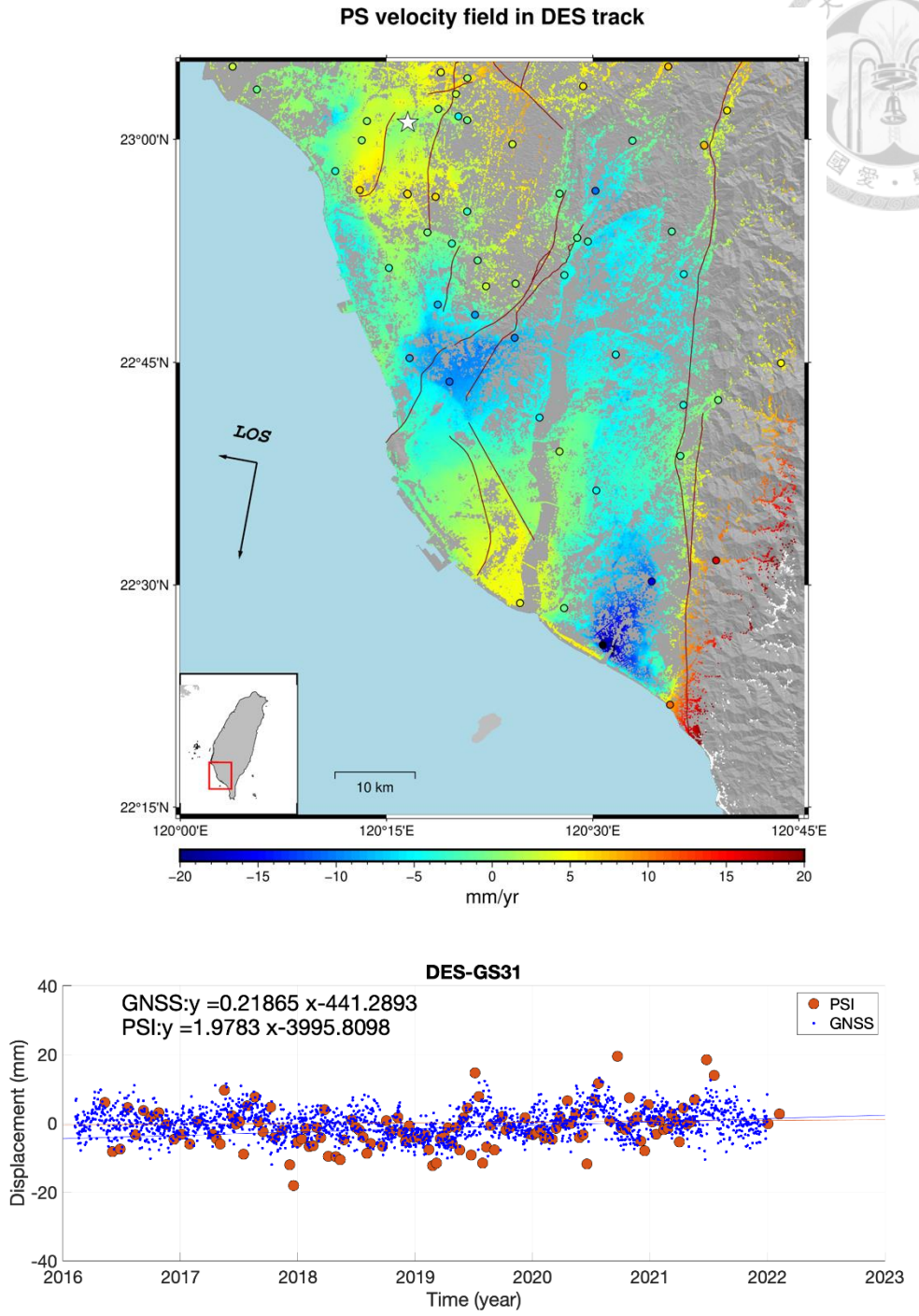

Fig. 4.7. PSInSAR result reference to GNSS observations and the comparison both data at GS31 station in DES track. The white star is the reference point (GS31 station). The dots are GNSS stations in the study area.

doi: 10.6342/NTU202400130

To correct PS observations by using GNSS observations, I calculated the correlation between two data (Fig. 4.8). According to Fig. 4.8, the GNSS observations and PS results show high-positive correlation (both directions larger than 0.7). Thus, I used GNSS observations to correct InSAR results by linear method. The step is as following:

- Take the average PS velocity within 200 meters around the GNSS stations
- Subtract the GNSS observations from the PS average velocity
- Interpolate the difference to the whole study area
- Raw PSs velocity plus difference

After the correction, the difference between GNSS and PSInSAR is lower than 5 mm/yr in both tracks (Fig. 4.9; Fig. 4.10).

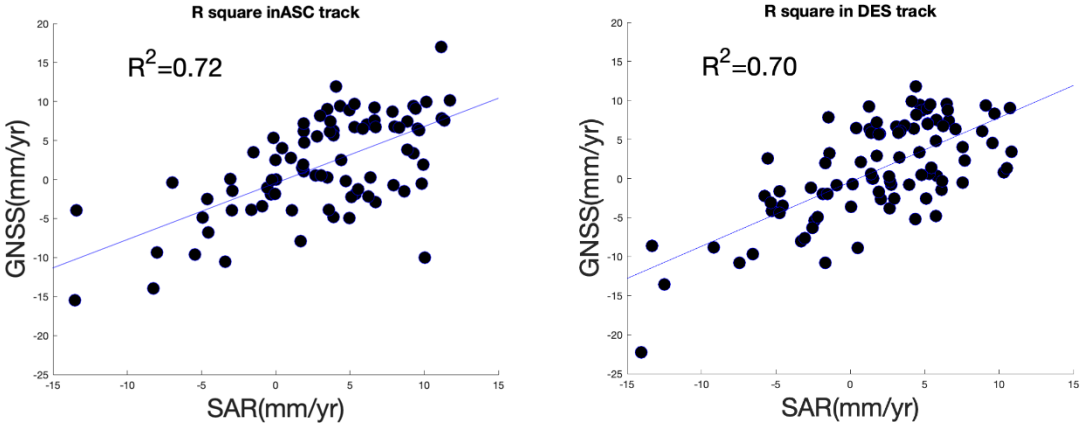

Fig. 4.8. The correlation between GNSS velocities in the LOS direction and PS velocities in the LOS direction. The left one is in ASC track. The right one is in DES track.

doi: 10.6342/NTU202400130

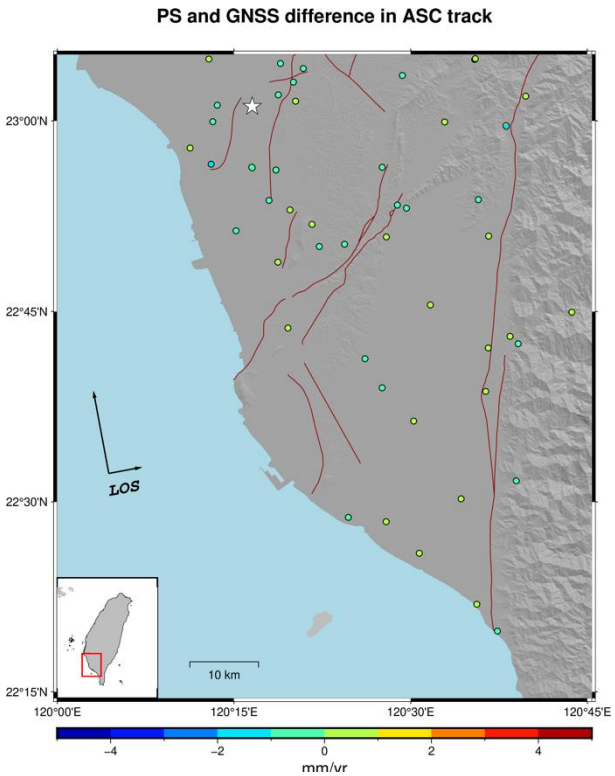

Fig. 4.10. The difference between GNSS and PSInSAR (mean value of PS within 200 meters) on GNSS stations in the ASC track.

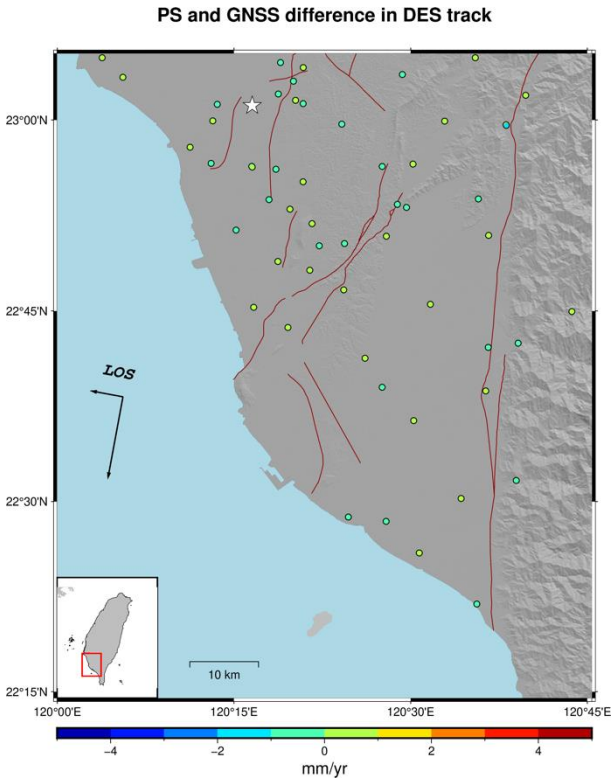

Fig. 4.9. The difference between GNSS and PSInSAR (mean value of PS within 200 meters) on GNSS stations in the DES track.

doi: 10.6342/NTU202400130

4.3 Decomposition

In the study, I processed two LOS directions of PS velocity fields. Because of having two directions InSAR observations, I can decompose the result into vertical (Fig. 4.11) and E-W (Fig. 4.12) directions. Here, I used the InSAR3Ddisp Matlab script derived by Lin (2021) (https://github.com/LiChiehLin/3D_decomposition), which presumes the contribution of N-S component is 0 because the orbital track of the satellite is nearly parallel to the N-S direction. The main contribution of active faults is the E-W direction so that the error caused by neglecting the N-S component is acceptable (Fuhrmann and Garthwaite, 2019). The resolution of decomposition is 100 meters in each grid. In the vertical direction, the velocity difference of the HCL fault and HKS fault is 6 mm/yr and 3 mm/yr, respectively. Dade Park, Ciaotou Park, TR railroad, and THSR railroad are crossed by the faults mentioned above. In the E-W direction, the velocity difference of the CKL fault, YC fault, and FS fault is 4 mm/yr, 4 mm/yr, and 3 mm/yr, respectively. TR railroad, THSR railroad, and Freeway systems are crossed by the fault mentioned above. The allowable time of these transportation systems will be discussed in the next Chapter.

doi: 10.6342/NTU202400130

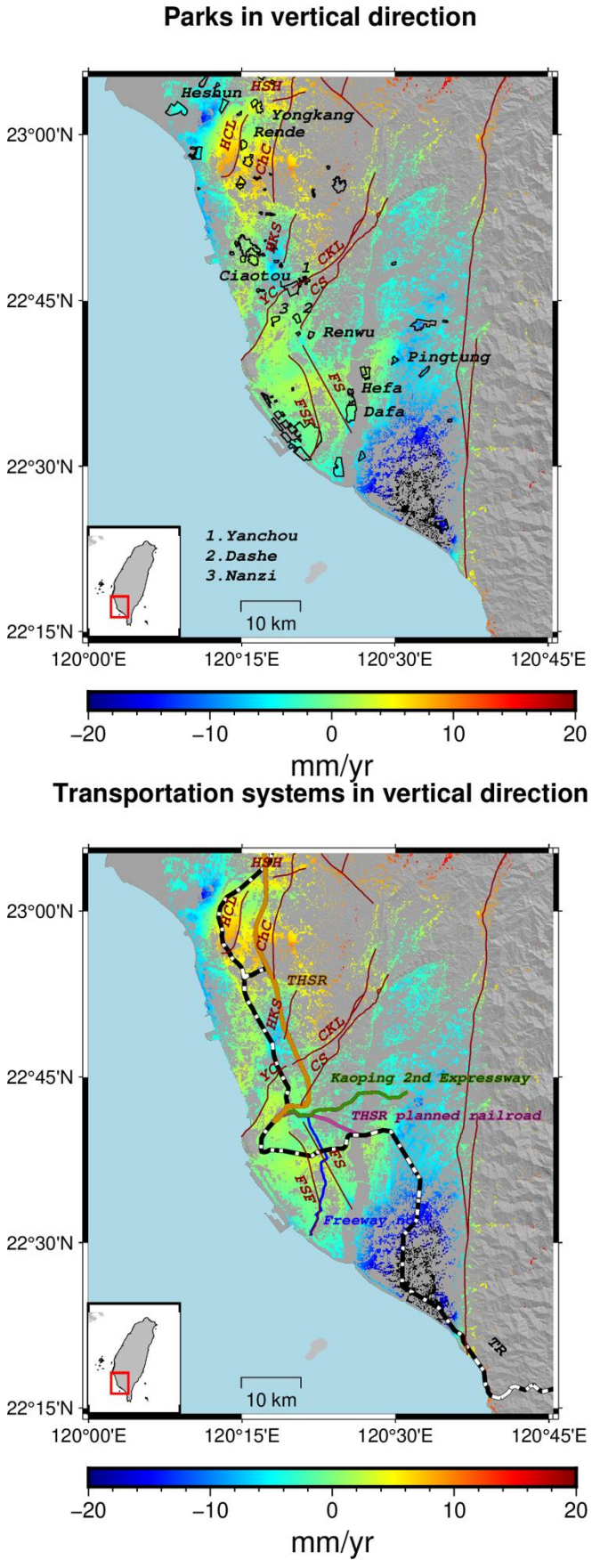

Fig. 4.11. Use two direction InSAR observations to decompose into velocity in vertical direction.

doi: 10.6342/NTU202400130

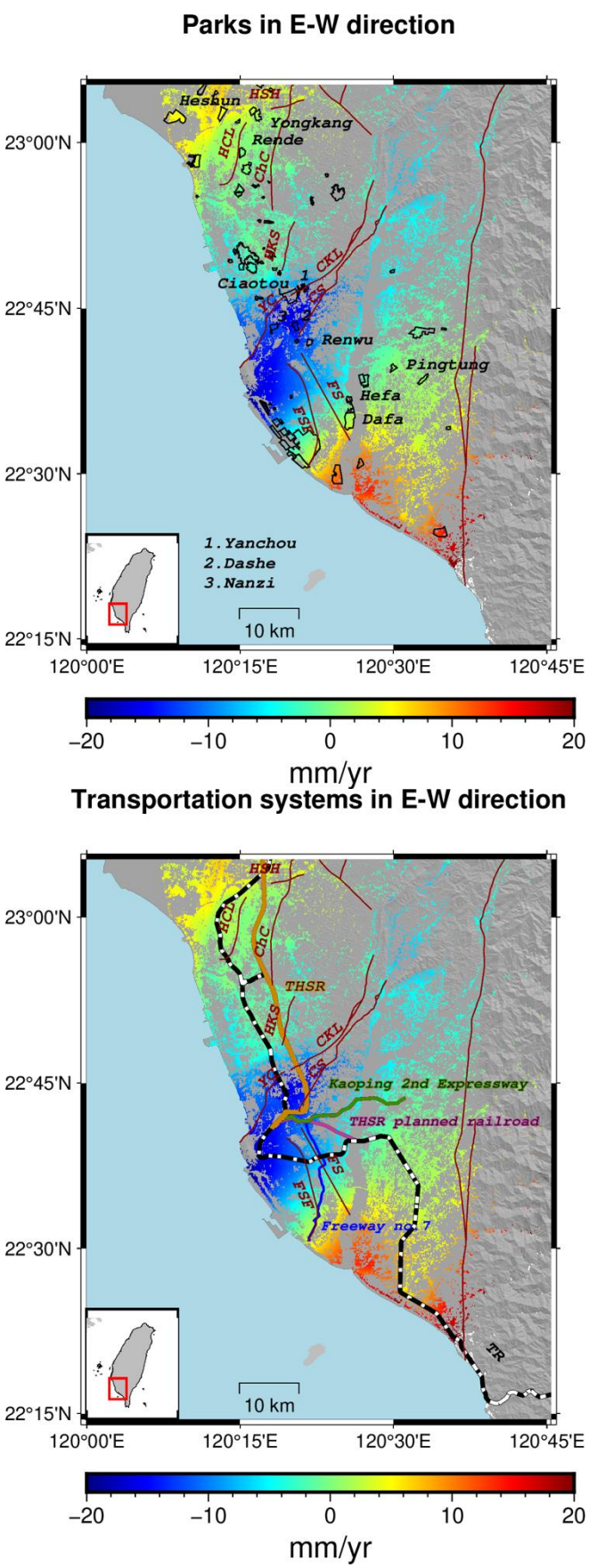

Fig. 4.12. Use two direction InSAR observations to decompose into velocity in E-W direction.

doi: 10.6342/NTU202400130

4.4 Comparison PS and leveling

To verify our PS result, I used leveling data derived by CGS (經濟部地質調查所，2022), which has time span from 2016 to 2022. The location of other leveling survey lines has sparse PS observations so we cannot have a good comparison. Therefore, I showed 2 leveling survey lines, which cross the HCL fault and HKS fault, respectively. The PS observation here is in the vertical direction, which is extracted along the leveling survey line.

The velocities between leveling and PS observations have the same patterns in both profiles. The difference of PS and leveling of most points along the profile line is lower than 1 mm/yr and the largest difference is lower than 3 mm/yr in both the HCL (Fig. 4.13) and HKS profile (Fig. 4.14). The fourth leveling point of HKS shows a larger error and has a different pattern compared to other points (Fig. 4.15).

doi: 10.6342/NTU202400130

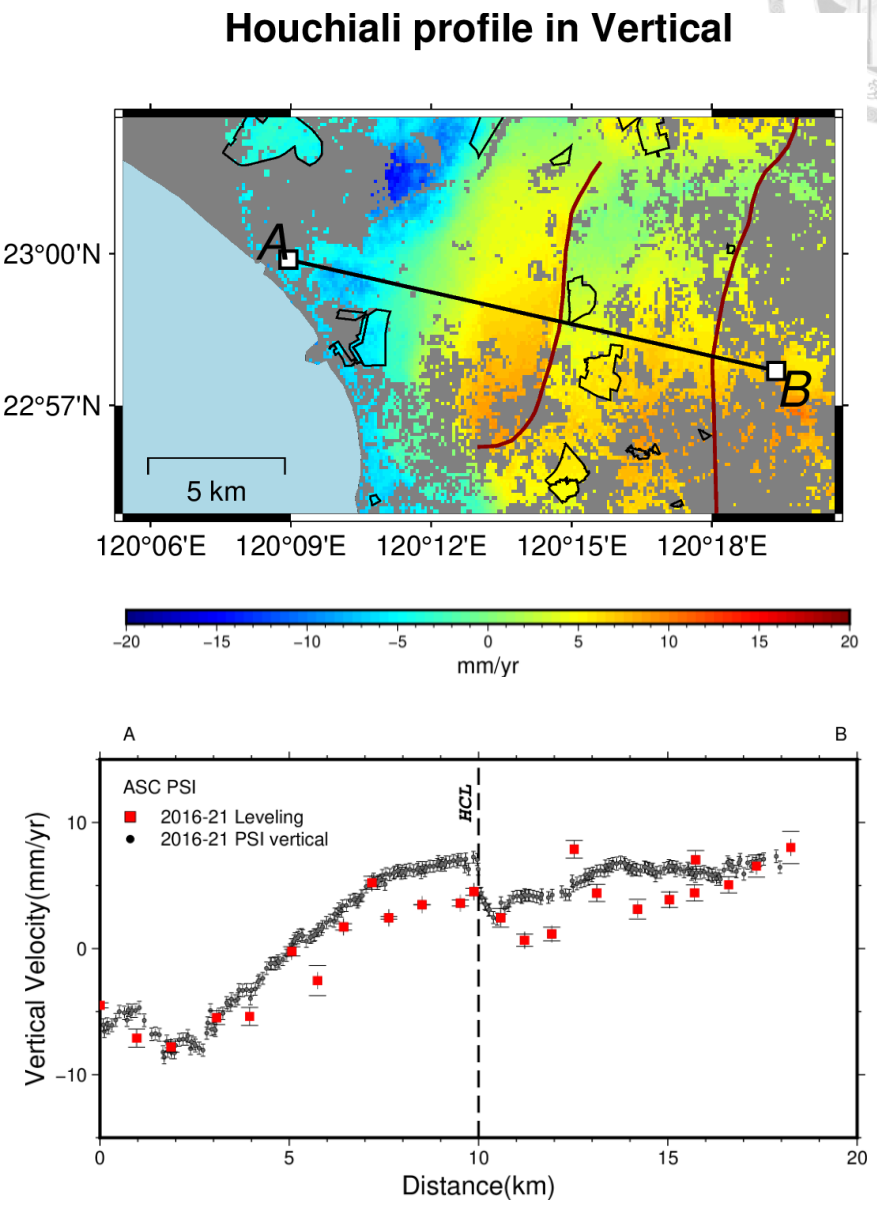

Fig. 4.13. The difference of PS and leveling in HCL profile. Top is the location of HCL profile. Bottom is the comparison of velocity of PS and leveling data.

doi: 10.6342/NTU202400130

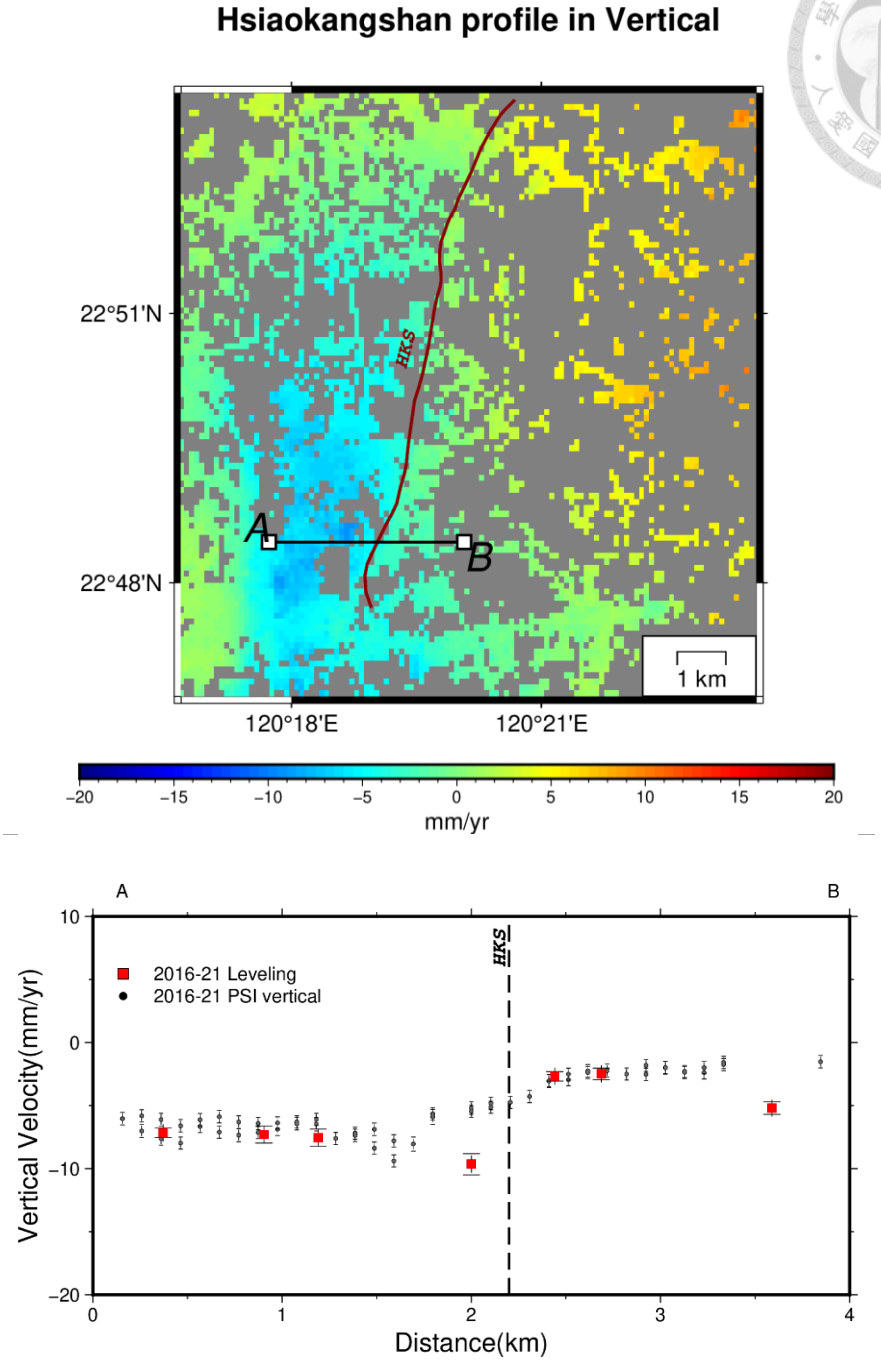

Fig. 4.14. The difference of PS and leveling in HKS profile. Top is the location of HKS profile. Bottom is the comparison of velocity of PS and leveling data.

doi: 10.6342/NTU202400130

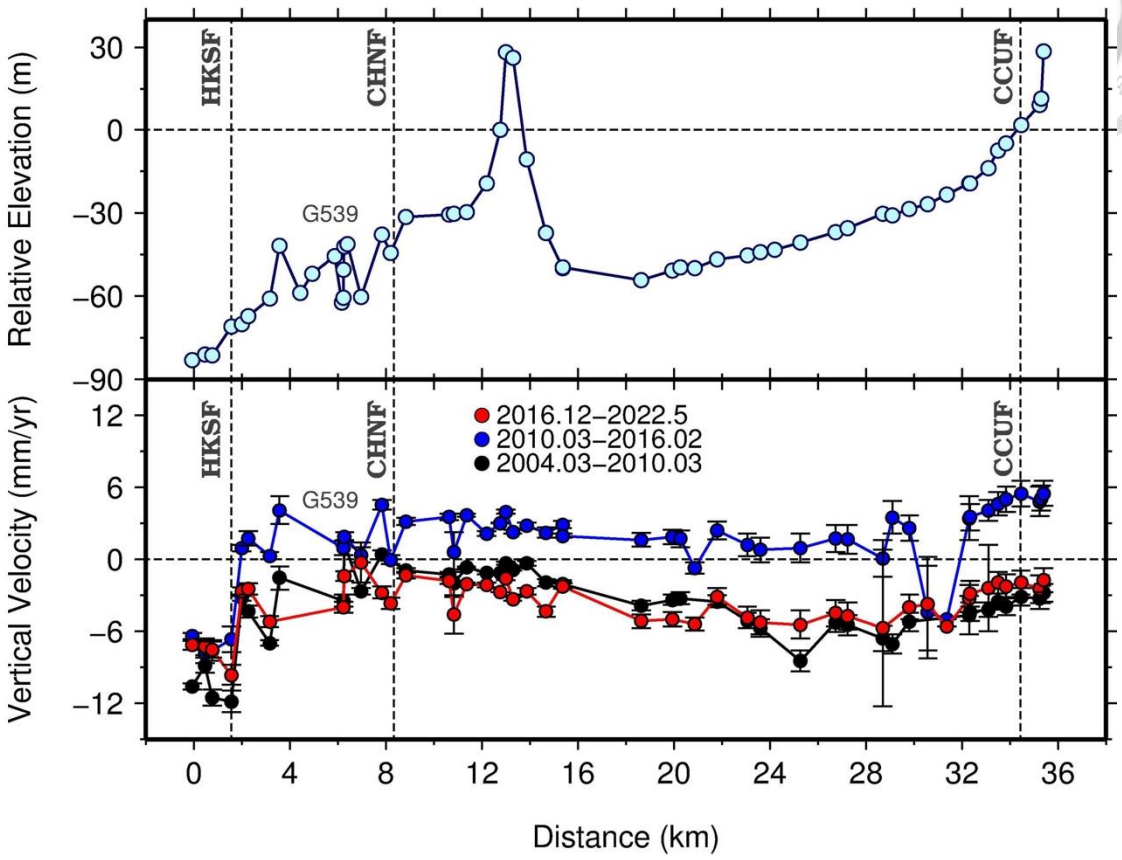

Fig. 4.15. The weird leveling point at different time span (經濟部地質調查所，2022).

doi: 10.6342/NTU202400130

Chapter 5 Discussion

5.1 Active fault motion

The PSInSAR result shows the velocity change along fault so that we can plot the profile line and time-series displacements. The velocity differences across some active faults have sharp changing.

In the middle of the Houchiali (HCL) fault, the velocity differences are about 4 mm/yr and 2 mm/yr in the vertical and E-W directions, respectively (Fig. 5.1), this value is lower than the previous study result, which is about 10 mm/yr (Huang et al, 2006). The time-series displacements along the profile line across the HCL fault shows the larger deformation on the hanging wall, but the velocity decrease from 7 (before 2019) to 3 mm/yr (after 2019) in the ASC track (Fig. 5.2).

The velocity difference along the THSR railroad across the CKL fault is about 6 mm/yr in the E-W direction within 1000 meters (Fig. 5.3). The time-series displacements along the THSR railroad across the CKL fault show the larger deformation on the hanging wall. The velocity remains constant are about 10 mm/yr and 9 mm/yr in the ASC and DES tracks, respectively (Fig. 5.4).

The velocity difference along the TR railroad across the YC fault is about 5 mm/yr in the E-W direction within 1000 meters (Fig. 5.5). And the time-series displacement trending shows that the hanging wall is faster than the foot wall in both track. The time-

doi: 10.6342/NTU202400130

series displacements along the THSR railroad across the YC fault shows the larger deformation on the hanging wall. The velocity difference is about 3 mm/yr in both ASC and DES tracks, and the velocity decreases about 2 mm/yr after 2019 (Fig. 5.6).

The pattern of decreasing on the HCL and YC faults is similar to the non-linear post-seismic pattern processed by the piecewise linear functions proposed in previous studies (Altamimi et al. 2007, 2011; Blick and Donnelly 2016; Klein et al. 2019). Although our time-series is without pre-seismic observations, we still can see the pattern of P1 before 2019 in Fig. 5.2, which shows the post-seismic curve so that we infer that this non-linear decay is finished in 2019. And if we want to better fit this kind of data in the future, we can subtract the inter-seismic velocities, which are estimated by using neighboring GNSS stations from the post-seismic time series (Yu and Kuo, 2001; Chen et al., 2020).

doi: 10.6342/NTU202400130

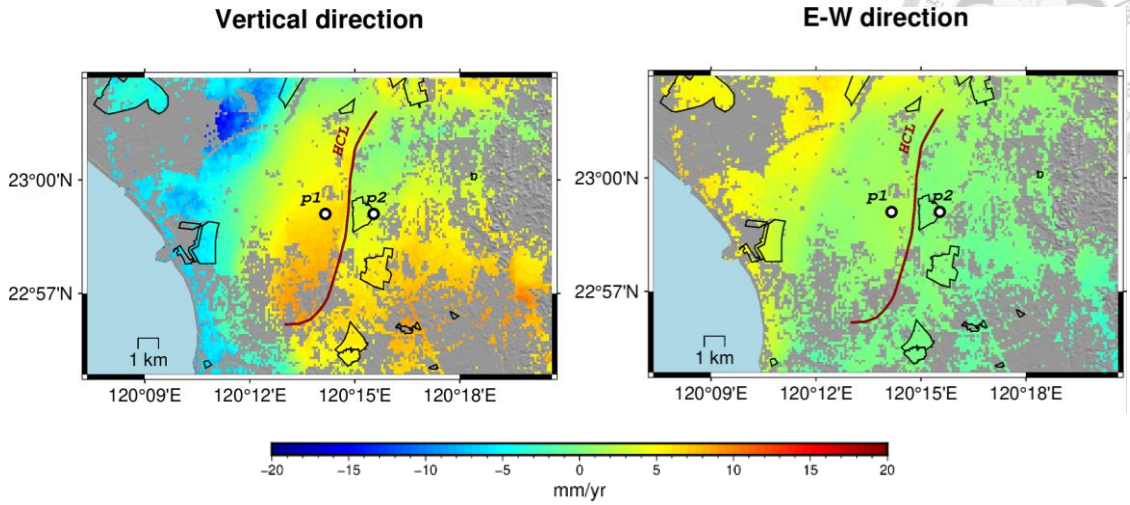

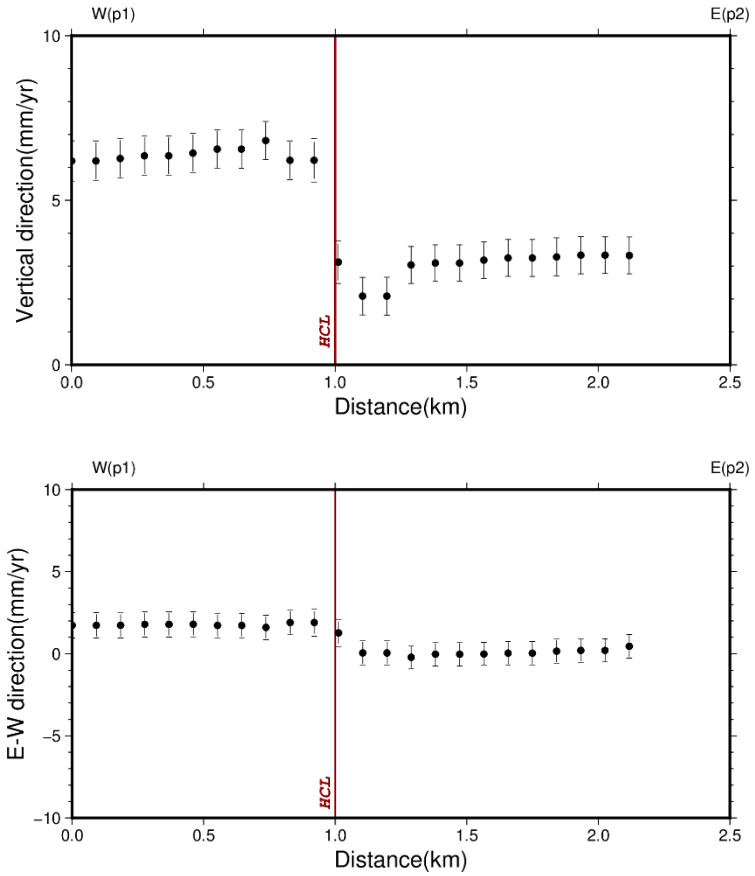

Fig. 5.1. The velocity change along p1-p2 profile line at HCL fault

doi: 10.6342/NTU202400130

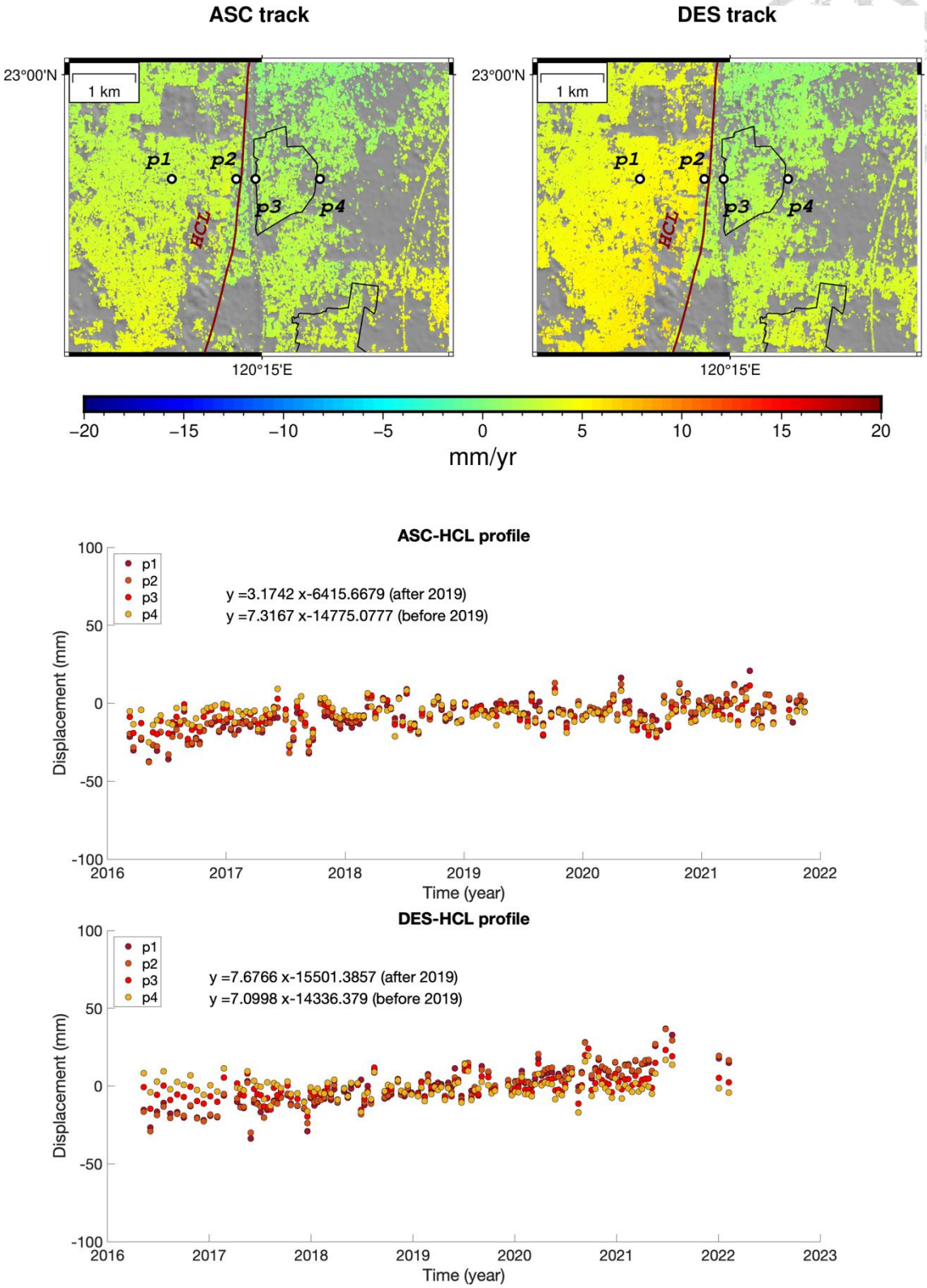

Fig. 5.2. The time-series displacements at p1 to p4 which are across the HCL fault in LOS direction.

doi: 10.6342/NTU202400130

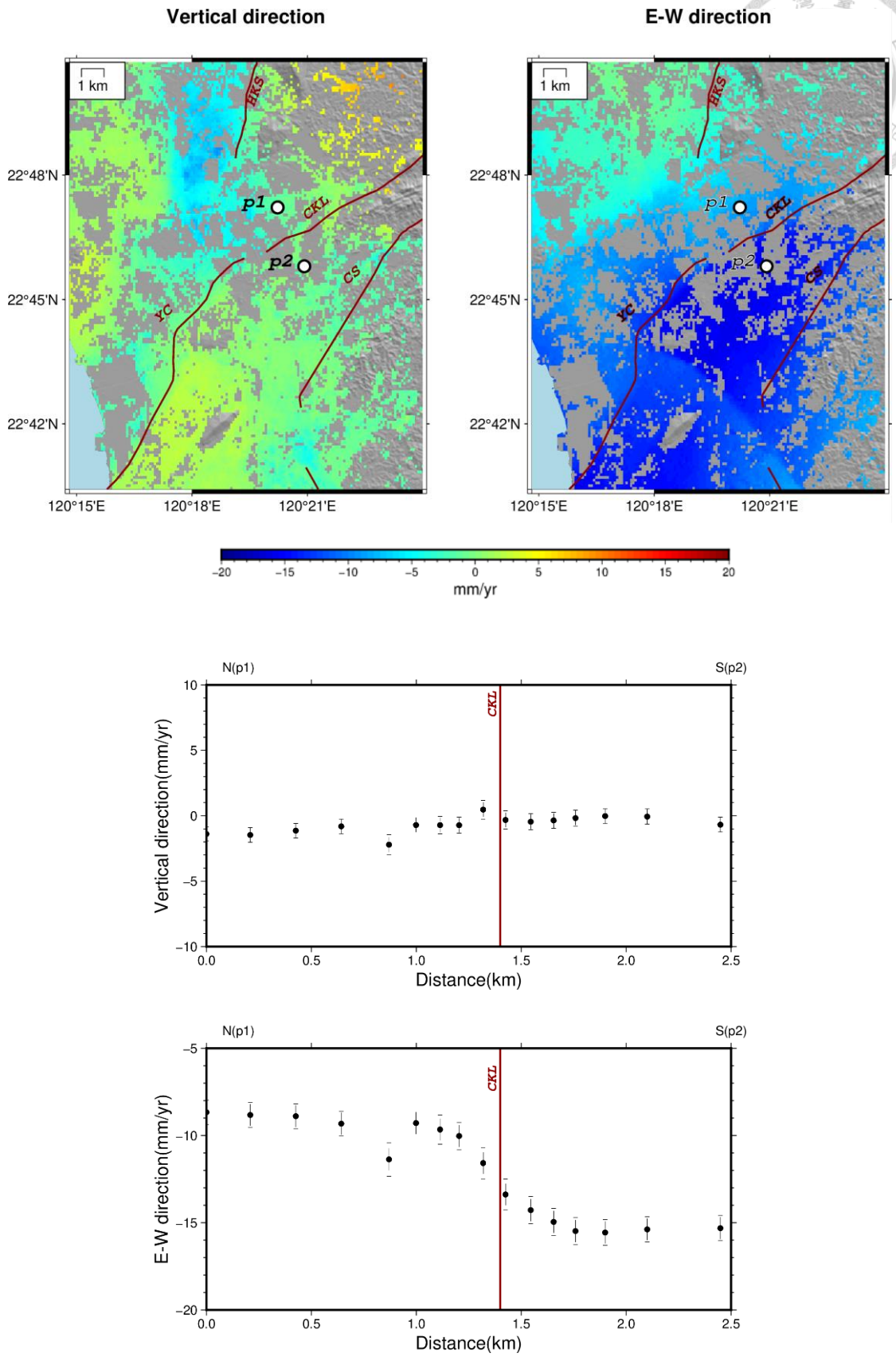

Fig. 5.3. The velocity change along p1-p2 profile line at CKL fault

doi: 10.6342/NTU202400130

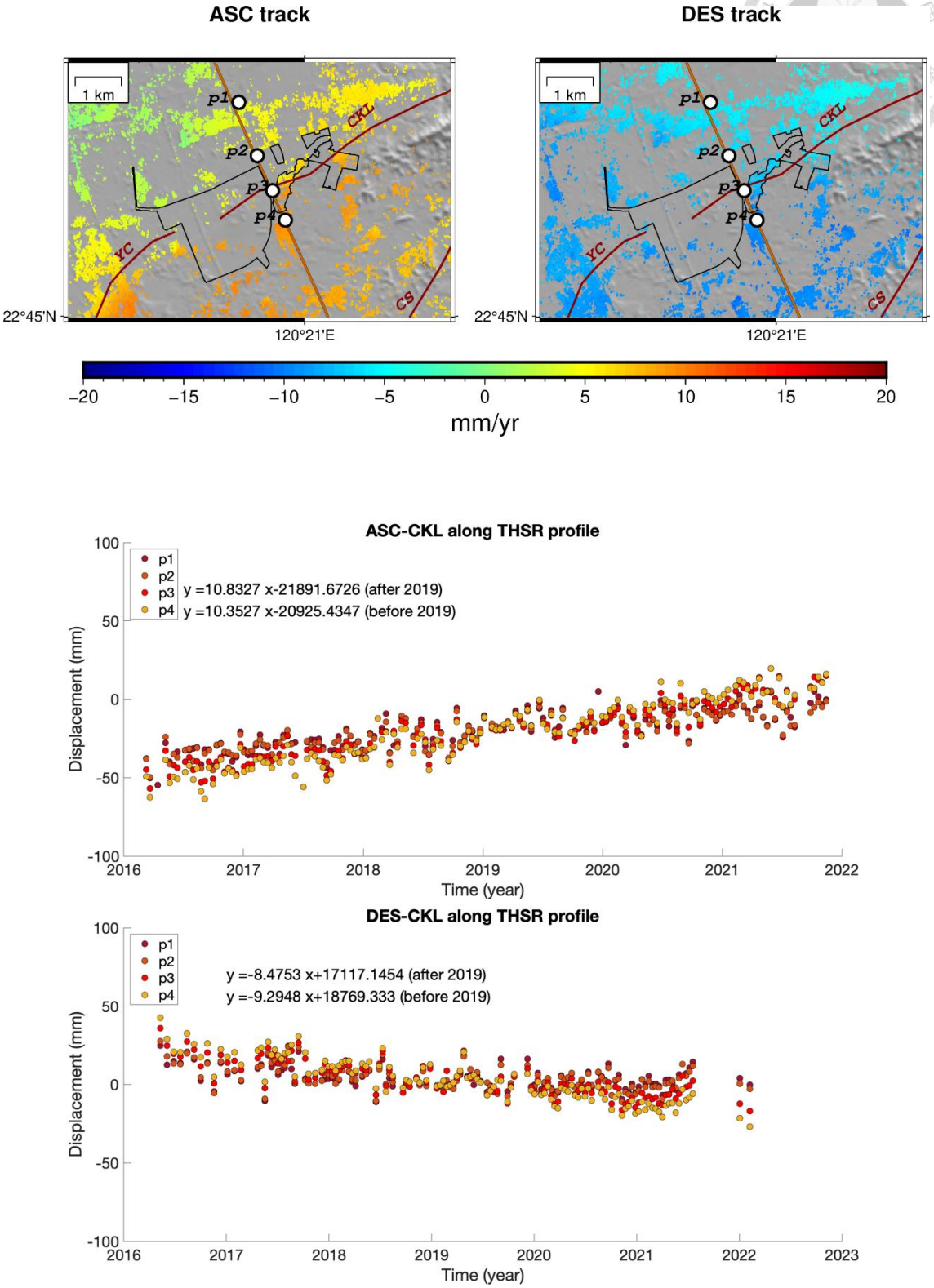

Fig. 5.4. The time-series displacements at p1 to p4 which are across the CKL fault in LOS direction.

doi: 10.6342/NTU202400130

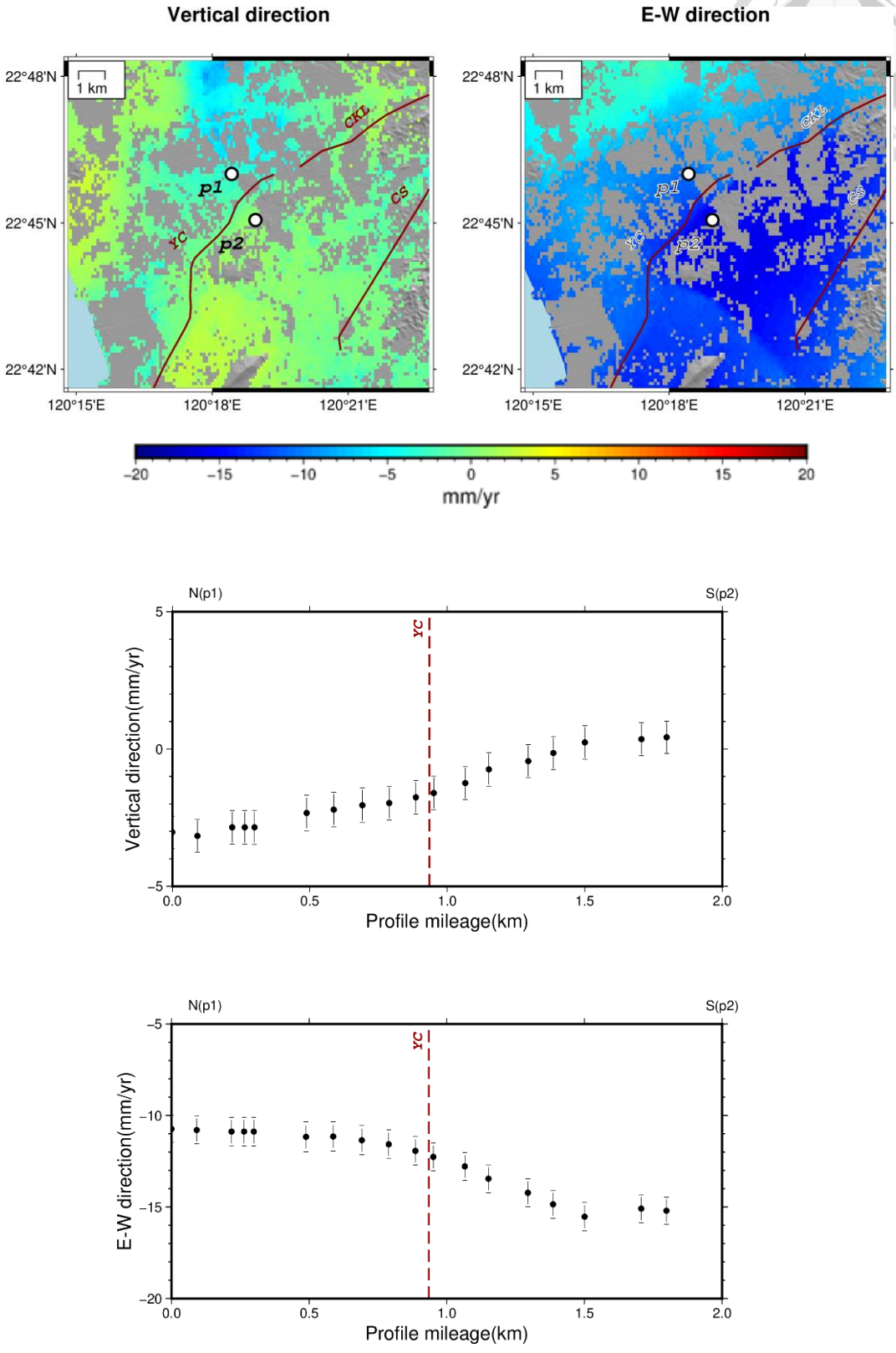

Fig. 5.5. The velocity change along p1-p2 profile line at YC fault

doi: 10.6342/NTU202400130

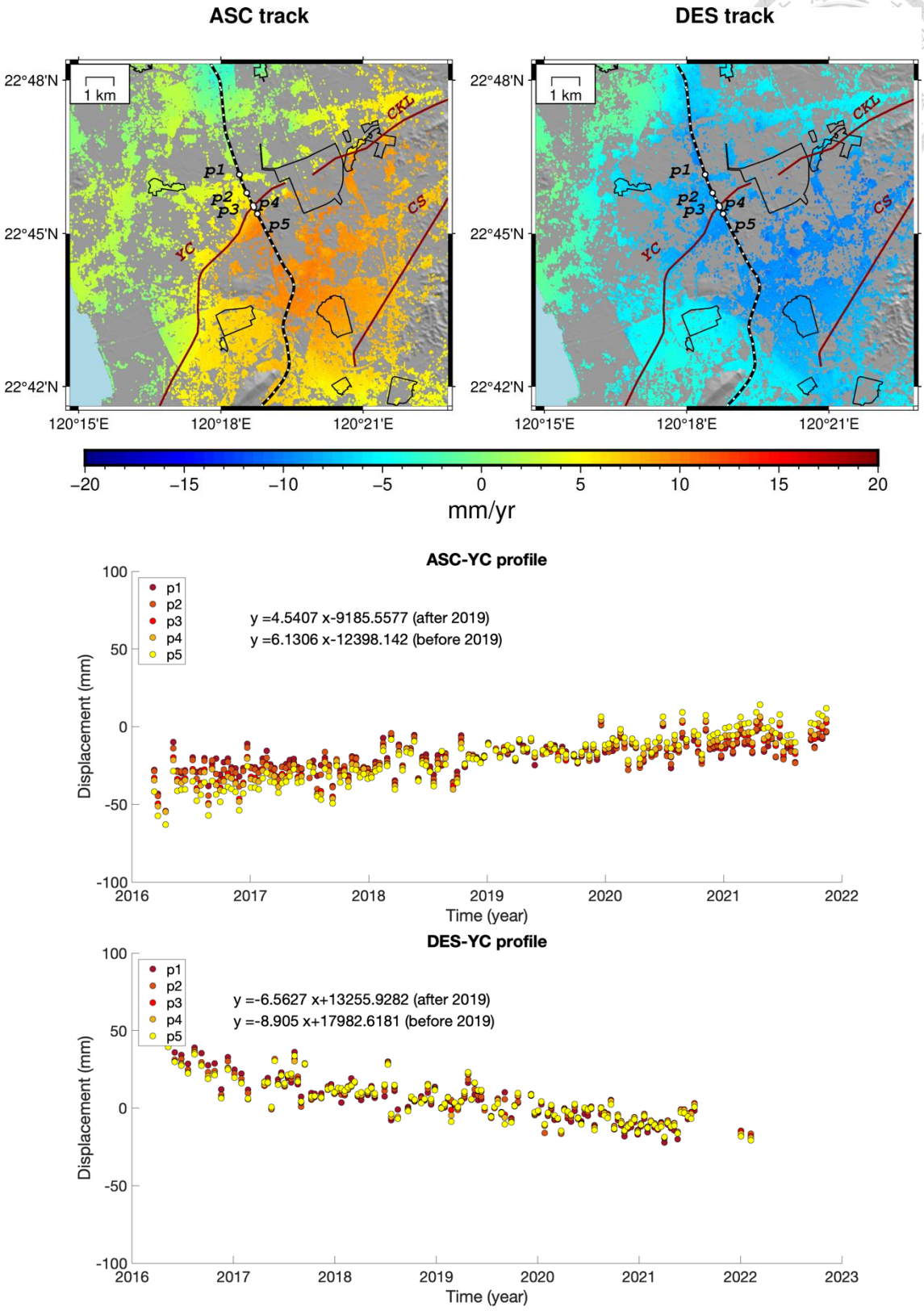

Fig. 5.6. The time-series displacements at p1 to p5 which are across the YC fault in LOS direction.

doi: 10.6342/NTU202400130

5.2 Infrastructure deformation

5.2.1 Transportation systems

The transportation systems in our study area include Taiwan High Speed Rail (THSR), Taiwan Railway (TR), and Freeway. The observations show the velocity difference at some places on these transportation systems. In this section, I will compare our result with the allowable deformation of different pavements.

THSR

86% of the THSR tracks are J-slab tracks with a gauge of 1435 mm. This kind of track is laid on top of prestressed concrete, which can no longer withstand tensile loads, especially in surface deformation area. The allowable deformation limits (容許變形值) of J-slab track are 50 mm/ 100 meters and 65 mm/ 100 meters in vertical and horizontal directions, respectively (THSR, 2011).

The deformation pattern of THSR railroads, according to the PS result and decompose result, is near the HKS, CKL, and FS faults. (Fig. 5.7; Fig. 5.8). Therefore, I plotted the profile along the THSR railroad (Fig. 5.9), and the time-series displacements on different side of these velocity changing boundaries. The distance chosen between the two points is 100 meters. In THSR-1, the THSR railroad across the HKS fault shows the main contribution is a vertical component, and the velocities difference is about 1 mm/yr (Fig. 5.10). In THSR-2, the THSR railroad across the CKL fault, shows the main

doi: 10.6342/NTU202400130

contribution is the E-W component, and the velocities difference across the CKL fault is about 6 mm/yr (Fig. 5.11). In THSR-3, although there is no fault trace cut through the THSR railroad, there still have sharp velocities change. The main contribution is the E-W component, and the velocities difference here decreases to about 2 mm/yr (Fig. 5.12).

The entire Taiwan High Speed Rail (THSR) railroad in our study area is constructed in the viaduct type with prestressed concrete. According to the allowable deformation limits of the track with a gauge of 1453 mm (Fig. 5.13), the equation of allowable deformation in horizontal direction is as following:

$$T_h = \frac{M_h}{V_h}, M_h = \frac{1.3 \times L}{2000}$$

where T_h is the time required for the horizontal deformation to reach the allowable limit, M_h is allowable deformation is horizontal direction, and L is the bridge span. The equation of allowable deformation in the vertical direction is as following:

$$T_v = \frac{M_v}{V_v}, M_v = \frac{L}{2000}$$

where T_v is the time required for the horizontal deformation to reach the allowable limit and M_v is allowable deformation is the horizontal direction.

To verify our result, I compare the result with a previous study (Li, 2020), they use the GNSS observations and leveling data from THSR company to calculate the allowable time along the railroad which cross the CKL fault (Fig. 5.14) (Table 5.1). I neglected the

doi: 10.6342/NTU202400130

points, which have larger error than observations. At the T331K+500~T331K+600 (cross CKL fault), it will reach to allowable deformation within 7 years.

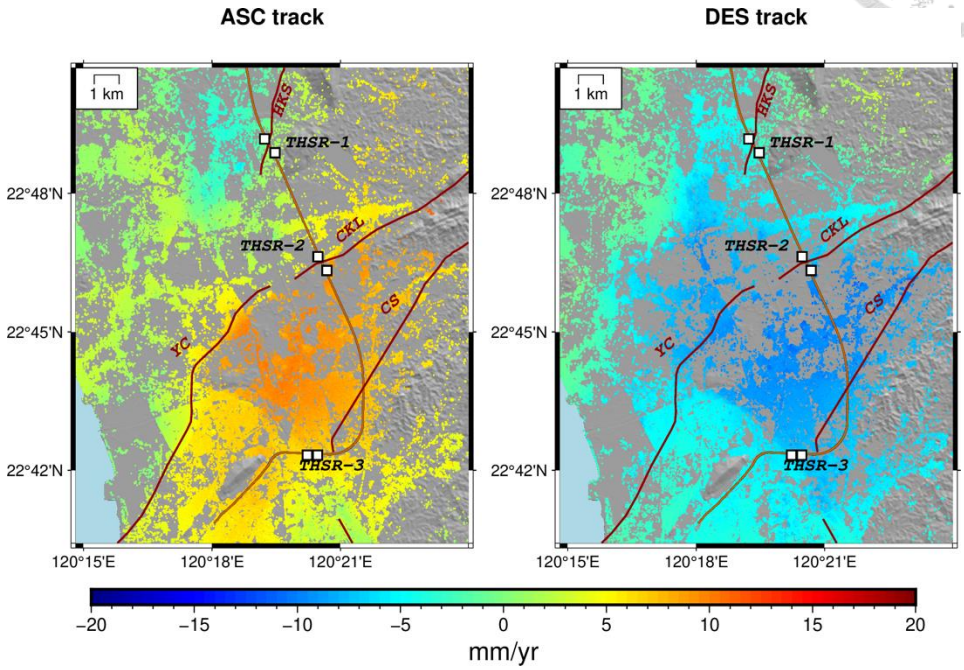

Fig. 5.8. PSInSAR result near THSR railroad with sharp velocity change in LOS direction. Left is ASC track. Right is DES track. The dark orange line is THSR railroad. The white rectangular is the time-series location. CS is the Chishan fault.

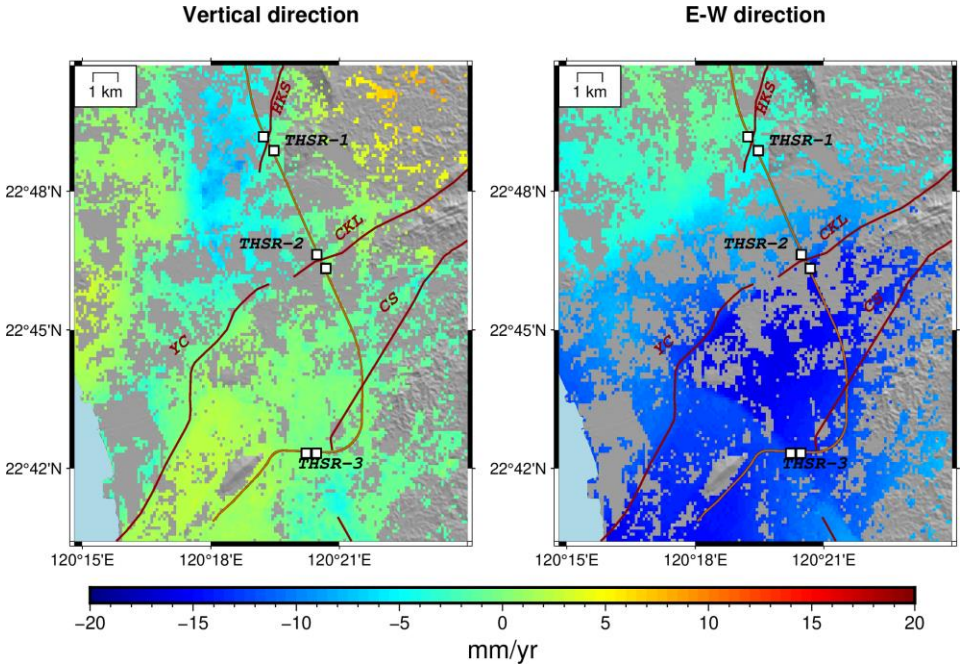

Fig. 5.7. The velocity field near THSR railroad in vertical and E-W directions.

doi: 10.6342/NTU202400130

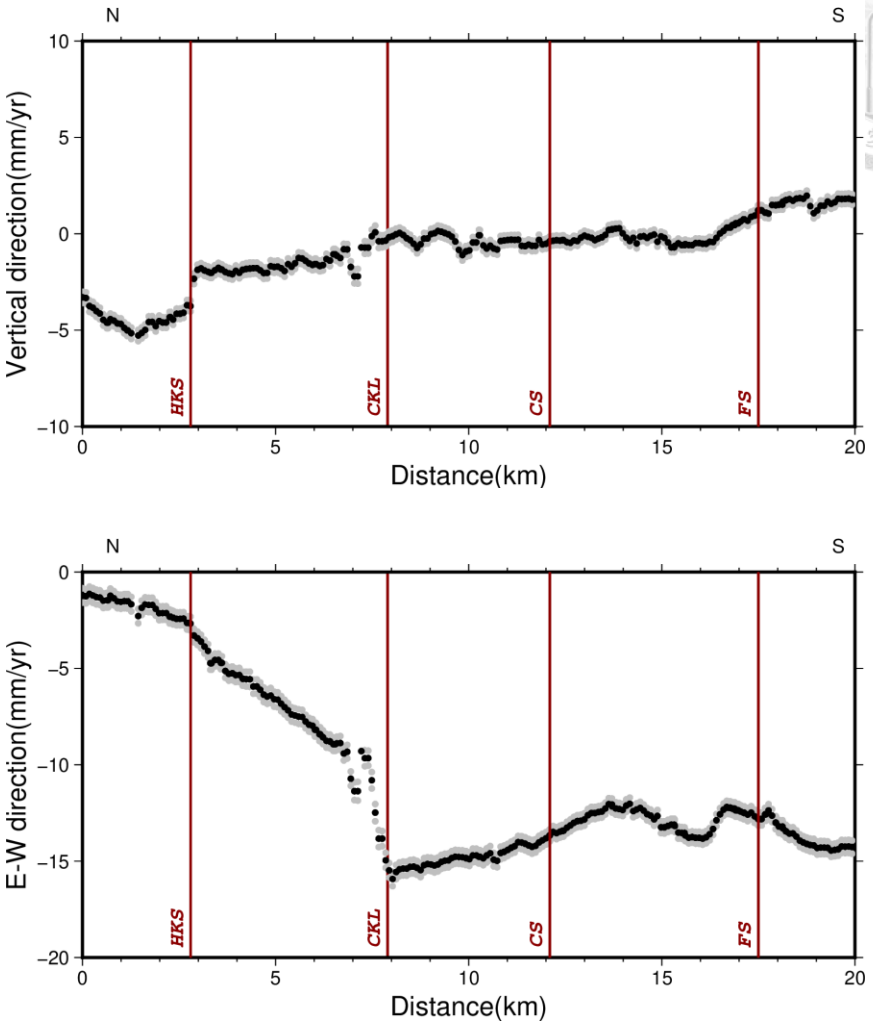

Fig. 5.9. The profile along THSR railroad. From 323K to 347K is from N to S direction. The black one is velocity. The gray one is error.

doi: 10.6342/NTU202400130

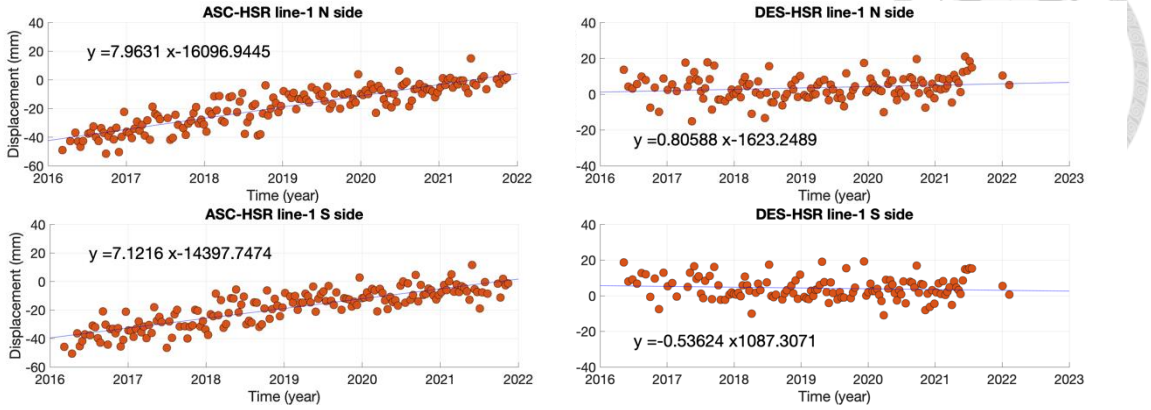

Fig. 5.10. The time-series displacement in THSR-1

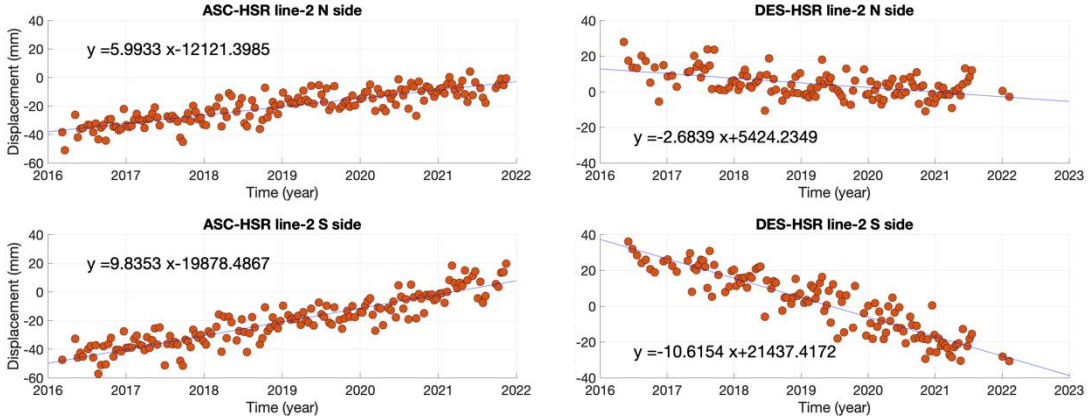

Fig. 5.11. The time-series displacement in THSR-2

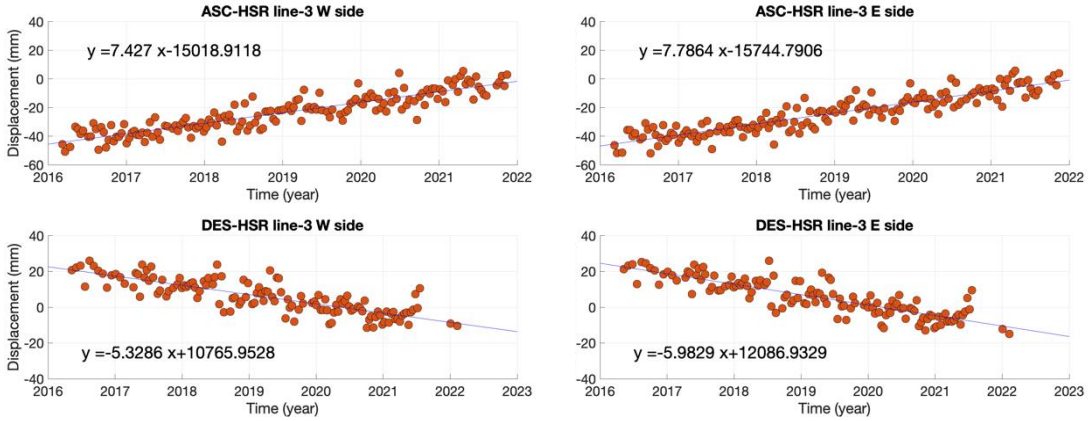

Fig. 5.12. The time-series displacement in THSR-3

doi: 10.6342/NTU202400130

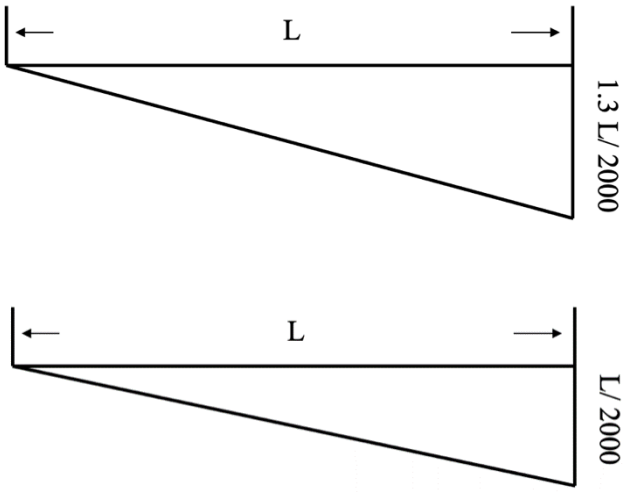

Fig. 5.14. The allowable deformation limits of THSR track (gauge: 1435 mm). Top is vertical direction. Bottom is horizontal direction. L is the bridge span.

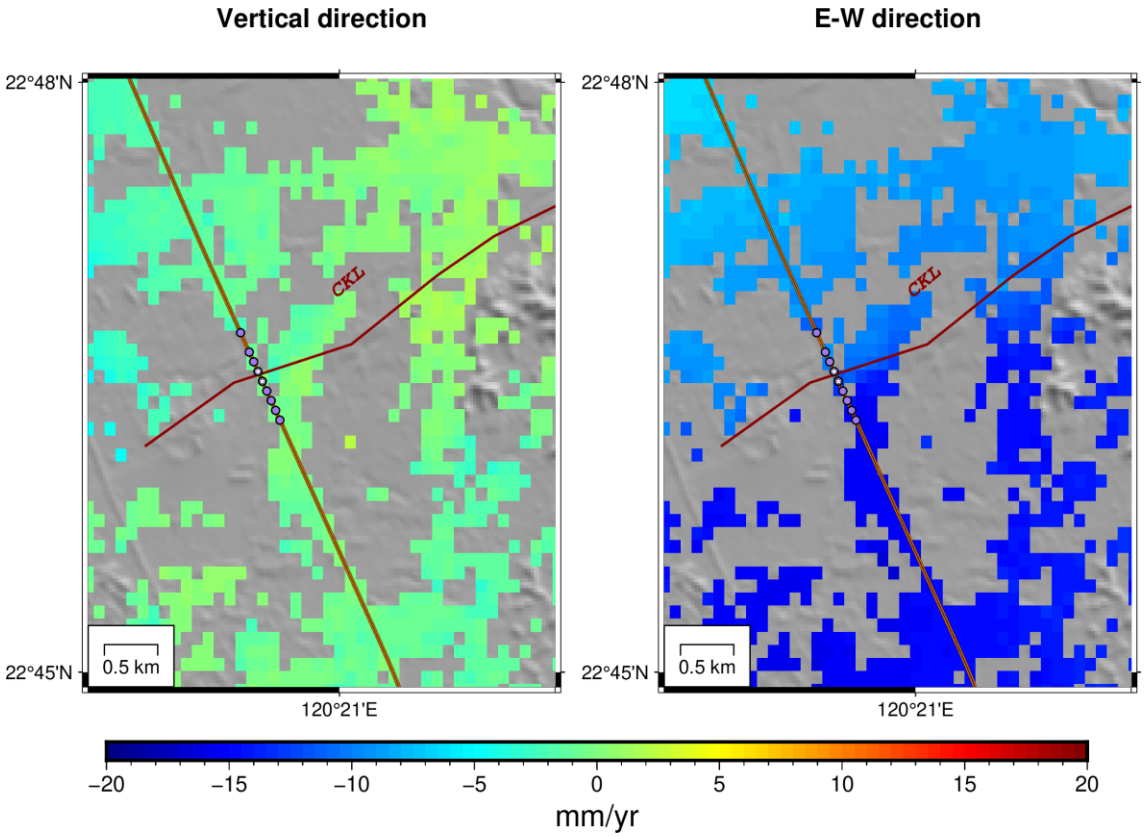

Fig. 5.13. The location of the THSR mileage. Purple circle is THSR mileage. White star is T331+500~T331+600.

doi: 10.6342/NTU202400130

Table 5.1: The horizontal, vertical deformation, and allowable time on the CKL section. The values in parentheses represent the allowable time from Li (2020).

	Horizontal (mm)		Vertical (mm)		Time (year)	
THSR mileage	2016~2019 (Li, 2020)	2016~2021 (This study)	2016~2019 (Li, 2020)	2016~2021 (This study)	T_h	T_v
331K+100		0.0 ± 0.8		0.0 ± 0.8		
331K+300	0.0 ± 0.1	1.0 ± 0.8	0.0 ± 1.1	0.1 ± 0.6	26 (20)	
331K+400	0.4 ± 0.1	0.2 ± 0.8	0.1 ± 1.1	0.0 ± 0.6		
331K+500	1.3 ± 1.0	3.5 ± 0.9	0.3 ± 1.1	1.5 ± 0.6	7 (6)	14
331K+600	3.1 ± 0.1	2.2 ± 0.8	0.4 ± 1.1	1.0 ± 0.6	12 (16)	20
331K+700	0.9 ± 0.1	1.8 ± 0.8	0.2 ± 1.2	0.7 ± 0.7	15 (21)	
331K+800	1.0 ± 0.2	3.0 ± 0.9	0.1 ± 1.2	2.4 ± 0.6	9	9

TR

The TR railroad (track) is mainly composed of ballast, crossties, subgrade, and track assembly fittings. According to the safety regulations for track facilities, the condition of crossties will affect the overall safety of the track. When the deformation of the track reaches to certain level, it will cause damage to the crossties (Federal Railroad Administration (TRA), 2017). In this section, I will discuss the deformation limits of TR's track with a gauge of 1067 mm.

In TR railroad, I also focus on the sections that with obvious velocity difference boundaries (Fig. 5.15; Fig. 5.16). I plotted the profile along the TR railroad from 4 km north of the YC fault to the right bank of the Kaoping River (Fig. 5.17). There are many velocity changing boundaries so I plotted the time-series displacements on different sides of them. The TR-1 across the Youchang fault shows sharp velocity change, which has a

doi: 10.6342/NTU202400130

horizontal contribution, is about 4 mm/yr on the different sides of the fault within 100 meters (Fig. 5.18). In TR-2, which has a horizontal contribution, shows the velocity difference across the north of the FS fault. The velocity changing is about 3 mm/yr within 100 meters (Fig. 5.19). In TR-3, which has a horizontal contribution, there is about a 1 mm/yr difference located at the east side of the FS fault (Fig. 5.20).

The railroad in our study area includes the Western Trunk Line (西部鐵路縱貫線) and the Pingtung Line. The deformation of the railroad can be divided into different types, including level, longitudinal level, and alignment (Table. 5.2; The regulations of railway construction, Taiwan Railway MOC). Here I only discuss longitudinal level and alignment in this study. If the displacements accumulated by the same velocity rate, it will reach the allowable limit within 10 years in both longitudinal level and alignment types.

doi: 10.6342/NTU202400130

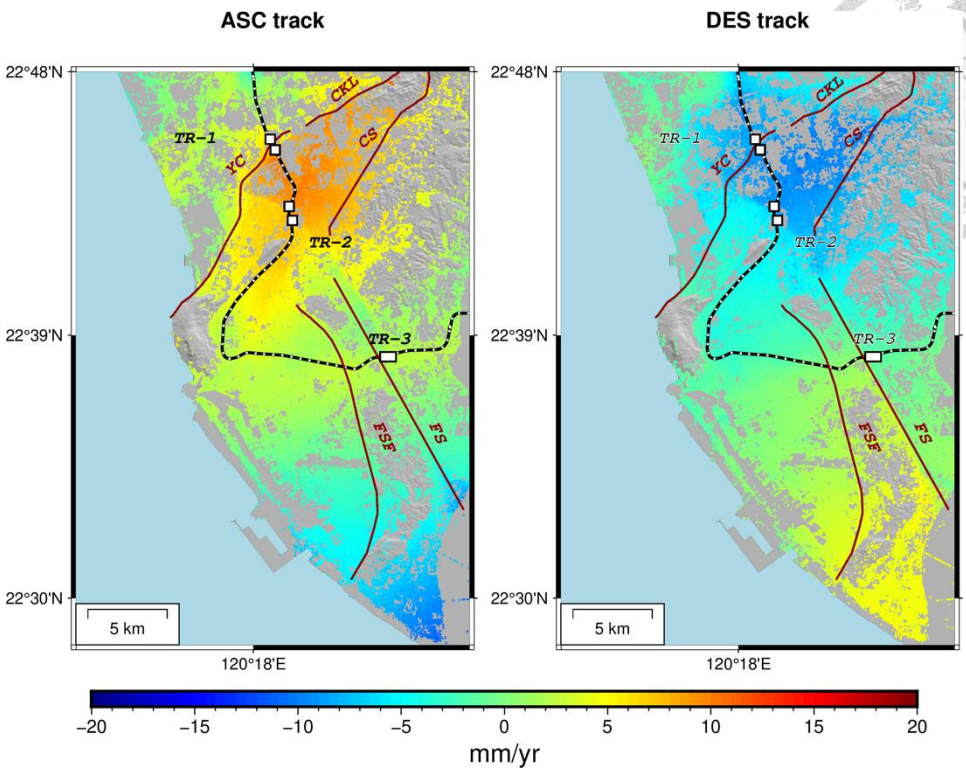

Fig. 5.15. PSInSAR result near TR railroad with sharp velocity change in LOS direction. Left is ASC track. Right is DES track. The black line is TR railroad. The white rectangular is the time-series location. FSF is the Fengshan hills frontal structure. FS is the Fengshan fault.

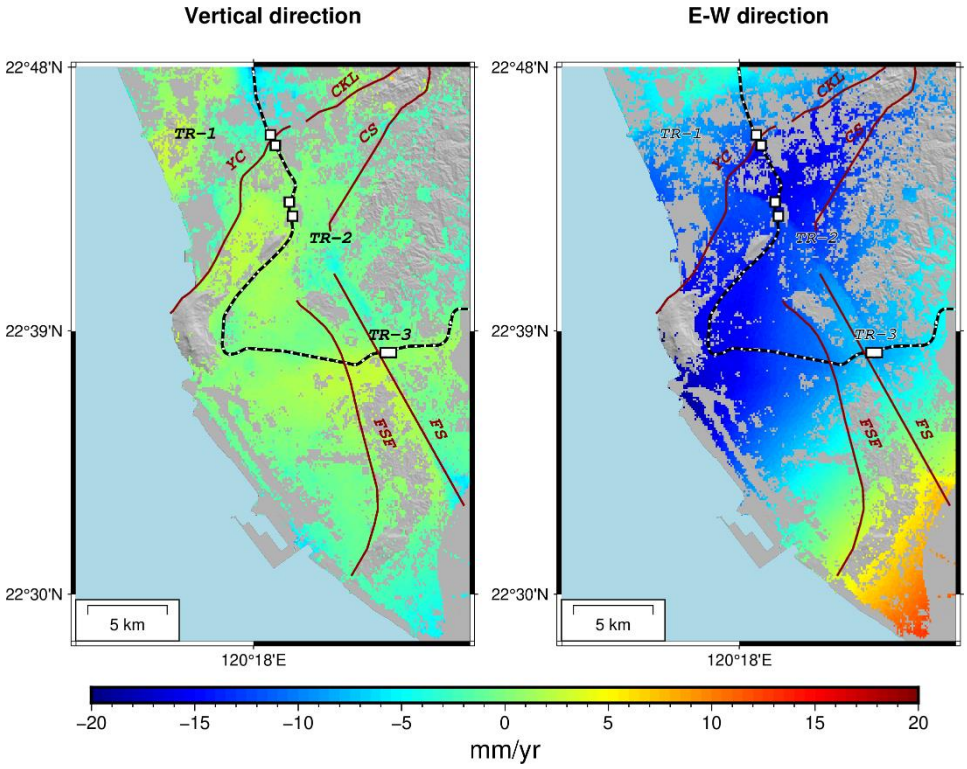

Fig. 5.16. The velocity field near TR railroad in vertical and E-W directions.

doi: 10.6342/NTU202400130

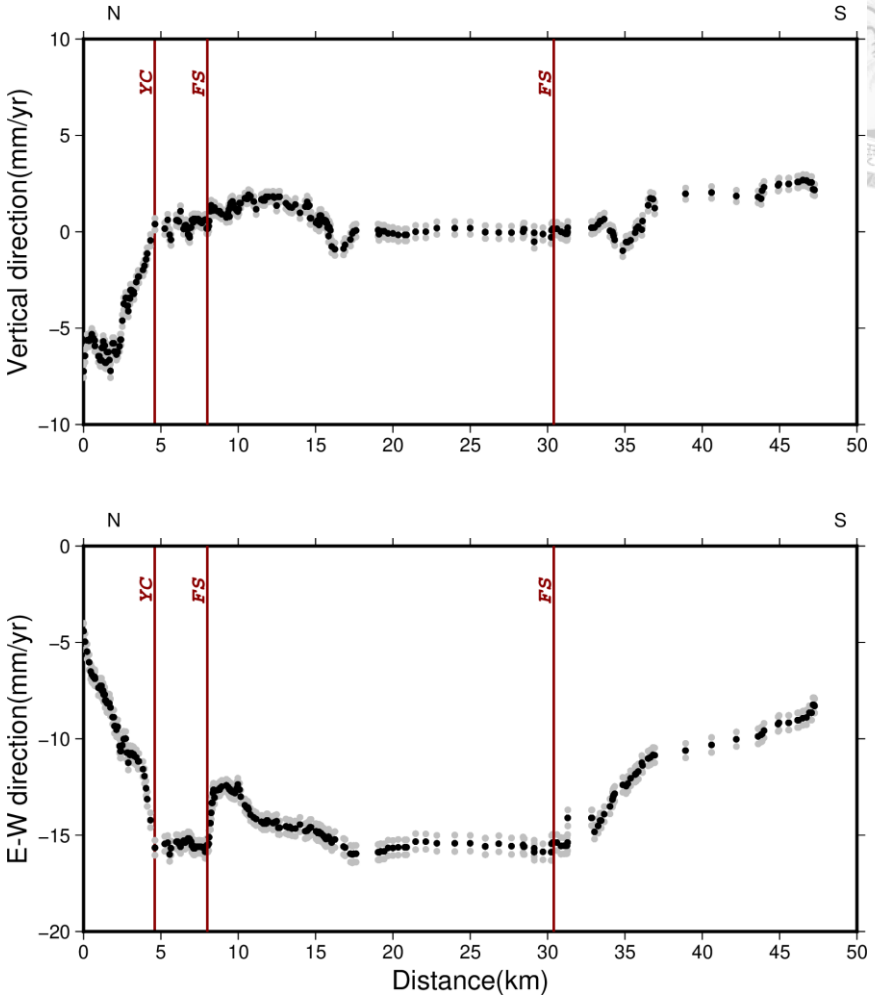

Fig. 5.17. The profile along TR railroad. From 0K to 50K is from N to S direction.

doi: 10.6342/NTU202400130

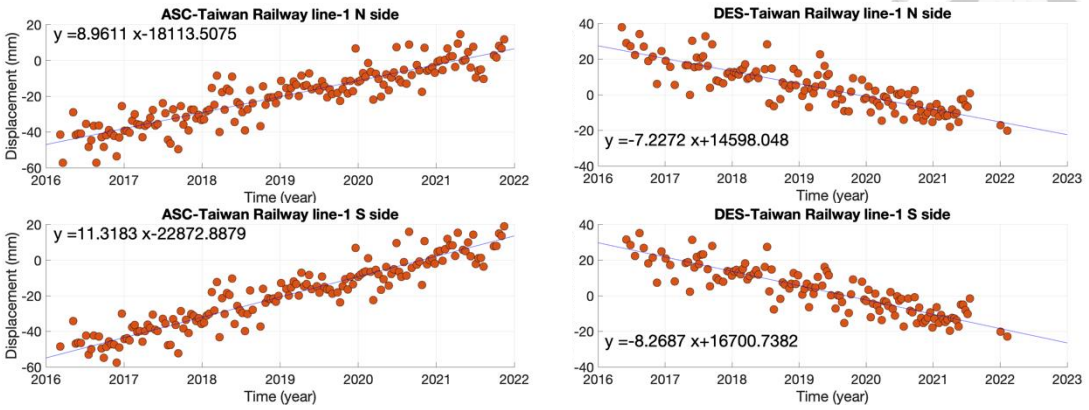

Fig. 5.18. The time-series displacement in TR-1

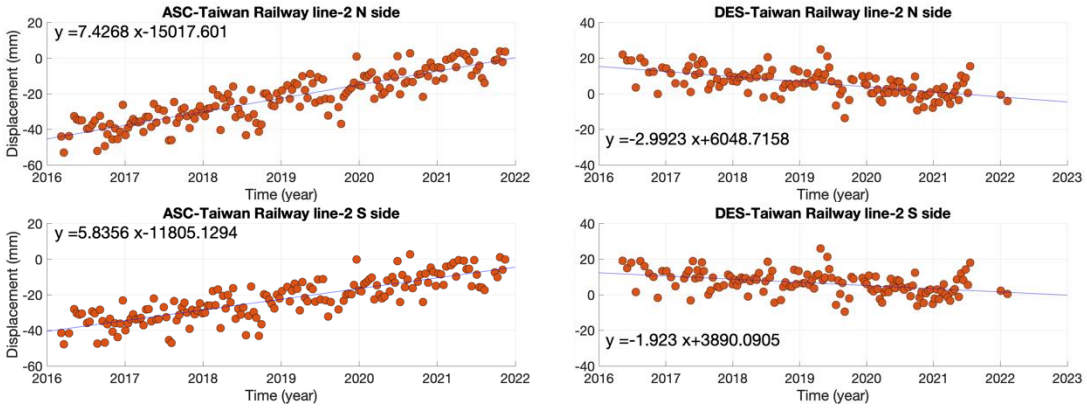

Fig. 5.19. The time-series displacement in TR-2

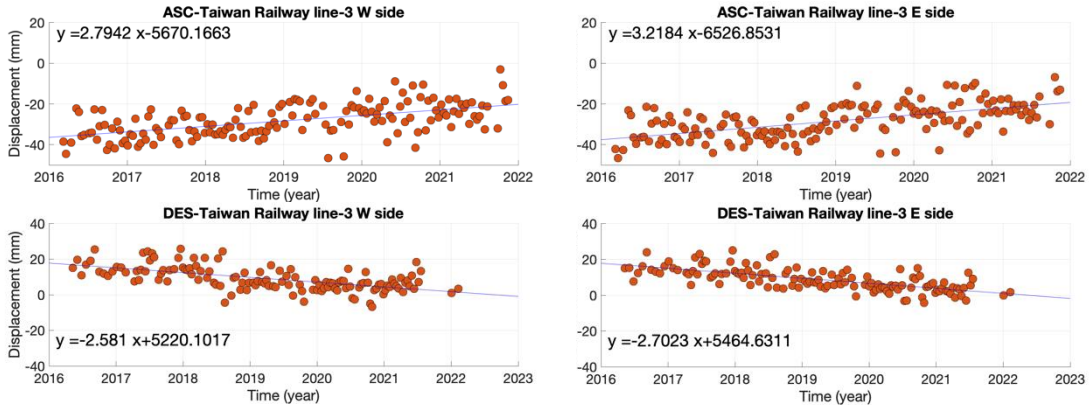

Fig. 5.20. The time-series displacement in TR-3.

doi: 10.6342/NTU202400130

Table 5.2: The allowable deformation and deformation types of rail track (gauge: 1067 mm), Taiwan Railway Administration (2010).

	Allowable deformation (mm)	Our result	Schematic
Level	7	No data	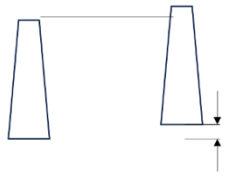
Longitudinal level	7	0.8	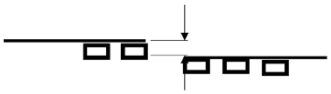
Alignment	7	1.1	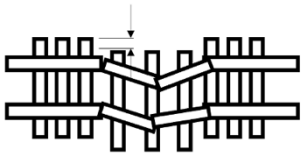

doi: 10.6342/NTU202400130

Planning route

In SW Taiwan, except for the route mentioned above, there still planned transportation systems that will be built in the future, such as Freeway no.7 (N7), Kaoping Expressway (KP-ex), and THSR Pingtung system (THSR-P).

In the N7 system, I also focus on the sections with obvious differences (Fig. 5.21; Fig. 5.22). I plotted the profile line along the N7 route, which shows the velocity changing boundaries near the FS fault trace (Fig. 5.23) so that I plotted the time-series displacement at different sides of the FS fault. The N7-1 has a sharp velocity difference east of the FS structure, showing the main contribution in the horizontal direction of about 3 mm/yr within 200 meters (Fig. 5.24). In N7-2, the velocity difference, which shows the main contribution in the vertical direction, is about 3 mm/yr within 200 meters at the different sides of the FS structure (Fig. 5.25).

The KP-ex system and THSR-P systems have the universal design at the deformation region, which is near the FS fault (Fig. 5.26; Fig. 5.27). I plotted the profile along the THSR-P and KP-ex route of the universal design, which shows the velocity changing at the FS fault in the vertical direction (Fig. 5.28); however, the point here is very rare so I plotted time-series displacement. In THSR KP-1, it shows the main contribution in the vertical direction, the velocity difference is about 4 mm/yr (Fig. 5.29).

According to the regulation of pavement in “Highway Maintenance Manual (2019)” made by Freeway Bureau, MOTC, the allowable deformation of pavement can be divided

doi: 10.6342/NTU202400130

into 3 classes (Table. 5.2). The depression and upheaval mean that the deformation within each pavement, and the faulting means that the deformation between different pavements (Fig. 5.30). By considering displacements and neglecting other factors, the N7-1 will reach to H class within 25 years in the threshold of depression and upheaval, and it will reach to H class within 20 years in the threshold of faulting. The THSR KP-1 is compared to the highway limits. It will reach to H class within 25 years in the threshold of depression and upheaval, and it will reach to H class within 10 years in the threshold of faulting; the THSR KP-1 compare to the track with a gauge of 1453 mm, calculated by equation above, it will reach the allowable time within 17 years.

doi: 10.6342/NTU202400130

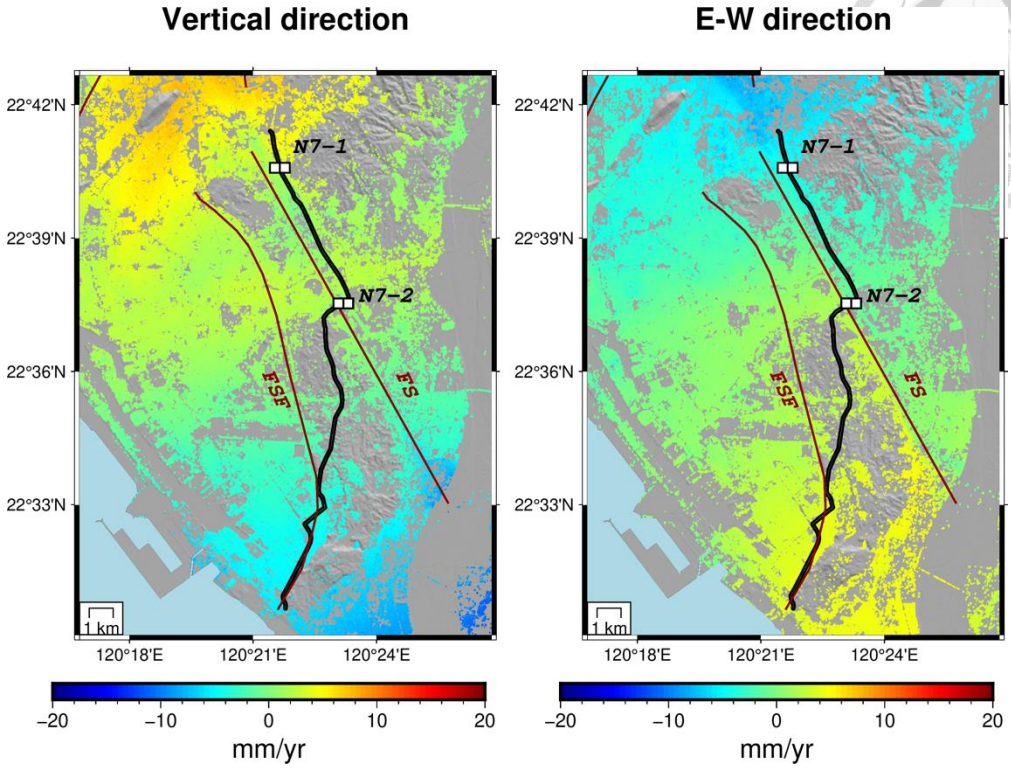

Fig. 5.21. PSInSAR result near N7 route with sharp velocity change in LOS direction.

Left is ASC track. Right is DES track. The black line is Freeway no. 7.

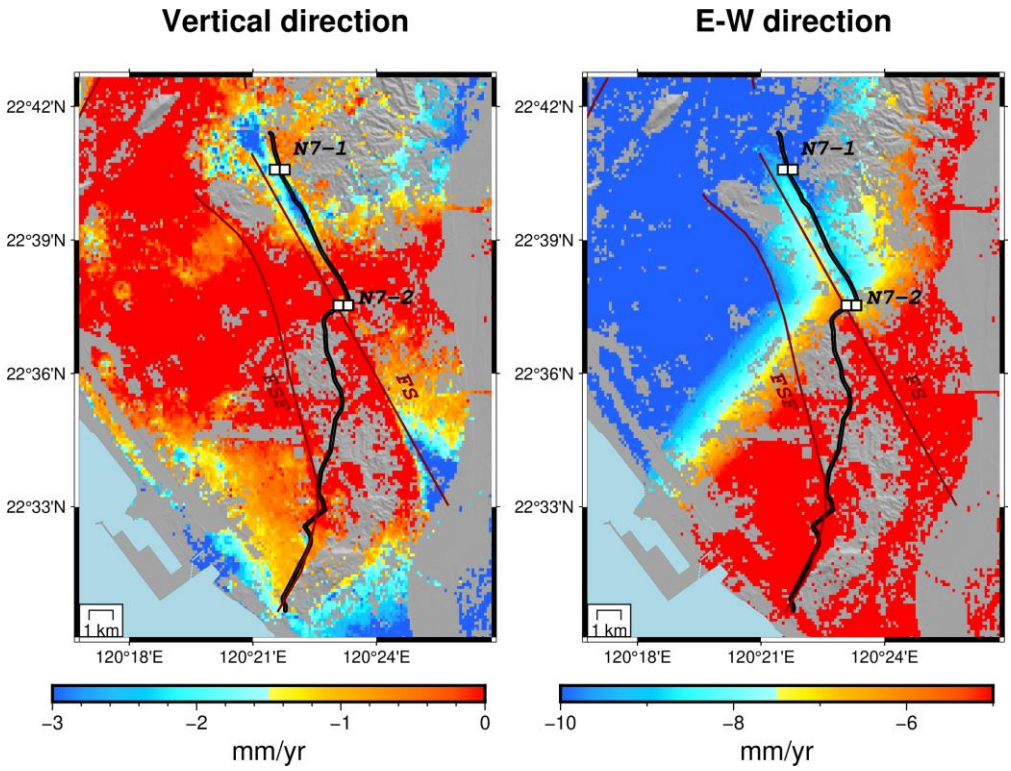

Fig. 5.22. The velocity field near N7 system in vertical and E-W directions.

doi: 10.6342/NTU202400130

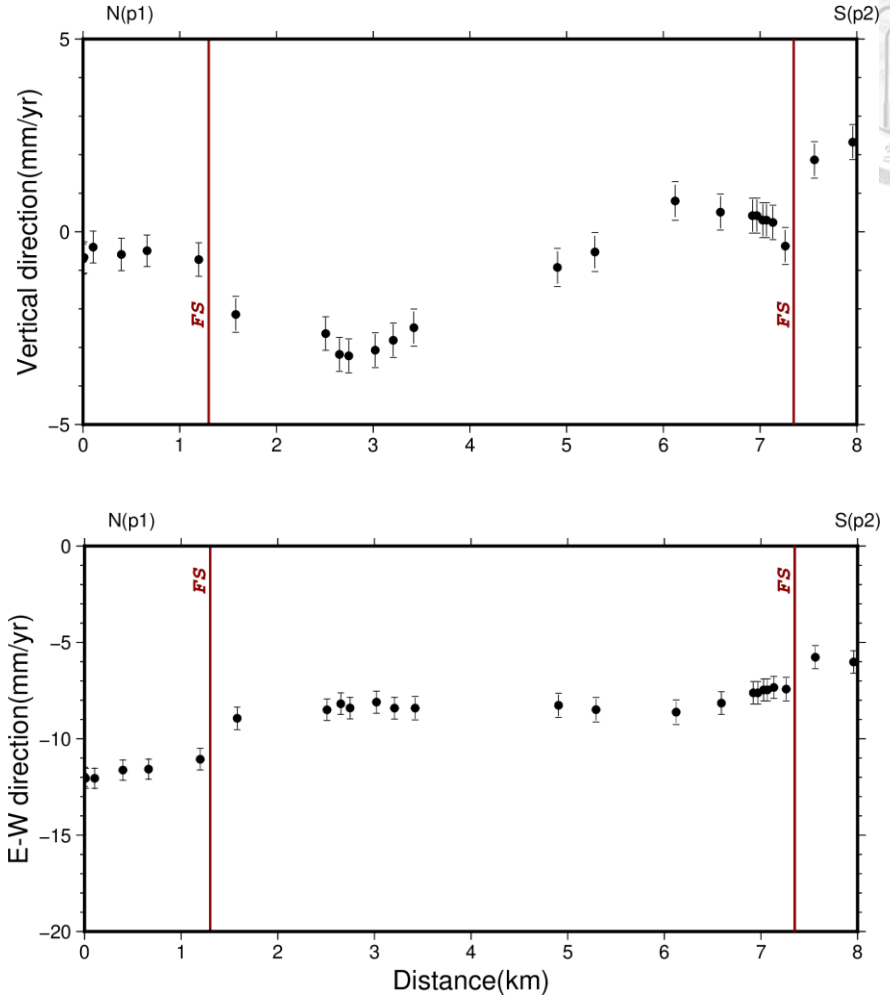

Fig. 5.23. The profile along N7 route. From 0K to 20K is from N to S direction.

doi: 10.6342/NTU202400130

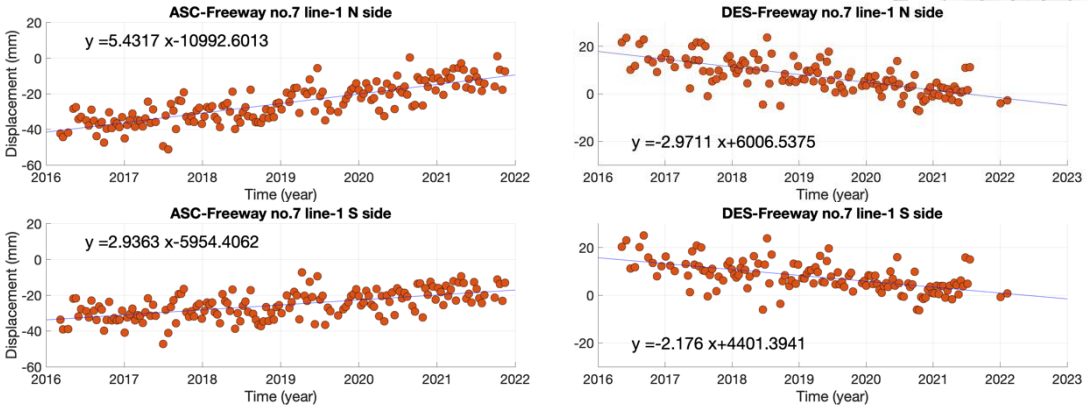

Fig. 5.24. The time-series displacement in N7-1

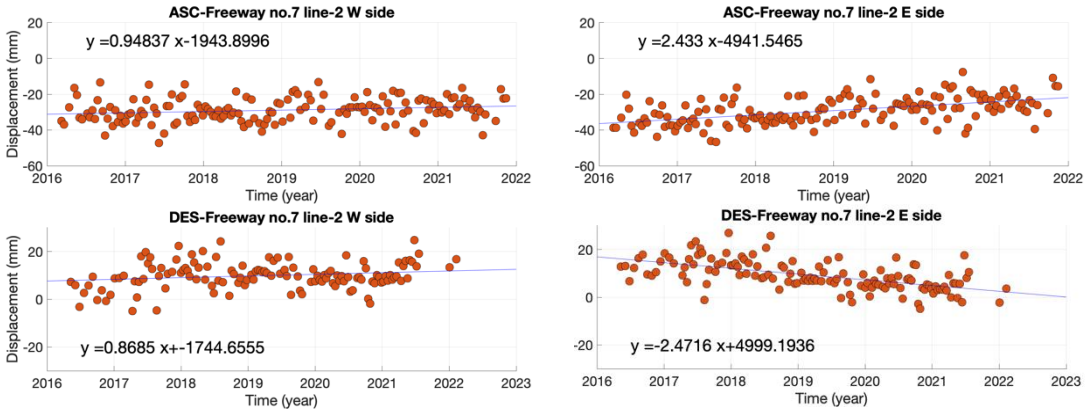

Fig. 5.25. The time-series displacement in N7-2

doi: 10.6342/NTU202400130

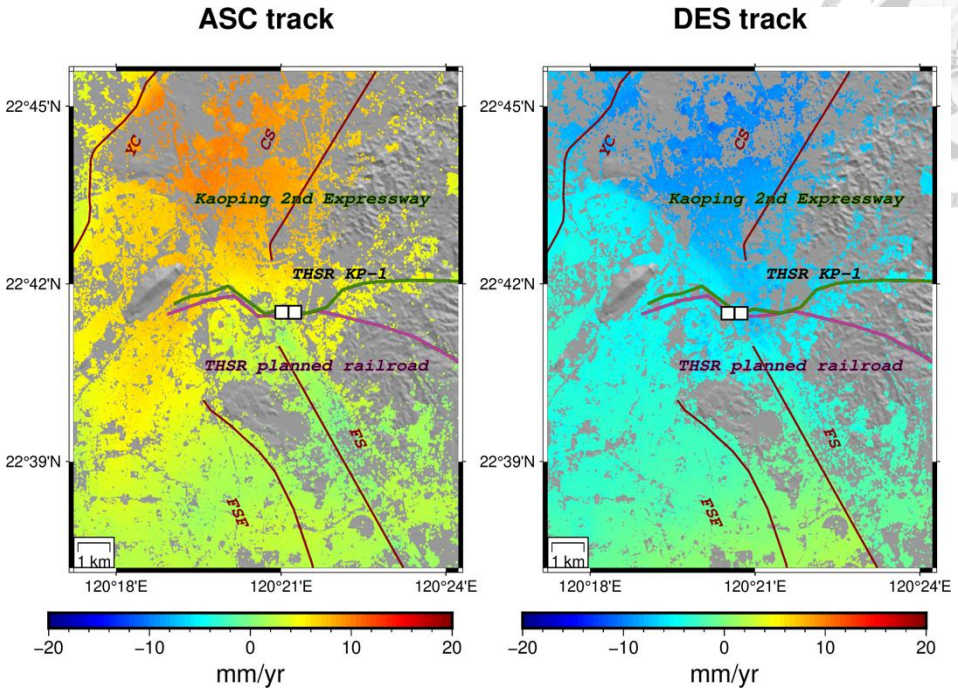

Fig. 5.26. PSInSAR result near KP-ex and THSR-P systems with sharp velocity change in LOS direction. The dark green line is KP-ex system. The dark purple line is THSR-P system. The white rectangular is the time-series location.

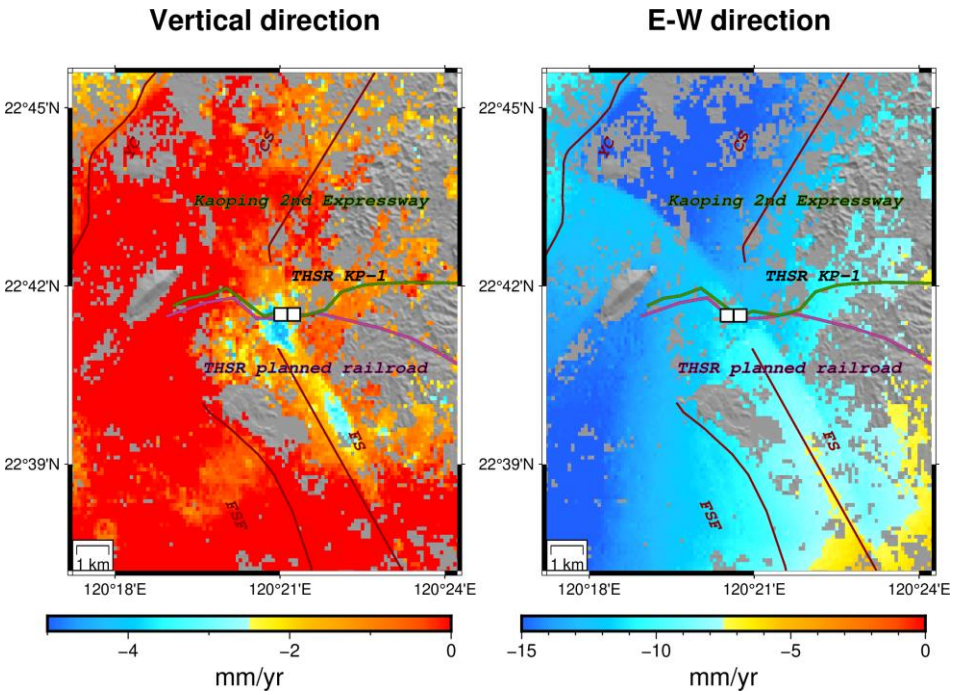

Fig. 5.27. The velocity field near KP-ex and THSR-P systems in vertical and E-W directions.

doi: 10.6342/NTU202400130

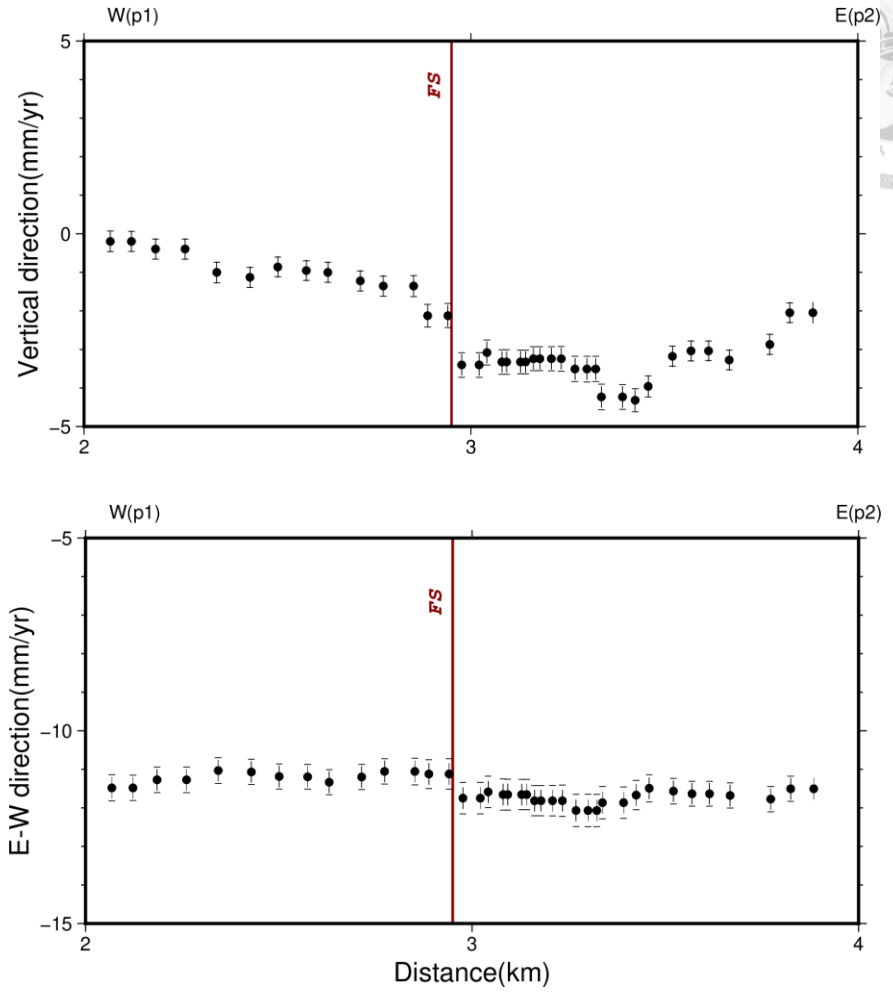

Fig. 5.28. The profile along THSR-P and KP-ex route. From 0K to 4K is from W to E direction.

doi: 10.6342/NTU202400130

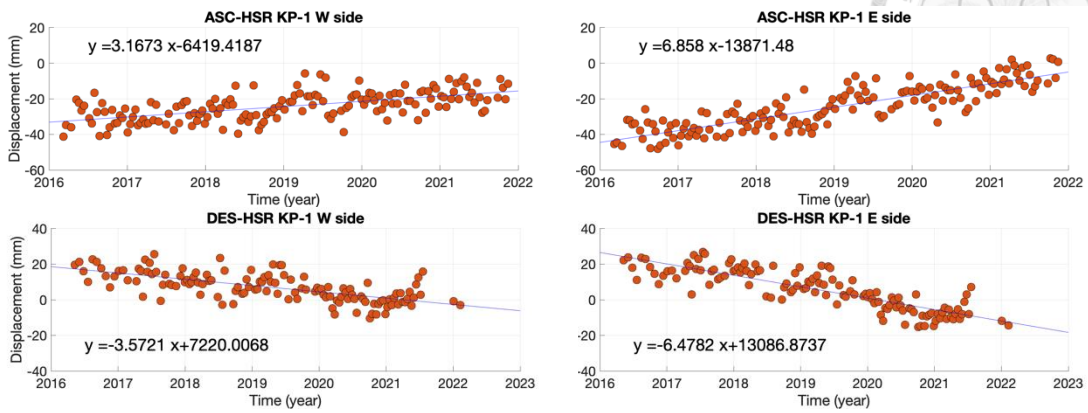

Fig. 5.29. The time-series displacement in THSR KP-1

Table 5.1: The allowable deformation of freeway pavement derived by Freeway Bureau, MOTC (2019).

	Light (L)	Medium (M)	Heavy (H)
Depression or Upheaval	13-25 mm	25-50 mm	> 50 mm
Faulting	3-10 mm	10-20 mm	> 20 mm

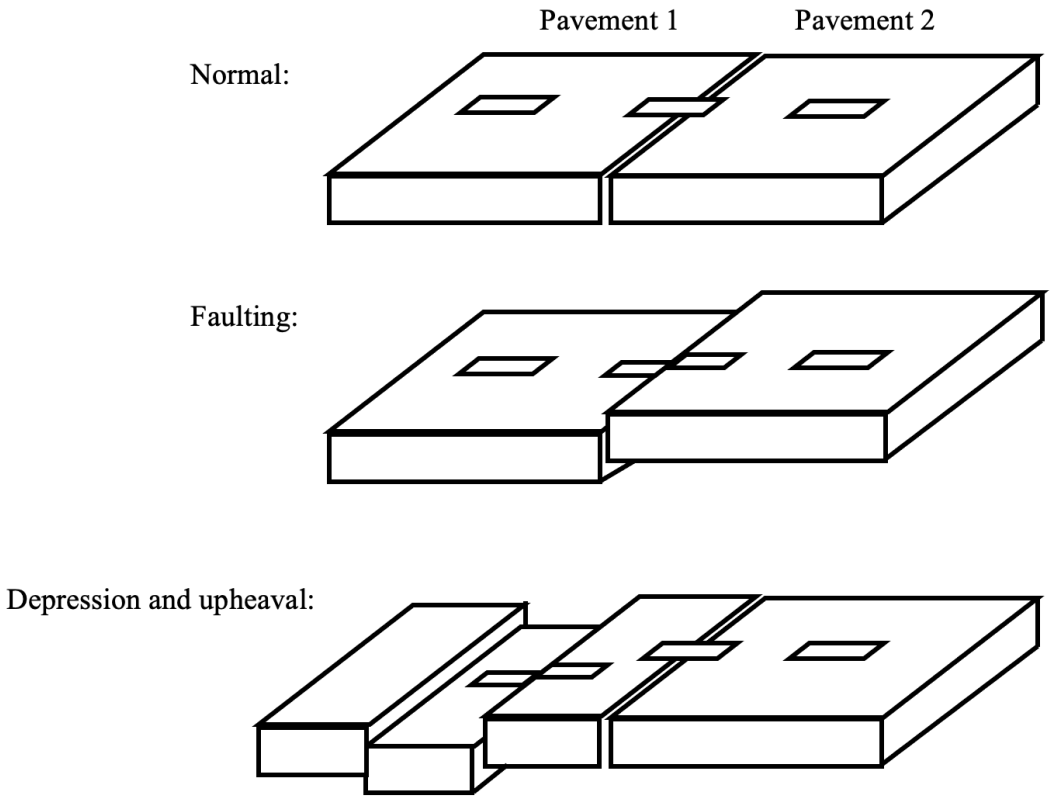

Fig. 5.30. The schematic of Faulting and Depression (Upheaval) of pavement.

doi: 10.6342/NTU202400130

5.2.2 Industrial parks

The unequal deformation not only can cause damage to transportation systems but can have a great impact on industrial parks. This section shows the industrial parks, which have unequal deformation within the park. The Yongkang Park, Tainan is cut through by the Hsinhua fault (HSH), which has a velocity difference is about 4~5 mm/yr south of the fault trace in the LOS and vertical directions (Fig. 5.31; Fig. 5.32). The Dade Park, Kaohsiung is cut through by the HKS fault, which has unequal deformation is about 1~3 mm/yr (Fig. 5.33; Fig. 5.34). The velocity difference in Yanchao and Ciaotou Park, Kaohsiung which is cut through by the CKL fault is about 3~7 mm/yr within the park (Fig. 5.35; Fig. 5.36).

The “Regulations for the Delineation, Amendment and Revocation of Geologically Sensitive Area Status” from CGS illustrates the sensitive area of an active fault. This area is based on a fault deformation zone based on historical earthquake data and geological drilling data. There are only 3 active faults that have sensitive areas in our study area, namely the HSH, HSK, and CS faults. The sensitive area of the HSH fault is 150 meters on both sides of the fault trace. The sensitive areas of the HKS fault and CS fault are 200 meters and 100 meters in the hanging wall and foot wall, respectively. Along the fault traces of the CGS, only the Ciaotou Park area is intersected by a fault, while the other parks are not within any sensitive zone. However, the parks have unequal deformation

doi: 10.6342/NTU202400130

within parks near the fault traces, and even some parks are intersected by TEM fault traces based on the PS observations. In addition, the areas near some faults are also active, such as the Houchiali fault and the Chekualin fault. Although we cannot confirm the deformation here is caused by fault activity, it is still necessary to pay attention to such deformation near the active faults. Thus, it is recommended to establish active fault sensitive areas in the future.

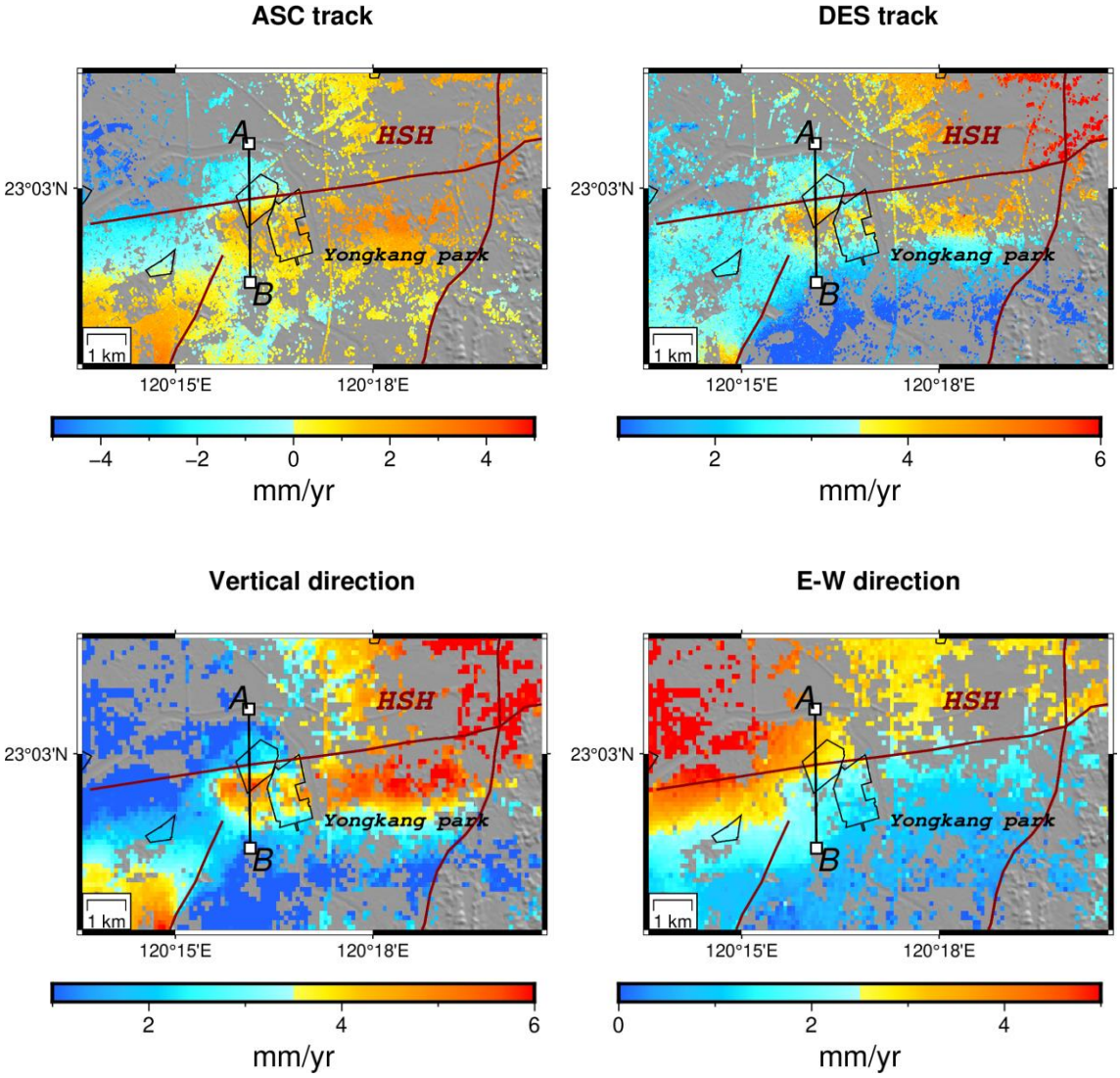

Fig. 5.31. The velocity field near the Yongkang park in LOS and decomposition directions.

doi: 10.6342/NTU202400130

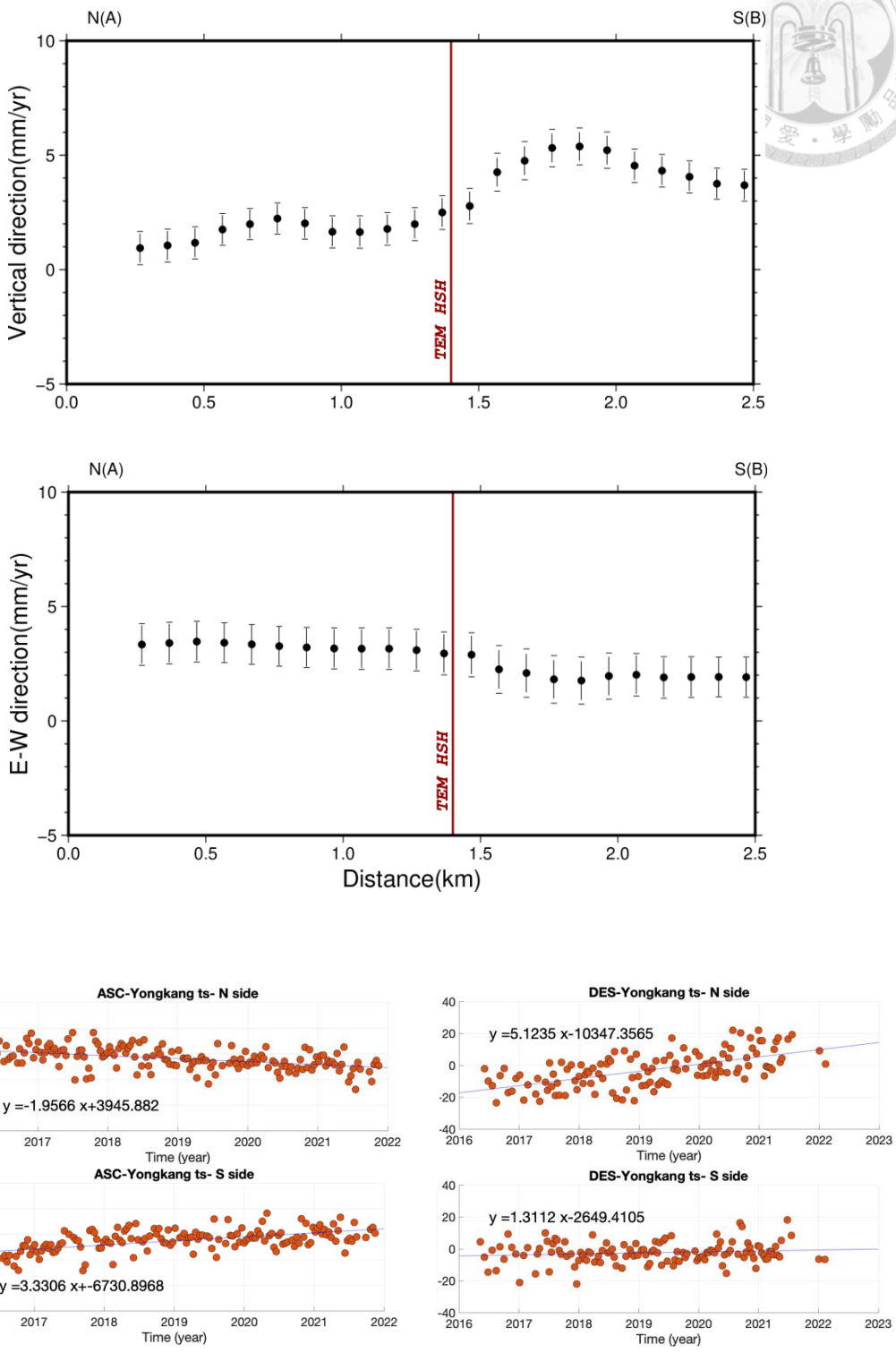

Fig. 5.32. The velocity along AB profile line and the time-series displacement at Yongkang Park in decomposition and LOS directions, respectively.

doi: 10.6342/NTU202400130

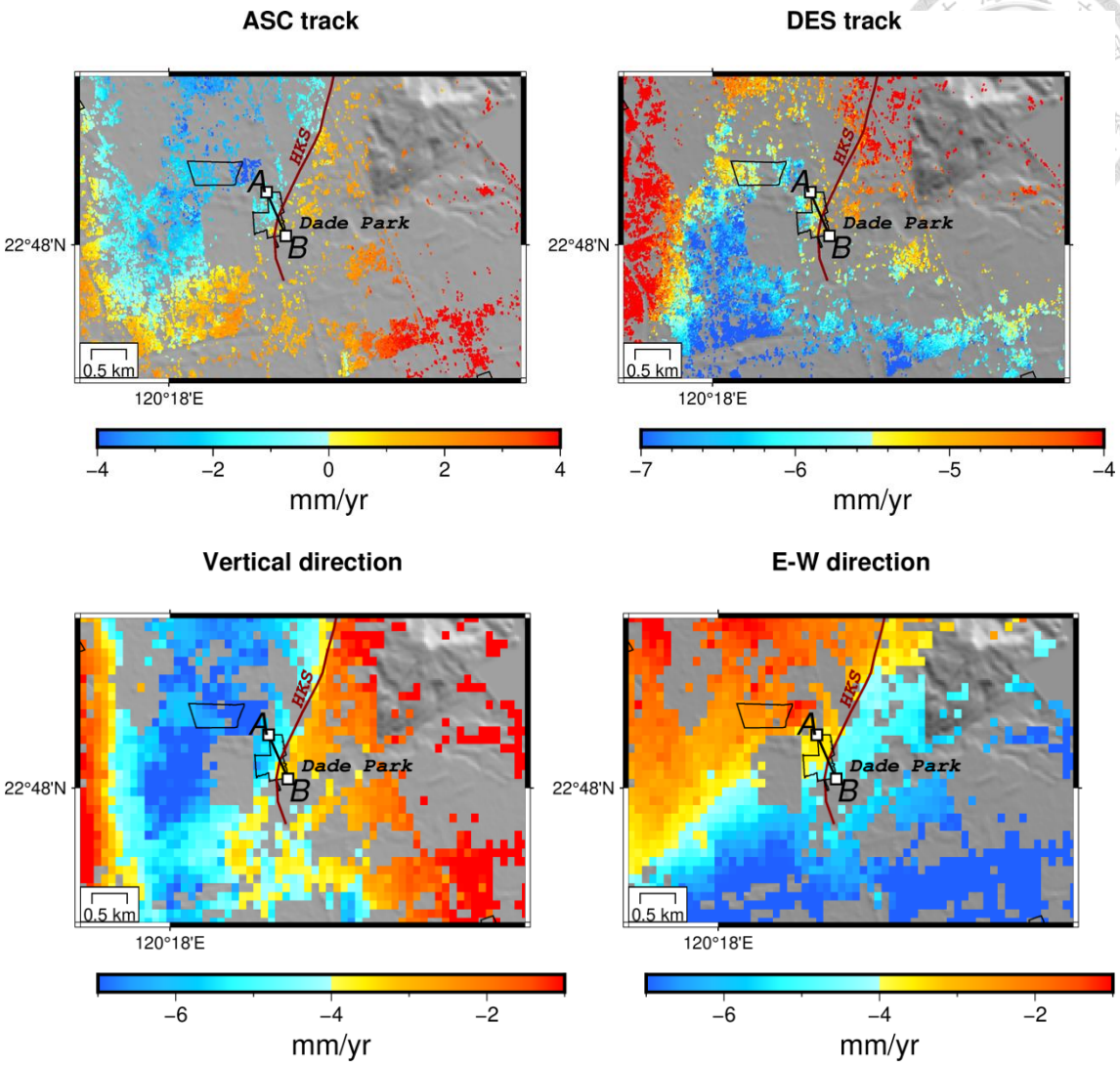

Fig. 5.33. The velocity field near the Dade Park in LOS and decomposition directions.

doi: 10.6342/NTU202400130

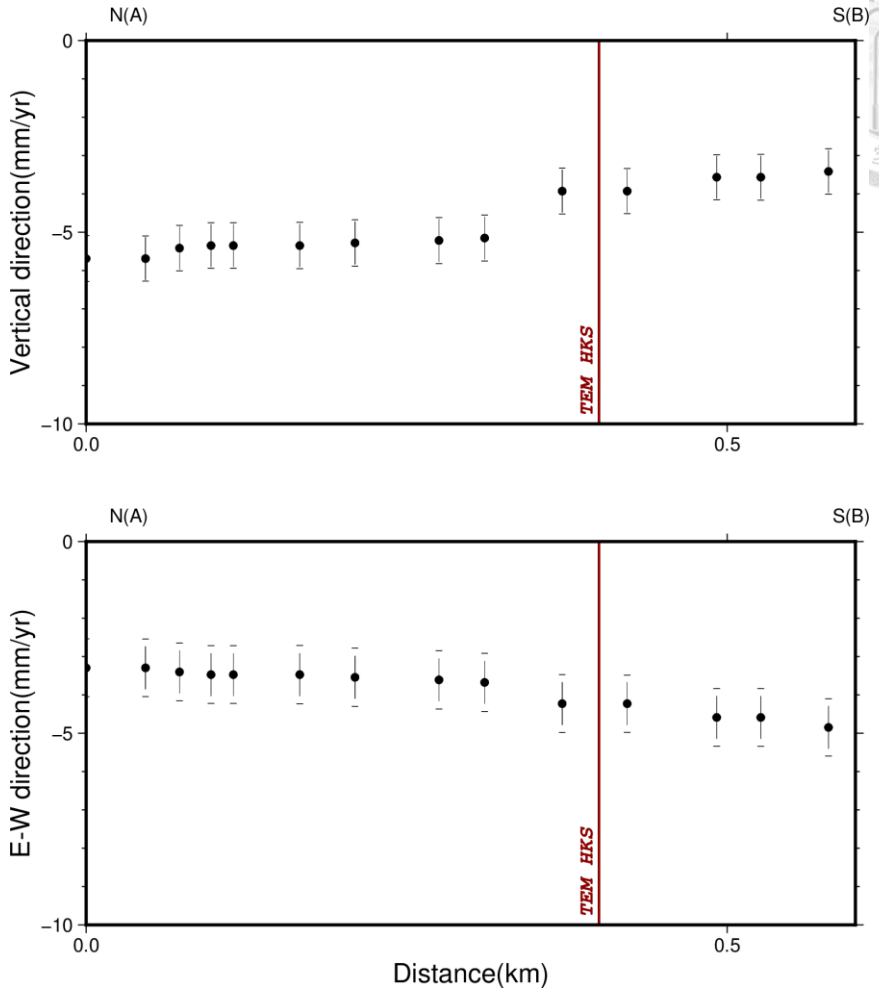

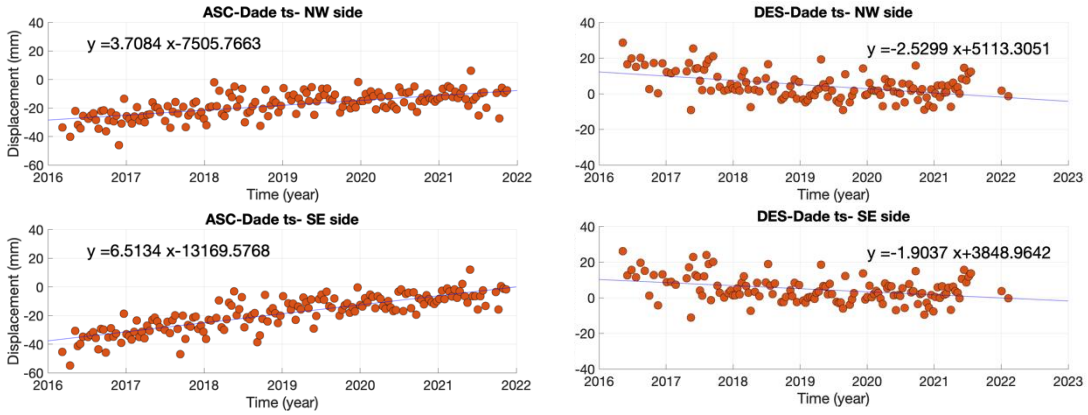

Fig. 5.34. The velocity along AB profile line and the time-series displacement at Dade Park in LOS and decomposition directions, respectively.

doi: 10.6342/NTU202400130

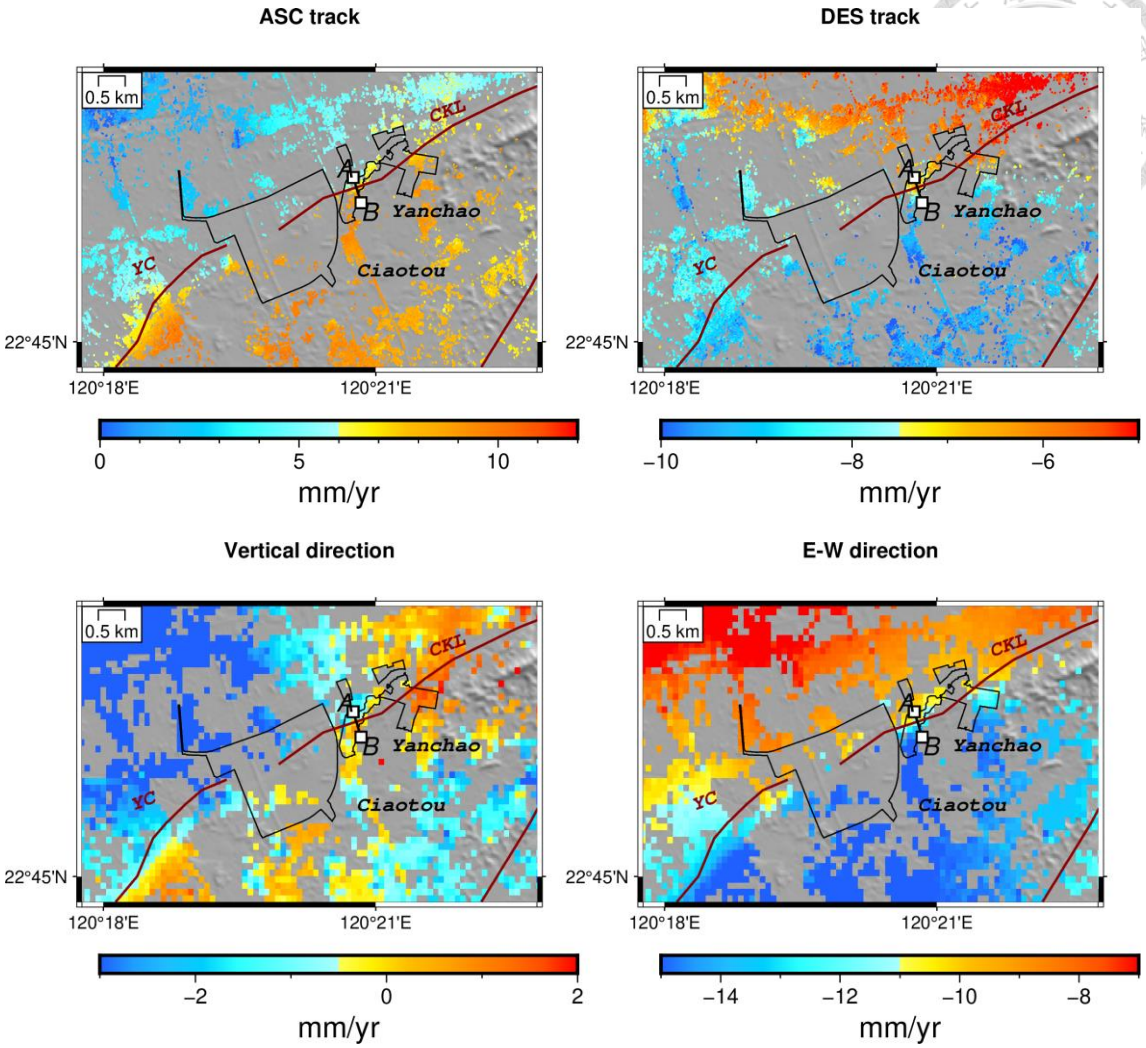

Fig. 5.35. The velocity field near the Yanchao and Ciaotou park in LOS and decomposition directions.

doi: 10.6342/NTU202400130

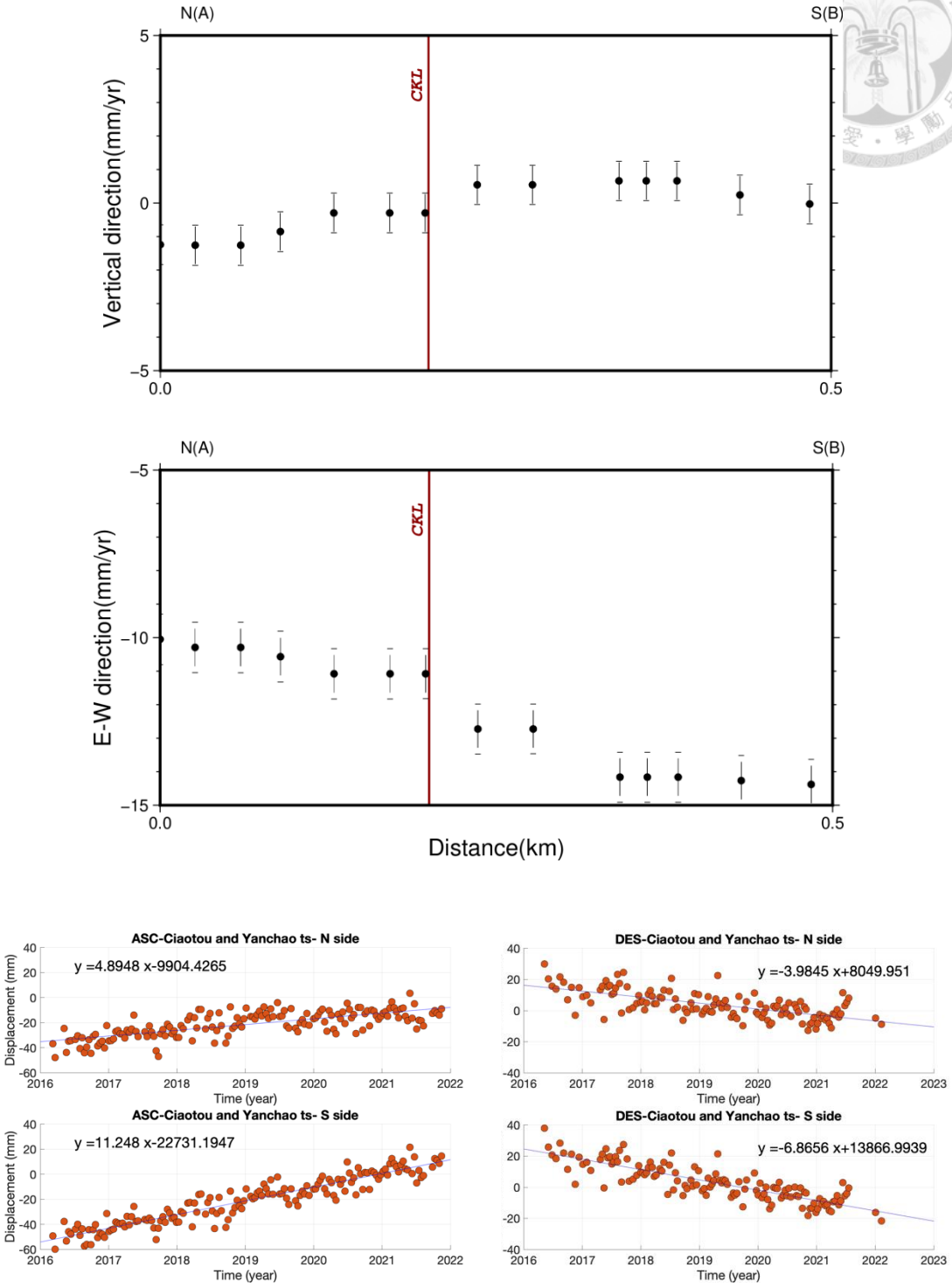

Fig. 5.36. The velocity along AB profile line and the time-series displacement at Ciaotou and Yanchao Park in LOS and decomposition directions.

doi: 10.6342/NTU202400130

Chapter 6 Conclusions

This study uses StaMPS/MTI algorithm to process PSInSAR from 2016 (after the Meinong earthquake) to 2022. I generated velocity fields near active faults, transportation systems, and industrial parks in SW Taiwan. The conclusions are as following:

There are many active faults across urban areas in our study area. The PSI result shows reliable displacements by removing spatial-temporal error because of the stable signals reflected from human objects. Thus, we can get the velocity and time-series displacements across the active faults. Although the result is during the interseismic period, we can still see the displacements so there should be surface fault creep along some active structures. The slip rates are shown below: the HCL fault has 3~6 mm/yr, the HKS fault has 1~2 mm/yr, the CKL fault has 4~8 mm/yr, and the YC fault has 1~3 mm/yr. According to the observations, THSR will reach to limit within 7 years, the TR railroad will reach to limit within 10 years, and the Freeway system will reach to H class within 10 years. Although the Freeway systems mentioned above and industrial parks are not affected immediately, the accumulation of deformation would have an impact on them in the future. Through this study, we know the present-day situation of surface deformation on active faults and critical infrastructures of urban areas in SW Taiwan. There is still need for more geodetic observations to monitor to provide a better vision of future hazards.

doi: 10.6342/NTU202400130

Reference

1067 公厘軌距軌道橋隧檢查養護規範（2003）。交通部，民國 92 年。

何春蓀 (1975) 。臺灣地質概論。經濟部地質調查所，共 118 頁。

李俊賢(2020) 。估計台灣高鐵里程 TK331 段高架橋結構變位及評估其影響: 使用 GPS, 水準, 角邊測量技術. 國立成功大學測量及空間資訊學系博士論文，共 99 頁。

林啟文、張徽正、陳勉銘、盧詩丁、石同生、黃文正（2000）。活動斷層概論，五十萬分之一灣活動斷層分布圖說明，第二版。經濟部中央地質調查所特刊，第 13 號，共 122 頁。

林啟文, 盧詩丁, 石同生, 劉彥求, 林偉雄, 林燕慧（2007）。臺灣西南部的活動斷層：二萬五千分之一活動斷層條帶圖說明書。經濟部中央地質調查所特刊，第 17 號。

林啟文、陳文山、劉彥求、陳柏村（2009）。臺灣東部與南部的活動斷層：二萬五千分之一活動斷層條帶圖說明書。經濟部中央地質調查所特刊，第 23 號。

胡植慶、劉啟清、饒瑞鈞、李元希、鄭錦桐、張午龍、陳卉瑄、景國恩、唐昭榮（2012）。「斷層活動性觀測研究第二階段斷層監測與潛勢分析研究(4/4)」(第四年度)，計畫編號：101-5226904000-01-01，經濟部中央地質調查所 101 年度委託專業服務計畫執行期末報告書，共 422 頁。

孫習之、施垚鑫 (1960) 。 高雄縣大崗山至鳳山區間地質調查報告，中油內部報告

耿文溥 (1967)。臺灣南部甲仙及旗山間之地質。臺灣省地質調查所彙刊，第 19 號，1-13 頁。

鳥居敬造（1932）。台南州新化油田調查報告。臺灣總督府殖產局，609 號，共 29 頁。

張中白、王志添、王皓正、陳錕山（2004）。應用雷達差分干涉法監測都會型地表變形：以中壢工業區為例。航測及遙測學刊，第九卷，第三期，第 9-14 頁。

陳文山、黃能偉、游能悌、周飛宏、顏一勤、宋時驊、楊志成、楊小青 (2005)。地震地質調查及活動斷層資料庫建置計畫－槽溝開挖與古地震研究計畫（4/5）－旗山與龍船斷層條帶地質圖說明書。經濟部中央地質調查所報告第 94-08-2 號，共 48 頁。

陳柏村 (2005)。旗山斷層南段變形特性研究。國立成功大學地球科學研究所碩士論文，共 125 頁。

陳柏村、林啟文、江婉綺、劉彥求、林慶偉 (2009)。臺灣南部旗山斷層的構造特

doi: 10.6342/NTU202400130

性研究。經濟部中央地質調查所彙刊，第 22 號，63-98 頁。

陳文山、松多信尚、石瑞銓、楊志成、游能悌、朱耀國、陳志壕、林啟文、劉桓吉、盧詩丁、劉彥求、林燕慧、陳柏村（2010）。臺灣西部平原區隱伏在全新世沉積層下的新期構造－以小崗山斷層為例。經濟部中央地質調查所特刊，第 24 號，第 75-92 頁。

陳文山、黃能偉、楊志成（2011）。臺灣西南部更新世沉積層序特性與前陸盆地演化。經濟部中央地質調查所特刊，第 25 號，1-38 頁。

陳文山、游能悌、楊小青（2012）。重要活動斷層帶構造特性調查研究計畫-斷層活動特性分析與評估 (2/4) ，經濟部中央地質調查所報告，計畫編號：101-5226904000-05-03，共 130 頁。

景國恩、胡植慶、陳宏宇、張午龍、鄭凱謙、莊昀叡（2019）。斷層活動性觀測研究第四階段-地表變形觀測資料處理分析與斷層模型反演評估（3/4）。經濟部中央地質調查所報告，計畫編號：108-5226904000-05-01，共 269 頁。

趙荃敏（2016）。利用大地測量及 PSInSAR 技術探討鳳山斷層之運動特性。國立成功大學地球科學系碩士論文，共 89 頁。

劉彥求、林啟文（2019）。臺灣南部車瓜林斷層的構造特性研究。經濟部中央地質調查所特刊，第 34 號，第 53-82 頁。

鄭宏祺（2000）。台灣西南部至屏東地區地質構造之研究，國立中央大學應用地質研究所碩士論文，共 92 頁。

謝嘉聲、史天元 (2006)。以雷達干涉技術偵測地表變形之研究 (Doctoral dissertation).

饒瑞鈞、余致義、洪日豪、胡植慶、李建成、詹瑜璋、許麗文（2006）。活動斷層監測系統計畫（5/5）。經濟部中央地質調查所報告，計畫編號：計畫編號:5226902000-02-95-03，共 256 頁。

重要活動斷層地區地表變形觀測與斷層潛勢評估（2022）。國立成功大學。經濟部中央地質調查所 111 年度委託專業服務期末報告書，計畫編號：B11130。

A. Moreira, P. Prats-Iraola, M. Younis, G. Krieger, I. Hajnsek and K. P. Papathanassiou (2013). "A tutorial on synthetic aperture radar," in IEEE Geoscience and Remote Sensing Magazine, vol. 1, no. 1, pp. 6-43, March 2013, doi: 10.1109/MGRS.2013.2248301.

Bekaert, D.P.S., Hooper, A.J., and Wright, T.J. (2015a). A spatially-variable power-law tropospheric correction technique for InSAR data, JGR, doi:10.1029/2014JB011558

doi: 10.6342/NTU202400130

Bekaert, D.P.S., Walters, R.J., Wright, T.J., Hooper, A.J., and Parker, D.J. (2015c). Statistical comparison of InSAR tropospheric correction techniques, Remote Sensing of Environment, doi: 10.1016/j.rse.2015.08.035

Bekaert, D. P. S., Hamlington, B. D., Buzzanga, B., and Jones, C. E. (2017). Spaceborne synthetic aperture radar survey of subsidence in Hampton Roads, Virginia (USA). Scientific reports, 7(1), 14752.

Chen, Y. G. and T. K. Liu (2000). Holocene uplift and subsidence along an active tectonic margin southwestern Taiwan. Quat. Sci. Rev., 19, 923-930, doi: 10.1016/S0277-3791(99)00076-1.

Chen, W. S. (2010). Research of long-term slip rates and recurrence intervals of faults (overall report), earthquake geology and potential deformation analysis projects. Cent. Geol. Surv. Rep. 99-09, Taipei, 141 pp. (in Chinese)

Chen, W. S., N. T. Yu, and H. C. Yang (2012). Active characteristics analysis and assessment of faults (2/4), structural characteristics investigation of important active faults research projects. Cent. Geol. Surv. Rep. 101-9, Taipei, 130 pp. (in Chinese)

Chen, S. C., Hsu, S. K., Wang, Y., Chung, S. H., Chen, P. C., Tsai, C. H., and Lee, Y. W. (2014). Distribution and characters of the mud diapirs and mud volcanoes off southwest Taiwan. Journal of Asian Earth Sciences, 92, 201-214.

Chen, L., Wang, H. Y., Wang, T. S., and Kou, C. H. (2019). Remote sensing for detecting changes of land use in Taipei City, Taiwan. Journal of the Indian Society of Remote Sensing, 47, 1847-1856.

Chen, T. H. K., Prishchepov, A. V., Fensholt, R., and Sabel, C. E. (2019). Detecting and monitoring long-term landslides in urbanized areas with nighttime light data and multi-seasonal Landsat imagery across Taiwan from 1998 to 2017. Remote Sensing of Environment, 225, 317-327.

Chen, K. H., Chuang, R. Y., and Ching, K. E. (2020). Realization approach of non-linear postseismic deformation model for Taiwan semi-kinematic reference frame. Earth, Planets and Space, 72, 1-13.

Chi W.R. (1981). Nannofossils, Exploration and Development Research Center, p. 407 (in Chinese).

Ching, K.-E., R.-J. Rau, and Y. Zeng (2007a), Coseismic source model of the 2003 Mw

doi: 10.6342/NTU202400130

6.8 Chengkung earthquake, Taiwan, determined from GNSS measurements, J. Geophys. Res., 112, B06422, doi:10.1029/2006JB004439.

Ching, K. E., Rau, R. J., Lee, J. C., & Hu, J. C. (2007). Contemporary deformation of tectonic escape in SW Taiwan from GNSS observations, 1995–2005. Earth and Planetary Science Letters, 262(3-4), 601-619.

Ching, K. E., Hsieh, M. L., Johnson, K. M., Chen, K. H., Rau, R. J., and Yang, M. (2011). Modern vertical deformation rates and mountain building in Taiwan from precise leveling and continuous GNSS observations, 2000–2008. Journal of Geophysical Research: Solid Earth, 116(B8).

Ching, K.-E., Rau, R.-J., Johnson, K.M., Lee, J.-C., and Hu, J.-C. (2011). Present-day kinematics of active mountain building in Taiwan from GNSS observations during 1995–2005.J. Geophys. Res. 116, B09405.

Ching, K. E., Gourley, J. R., Lee, Y. H., Hsu, S. C., Chen, K. H., and Chen, C. L. (2016). Rapid deformation rates due to development of diapiric anticline in southwestern Taiwan from geodetic observations. Tectonophysics, 692, 241-251.

Ding, C., Lee, C., & Ho, S. Characteristics of the Chekualin Fault in the Yanchao area, Kaohsiung City.

Ezeoke, M., Tong, K., and Shi, S. (2014). Modeling synthetic aperture radar signature of agbabu oil sand for petroleum exploration. *WIT Transactions on Ecology and the Environment*, *190*, 1283-1295.

Ferretti, A., C. Prati, and F. Rocca (2000). Nonlinear subsidence rate estimation using permanent scatterers in differential SAR interferometry, Geoscience and Remote Sensing, IEEE Trans. Geosci. Remote Sens, 38(5), 2202-2212.

Ferretti, A., C. Prati, and F. Rocca (2001). Permanent scatterers in SAR interferometry, IEEE Trans. Geosci. Remote Sens., 39(1), 8 –20.

Fuhrmann, T., and Garthwaite, M. C. (2019). Resolving three-dimensional surface motion with InSAR: Constraints from multi-geometry data fusion. Remote Sensing, 11(3), 241.

Funning, G. J., Bürgmann, R., Ferretti, A., Novali, F., and Fumagalli, A. (2007). Creep on the Rodgers Creek fault, northern San Francisco Bay area from a 10 years PS-InSAR dataset. Geophysical Research Letters, 34(19).

Global Modeling and Assimilation Office (GMAO) (2015). MERRA-2 inst6_3d_ana_Np: 3d,6-Hourly, Instantaneous, Pressure-Level, Analysis, Analyzed Meteorological

doi: 10.6342/NTU202400130

Fields V5.12.4, Greenbelt, MD, USA, Goddard Earth Sciences Data and Information Services Center (GES DISC), Accessed: [2022.7.20], 10.5067/A7S6XP56VZWS

Ge, L., Ng, A. H. M., Du, Z., Chen, H. Y., and Li, X. (2017). Integrated space geodesy for mapping land deformation over Choushui River Fluvial Plain, Taiwan. International Journal of Remote Sensing, 38(22), 6319-6345.

Hanssen, R.F. (2001). Radar Interferometry: Data Interpretation and Error Analysis; Springer Science & Business Media: New York, NY, USA, 2001; Volume 2.

Helz, R. L. (2005). Monitoring ground deformation from space. US Department of the Interior, US Geological Survey.

Hooper, A., P. Segall, K. Johnson, and J. Rubinstein (2002). Reconciling seismic and geodetic models of the 1989 Kilauea south flank earthquake, Geophysical Research Letters, 29(22)Artn 2062, Doi 10.1029/2002gl016156.

Hooper, A., H. Zebker, P. Segall, and B. Kampes (2004), A new method for measuring deformation on volcanoes and other natural terrains using InSAR persistent scatterers, Geophysical Research Letters, 31(23) Artn L23611, Doi 10.1029/2004gl021737.

Hooper, A., and H. A. Zebker (2007). Phase unwrapping in three dimensions with application to InSAR time series, J Opt Soc Am A Opt Image Sci Vis, 24(9), 2737-2747

Hooper, A. (2008). A multi-temporal InSAR method incorporating both persistent scatterer and small baseline approaches, Geophysical Research Letters, 35(16)10.1029/2008gl034654.

Hsieh, C. S., Shih, T. Y., Hu, J. C., Tung, H., Huang, M. H., & Angelier, J. (2011). Using differential SAR interferometry to map land subsidence: a case study in the Pingtung Plain of SW Taiwan. Natural hazards, 58, 1311-1332.

Huang, S. T., Yang, K. M., Hung, J. H., Wu, J. C., Ting, H. H., Mei, W. W., and Lee, M. (2004). Deformation front development at the northeast margin of the Tainan basin, Tainan–Kaohsiung area, Taiwan. Marine Geophysical Researches, 25(1), 139-156.

Huang, M. H. (2006). The case studies of the crustal deformation in Taiwan based on SAR interferometry. National Taiwan University PhD Thesis.

Huang, M. H., Bürgmann, R., and Hu, J. C. (2016). Fifteen years of surface deformation in Western Taiwan: Insight from SAR interferometry. Tectonophysics, 692, 252-

doi: 10.6342/NTU202400130

264.

Huang, M. H., Tung, H., Fielding, E. J., Huang, H. H., Liang, C., Huang, C., & Hu, J. C. (2016). Multiple fault slip triggered above the 2016 Mw 6.4 MeiNong earthquake in Taiwan. Geophysical Research Letters, 43(14), 7459-7467.

Hwang, C., Hung, W. C., and Liu, C. H. (2008). Results of geodetic and geotechnical monitoring of subsidence for Taiwan High Speed Rail operation. Natural Hazards, 47(1), 1-16.

Jian, L., Tseng, K. H., Tai, Y. H., and Lin, Y. C. (2019). Linking Land Subsidence and Land Use in Western Taiwan by Sentinel-1 PSInSAR Timeseries and A Network of GPS Continuous Stations. In AGU Fall Meeting Abstracts (Vol. 2019, pp. G13B-0535).

Lanari, R., Casu, F., Manzo, M., and Lundgren, P. (2007). Application of the SBAS-DInSAR technique to fault creep: A case study of the Hayward fault, California. Remote Sensing of Environment, 109(1), 20-28.

Lee, J. C., Angelier, J., Chu, H. T., Hu, J. C., Jeng, F. S., and Rau, R. J. (2003). Active fault creep variations at Chihshang, Taiwan, revealed by creep meter monitoring, 1998–2001. Journal of Geophysical Research: Solid Earth, 108(B11).

Lin, K.-C., Hu, J.-C., Ching, K.-E., Angelier, J., Rau, R.-J., Yu, S.-B., Tsai, C.-H., Shin, T.-C., and Huang, M.-H. (2010). GNSS crustal deformation, strain rate, and seismic activity after the 1999 Chi–Chi earthquake in Taiwan. J. Geophys. Res. 115, B07404.

Lillesand, T.M. and Kiefer, R.W. (1994). Remote Sensing and Image Interpretation. 3rd Edition, John Wiley and Sons, Inc., Hoboken, 750.

Lillesand, T., Kiefer, R. W., and Chipman, J. (2015). Remote sensing and image interpretation. John Wiley & Sons.

Lo, Y. T., Ching, K. E., Yen, H. Y., and Chen, S. C. (2023). Bouguer gravity anomalies and the three-dimensional density structure of a thick mudstone area: A case study of southwestern Taiwan. Tectonophysics, 848, 229730.

Miller, M. M., and Shirzaei, M. (2015). Spatiotemporal characterization of land subsidence and uplift in Phoenix using InSAR time series and wavelet transforms. Journal of Geophysical Research: Solid Earth, 120(8), 5822-5842.

Massonnet, D., Rossi, M., Carmona, C., Adragna, F., Peltzer, G., Feigl, K., & Rabaute, T. (1993). The displacement field of the Landers earthquake mapped by radar

doi: 10.6342/NTU202400130

interferometry. nature, 364(6433), 138-142.

Massonnet, D., and Feigl, K. L. (1998). Radar interferometry and its application to changes in the Earth's surface. *Reviews of geophysics*, *36*(4), 441-500.

Moreira, A., Prats-Iraola, P., Younis, M., Krieger, G., Hajnsek, I., and Papathanassiou, K. P. (2013). A tutorial on synthetic aperture radar. IEEE Geoscience and remote sensing magazine, 1(1), 6-43.

Nam, B. X., Van Anh, T., Bui, L. K., Long, N. Q., Ha, T. L. T., and Goyal, R. (2021). Mining-Induced Land Subsidence Detection by Persistent Scatterer InSAR and Sentinel-1: Application to Phugiao Quarries, Vietnam. In Proceedings of the International Conference on Innovations for Sustainable and Responsible Mining (pp. 18-38). Springer, Cham.

Osmanoğlu, B., Sunar, F., Wdowinski, S., and Cabral-Cano, E. (2016). Time series analysis of InSAR data: Methods and trends. ISPRS Journal of Photogrammetry and Remote Sensing, 115, 90-102.

Pepe, A., & Calò, F. (2017). A review of interferometric synthetic aperture RADAR (InSAR) multi-track approaches for the retrieval of Earth's surface displacements. Applied Sciences, 7(12), 1264.

Prati, C. L. A. U. D. I. O., Ferretti, A., & Perissin, D. (2010). Recent advances on surface ground deformation measurement by means of repeated space-borne SAR observations. Journal of Geodynamics, 49(3-4), 161-170.

Scott, C. (2021). The Central San Andreas creeps along without a major earthquake, Temblor, http://doi.org/10.32858/temblor.152

Segall, P., and Davis, J. L. (1997). GNSS applications for geodynamics and earthquake studies. Annual Review of Earth and Planetary Sciences, 25(1), 301-336.

Shyu, J.B.H., Sieh, K., Chen, Y.-G., and Liu, C.-S. (2005). Neotectonic architecture of Taiwan and its implications for future large earthquakes. J. Geophys. Res. 110, B08402.

Shyu, J. B. H., Y. R. Chuang, Y. L. Chen, Y. R. Lee, and C. T. Cheng (2016): A new on-land seismogenic structure source database from the Taiwan Earthquake Model (TEM) project for seismic hazard analysis of Taiwan. Terr. Atmos. Ocean. Sci., 27, 311-323, doi: 10.3319/TAO.2015.11.27.02(TEM)

Shyu, J. B. H., Y.-H. Yin, C.-H. Chen, Y.-R. Chuang, and S.-C. Liu (2020). Updates to the on-land seismogenic structure source database by the Taiwan Earthquake Model

doi: 10.6342/NTU202400130

(TEM) project for seismic hazard analysis of Taiwan. Terr. Atmos. Ocean. Sci., 31, 469-478, doi: 10.3319/TAO.2020.06.08.01

Suppe, J. (1984). Kinematics of arc–continent collision, flipping of subduction and back-arc spreading near Taiwan. Mem. Geol. Soc. China 6, 21–33.

Stramondo, S., Trasatti, E., Albano, M., Moro, M., Chini, M., Bignami, C., ... & Saroli, M. (2016). Uncovering deformation processes from surface displacements. Journal of Geodynamics, 102, 58-82.

Tanaka, K., Asano, K., Ishihara, T., Watanabe, M., Komatsubara, D., Kasirajima, N., ... & Suzuki, K. (2020). Mud volcanoes and human geoscience. Human Geoscience, 167-188.

Tsukahara, K. and Takada, Y. (2018). Aseismic fold growth in southwestern Taiwan detected by InSAR and GNSS. Earth Planets Space 70, 52. https://doi.org/10.1186/s40623-018-0816-6

Tymofyeyeva, E., Fialko, Y., Jiang, J., Xu, X., Sandwell, D., Bilham, R., and Moafipoor, S. (2019). Slow slip event on the Southern San Andreas fault triggered by the 2017 M w 8.2 Chiapas (Mexico) earthquake. Journal of Geophysical Research: Solid Earth, 124(9), 9956-9975.

Wang, C. T., Chen, K. S., Hu, J. C., Chang, W. Y., and Boerner, W. M. (2011). Mapping land uplift and subsidence in the industrial parks in northern Taiwan by radar interferometry. International journal of remote sensing, 32(21), 6527-6538.

Wu J.C., Tsai C.T., Mei W.W., Wang M.H., Yang K.M., Huang S.T., Lee M., and Chi W.R. (2002). Re-approach of Gutingkeng Sequence in the West Side of Lungchuan Fault. 2002 Annual meeting of China Geology Society, 7–99 (in Chinese).

Yu, S. B., Chen, H. Y., & Kuo, L. C. (1997). Velocity field of GPS stations in the Taiwan area. Tectonophysics, 274(1-3), 41-59.

Yu, S. B., & Kuo, L. C. (2001). Present-day crustal motion along the Longitudinal Valley Fault, eastern Taiwan. Tectonophysics, 333(1-2), 199-217.

doi: 10.6342/NTU202400130

Supplementary 1: Interferograms

Figure A.1: Ascending track

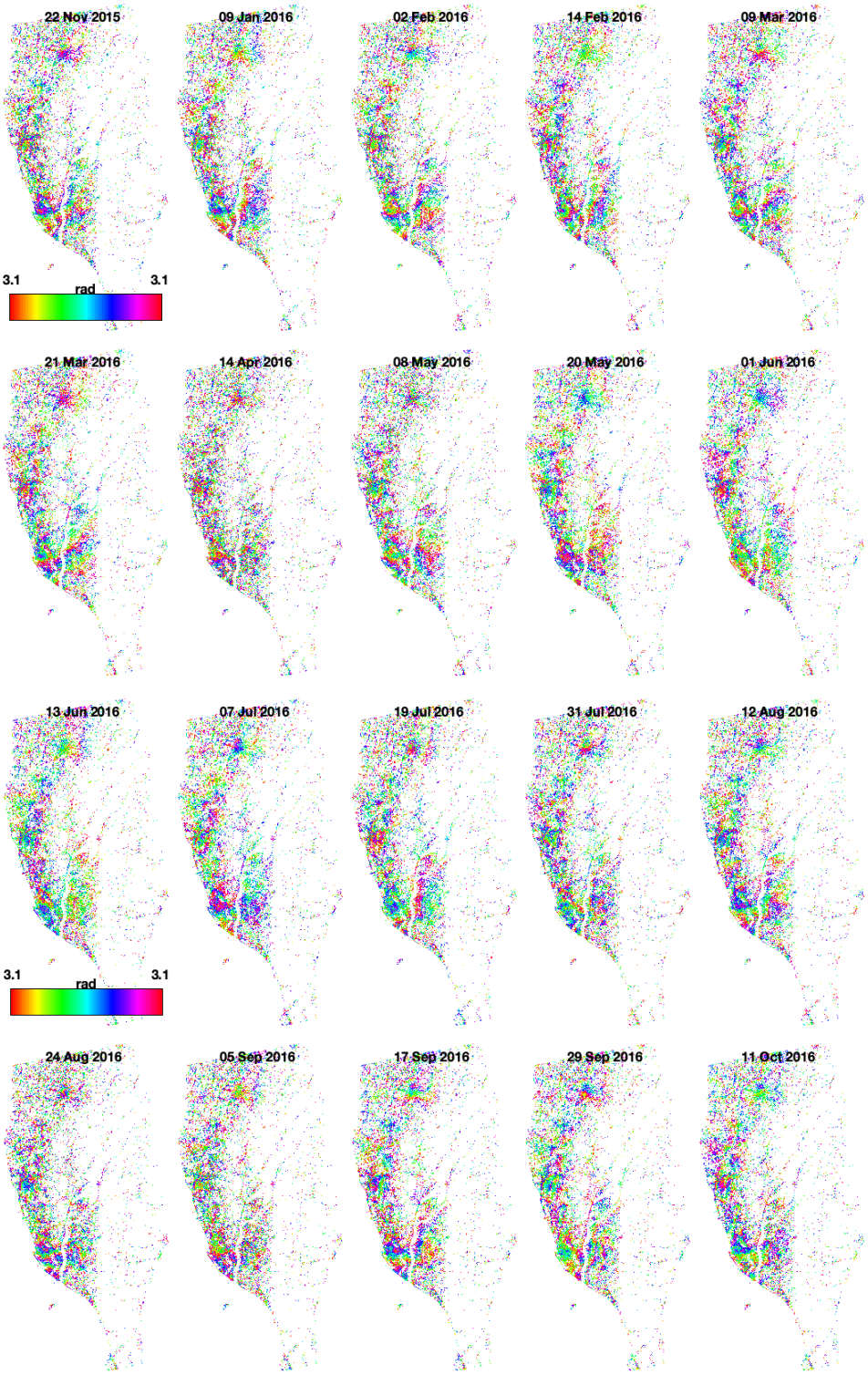

doi: 10.6342/NTU202400130

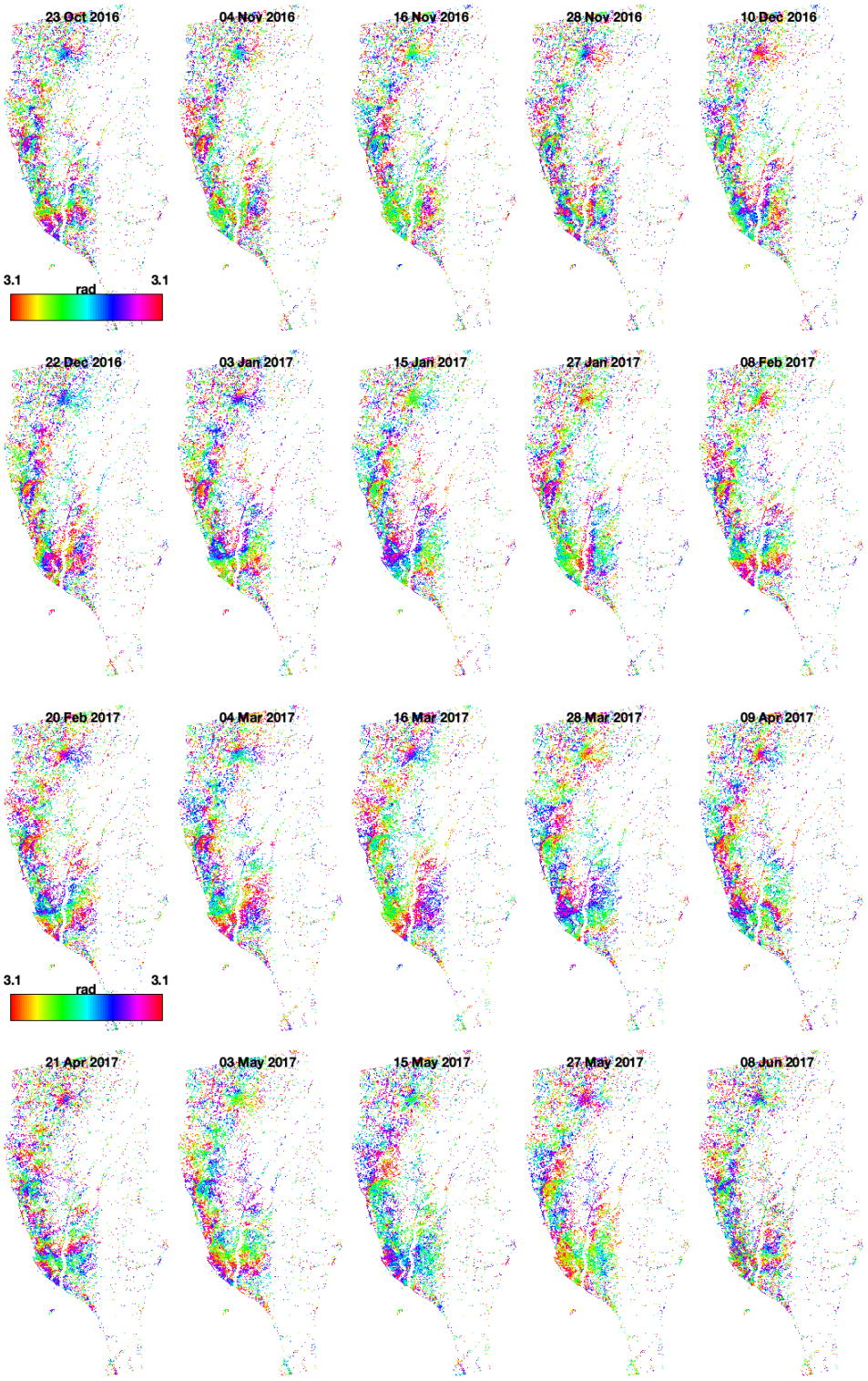

doi: 10.6342/NTU202400130

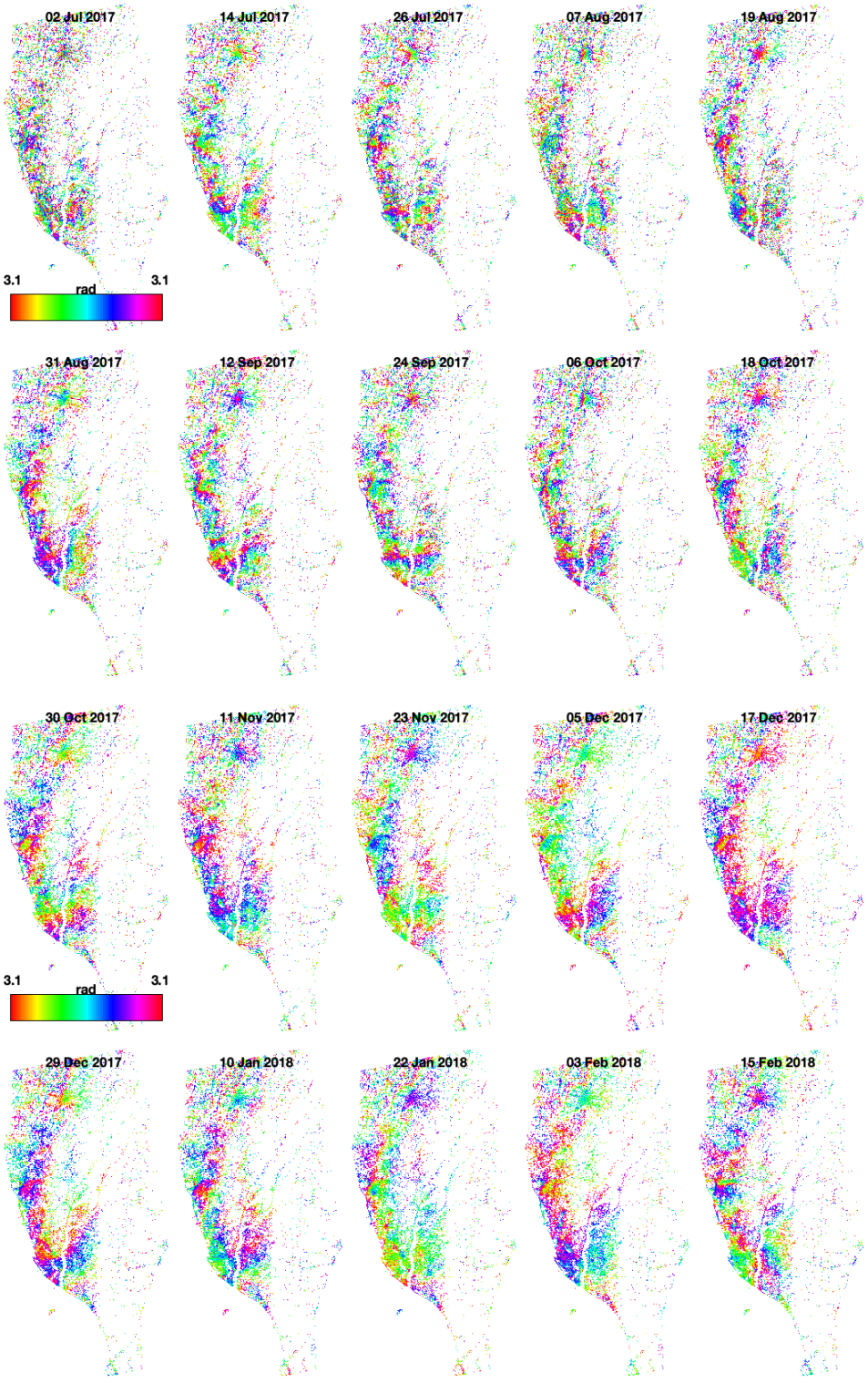

doi: 10.6342/NTU202400130

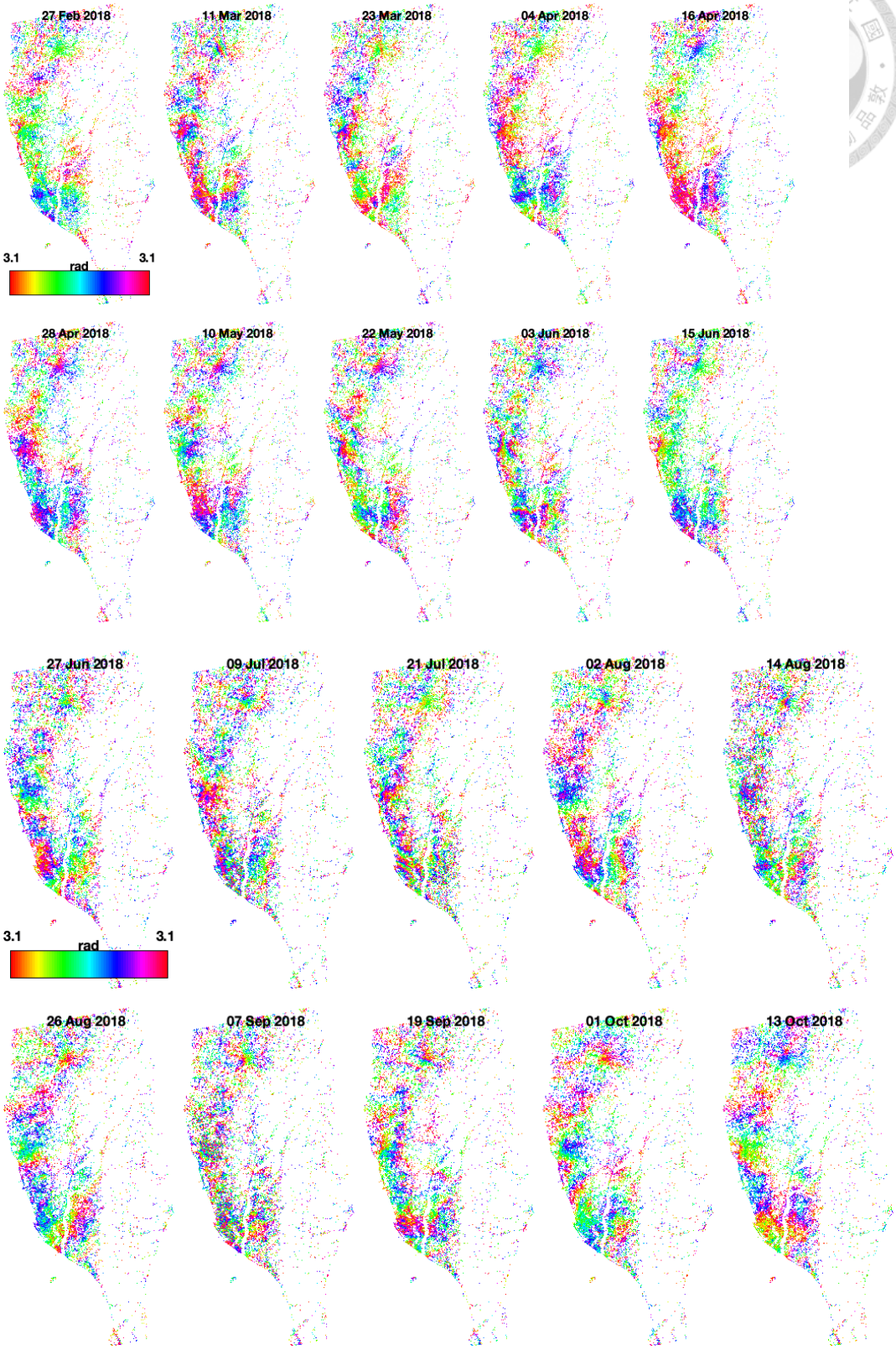

doi: 10.6342/NTU202400130

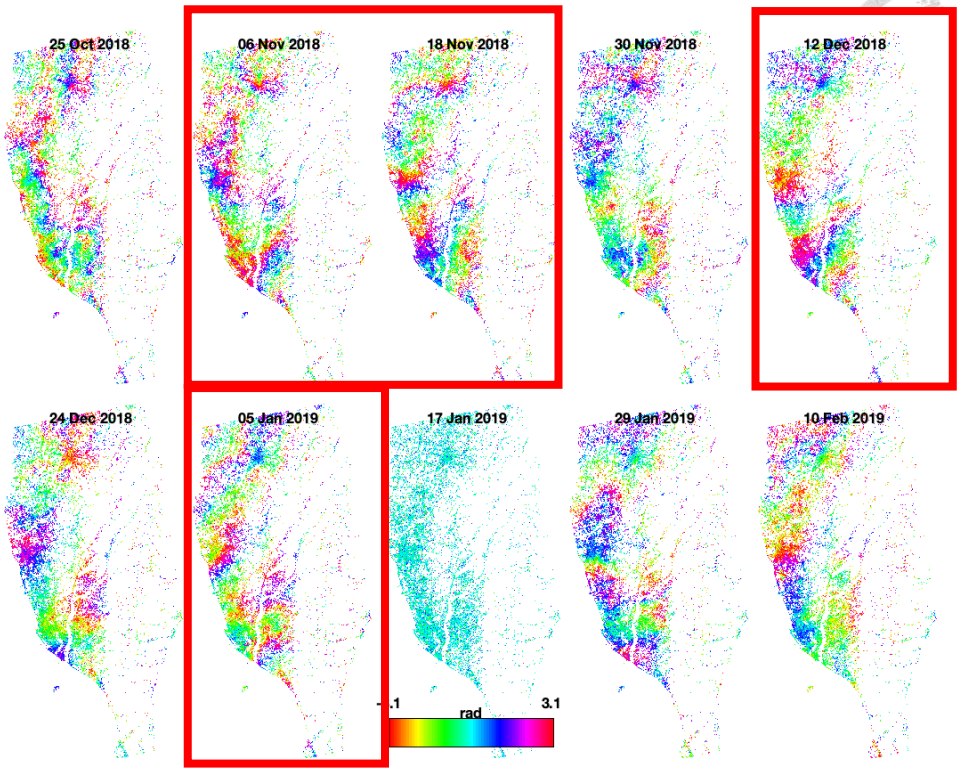

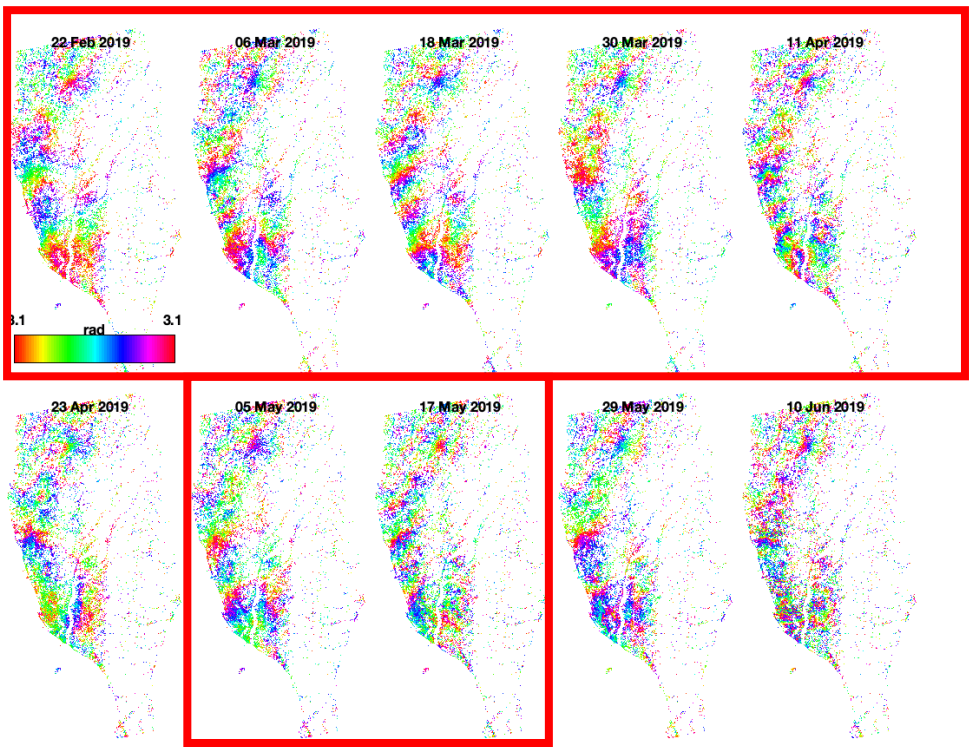

doi: 10.6342/NTU202400130

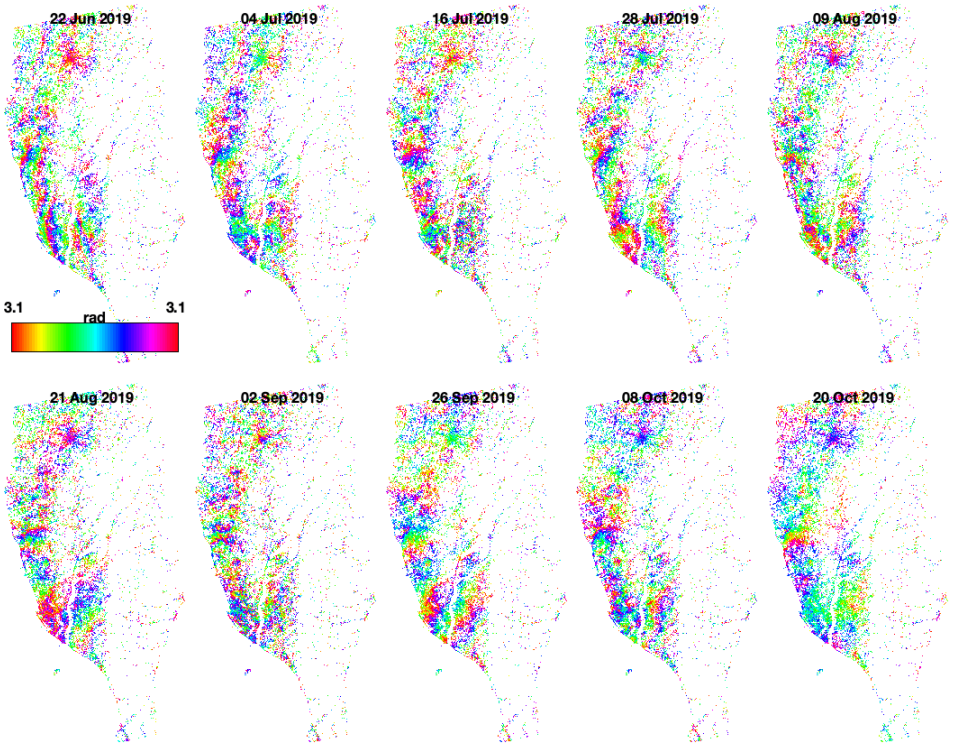

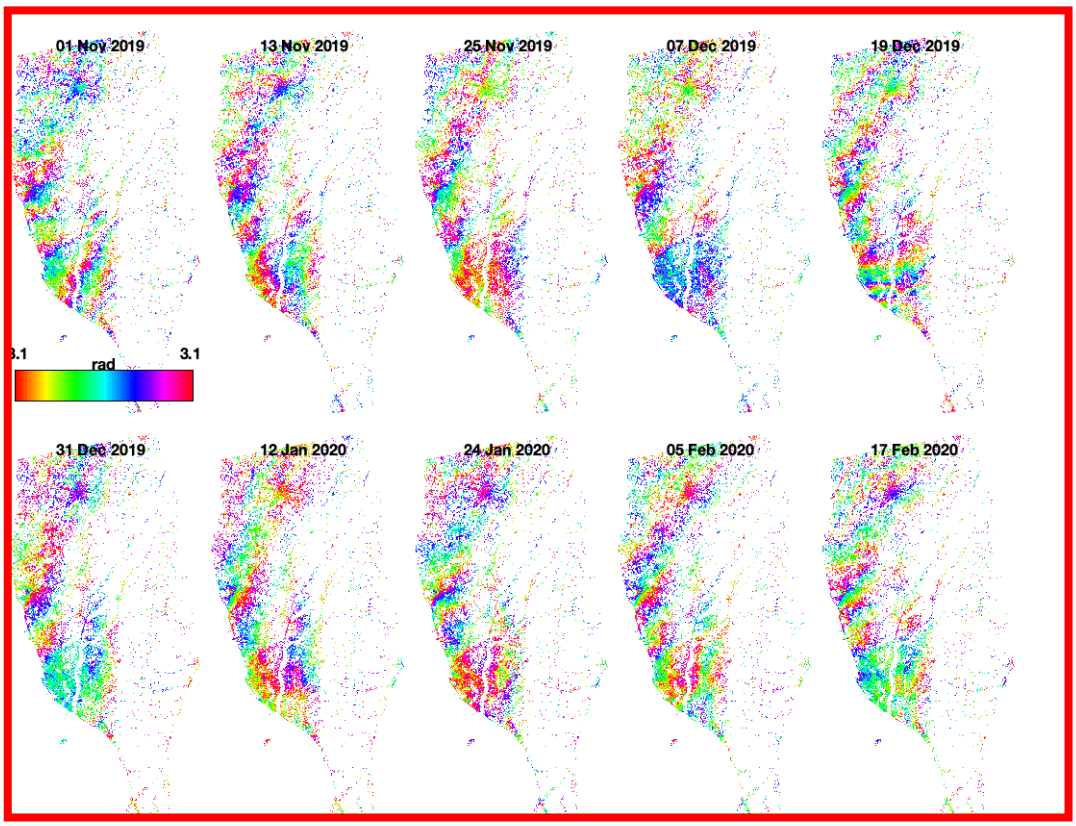

doi: 10.6342/NTU202400130

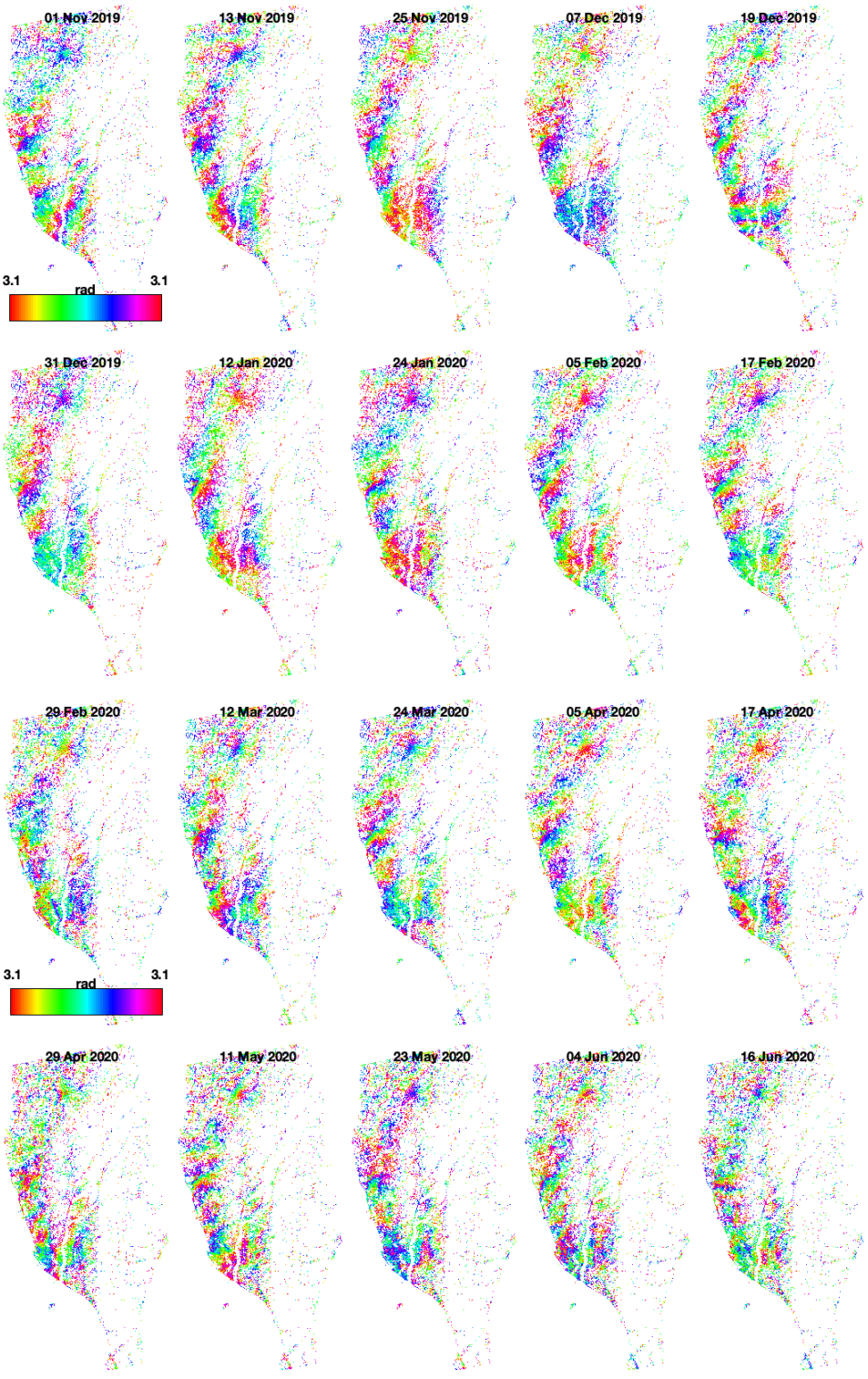

doi: 10.6342/NTU202400130

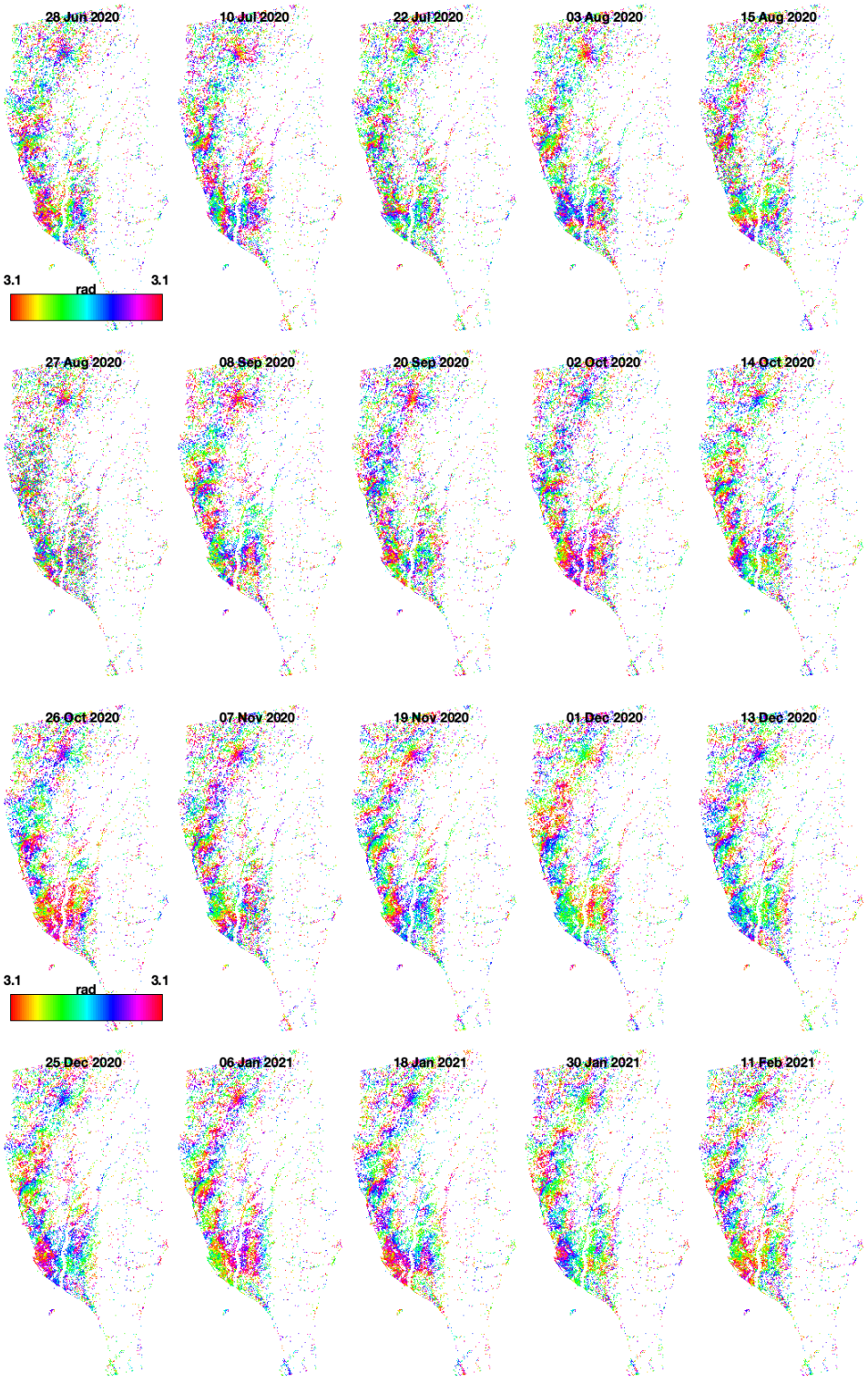

doi: 10.6342/NTU202400130

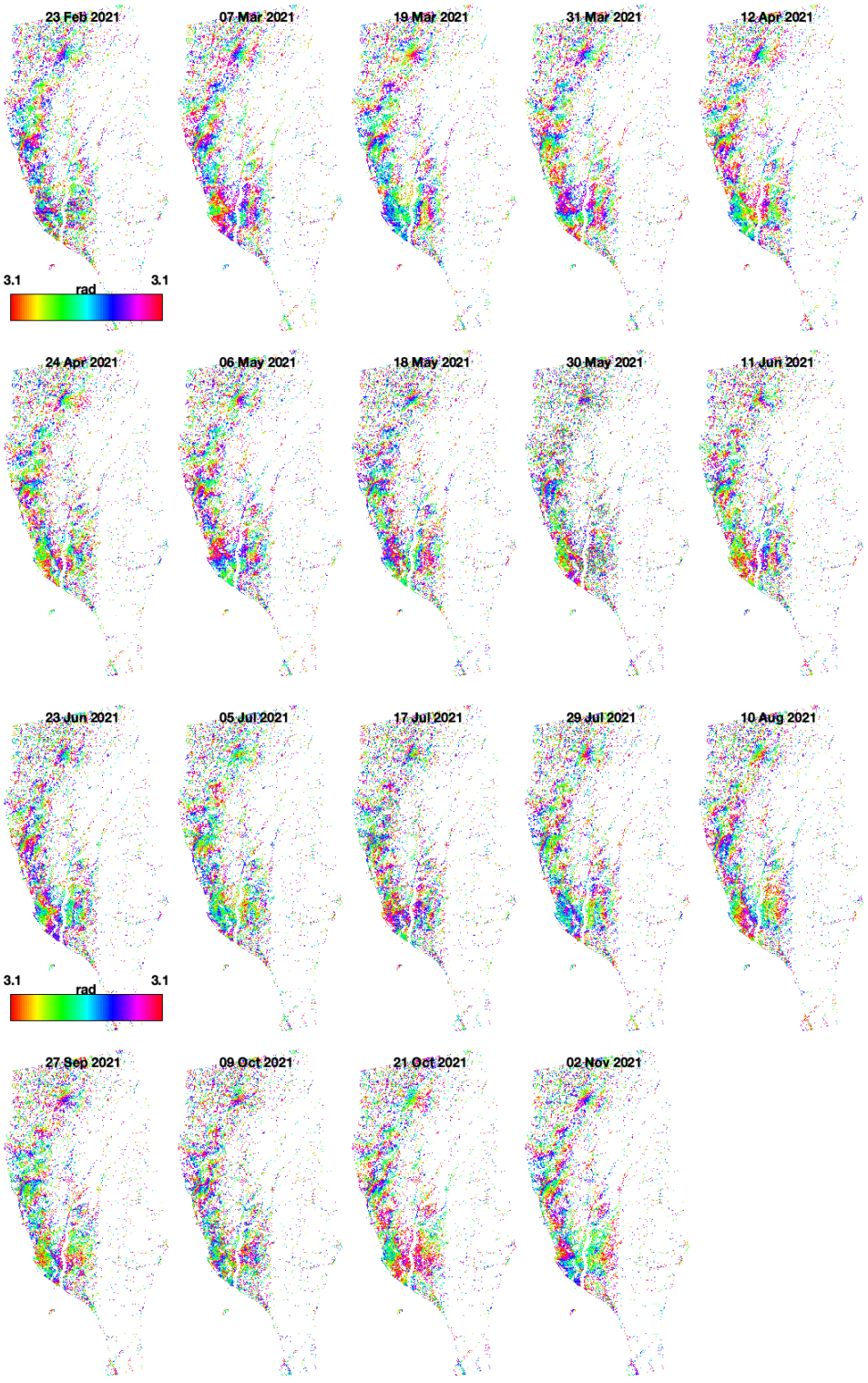

doi: 10.6342/NTU202400130

Fig. A.2: Descending track

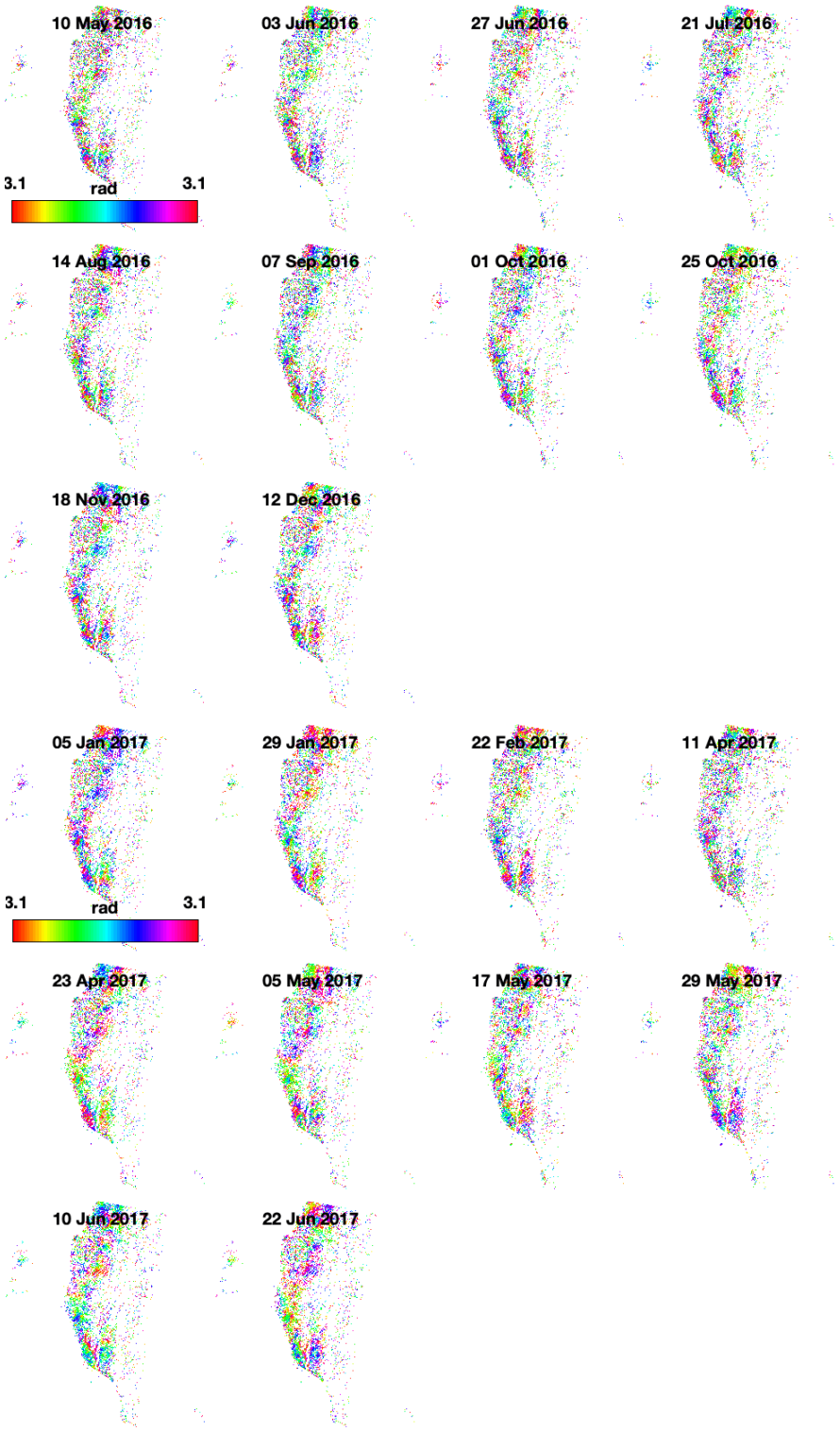

doi: 10.6342/NTU202400130

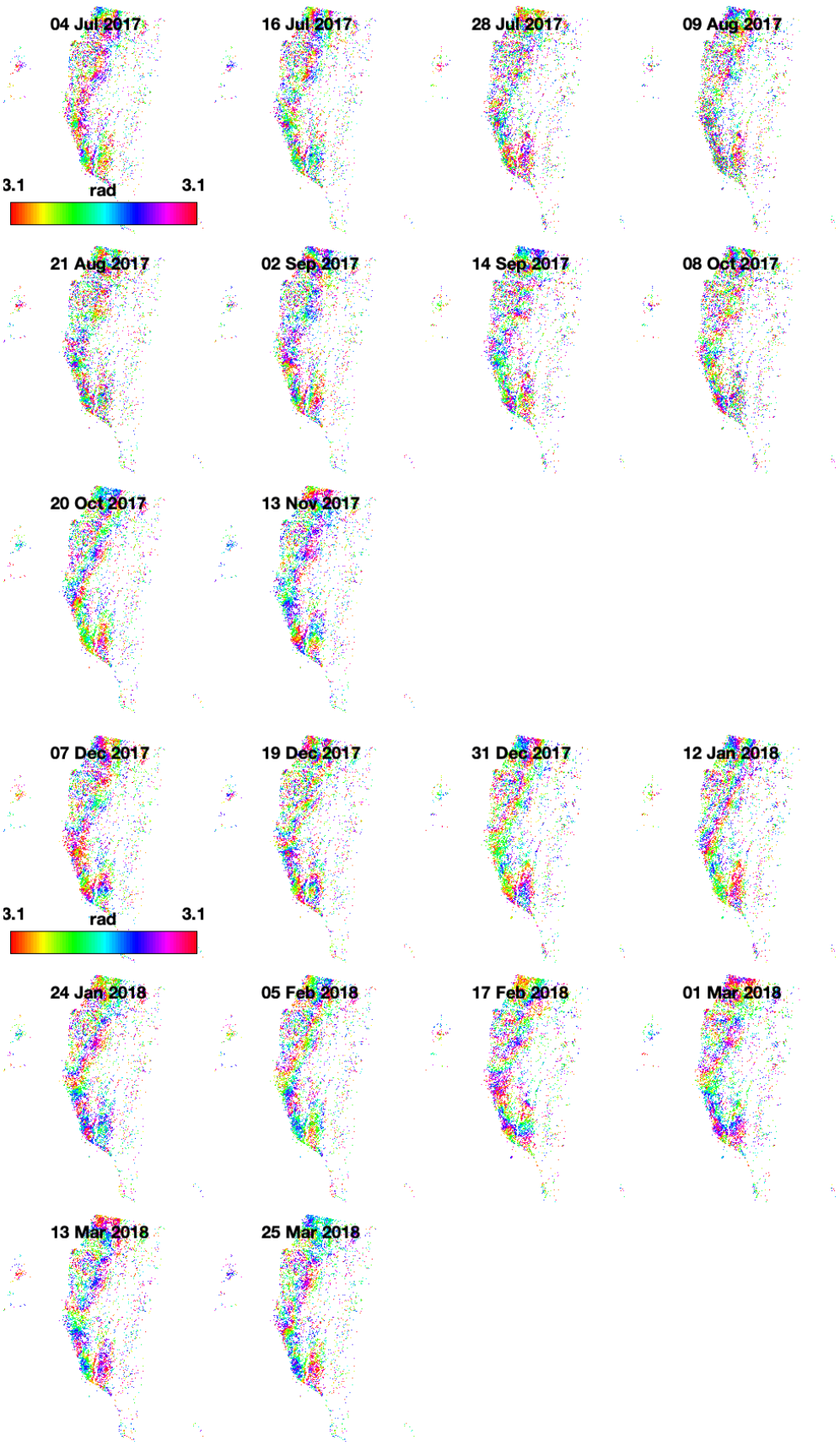

doi: 10.6342/NTU202400130

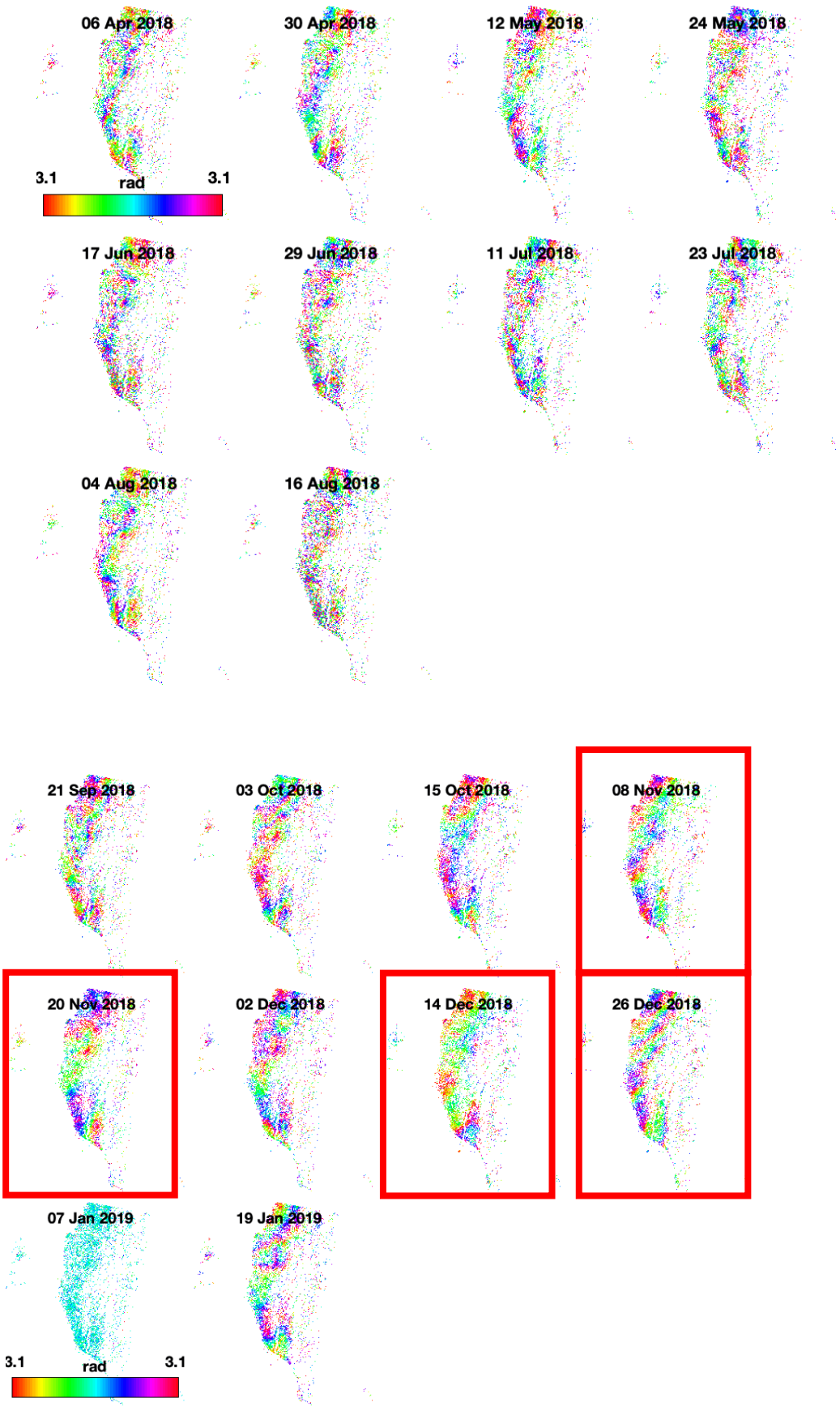

doi: 10.6342/NTU202400130

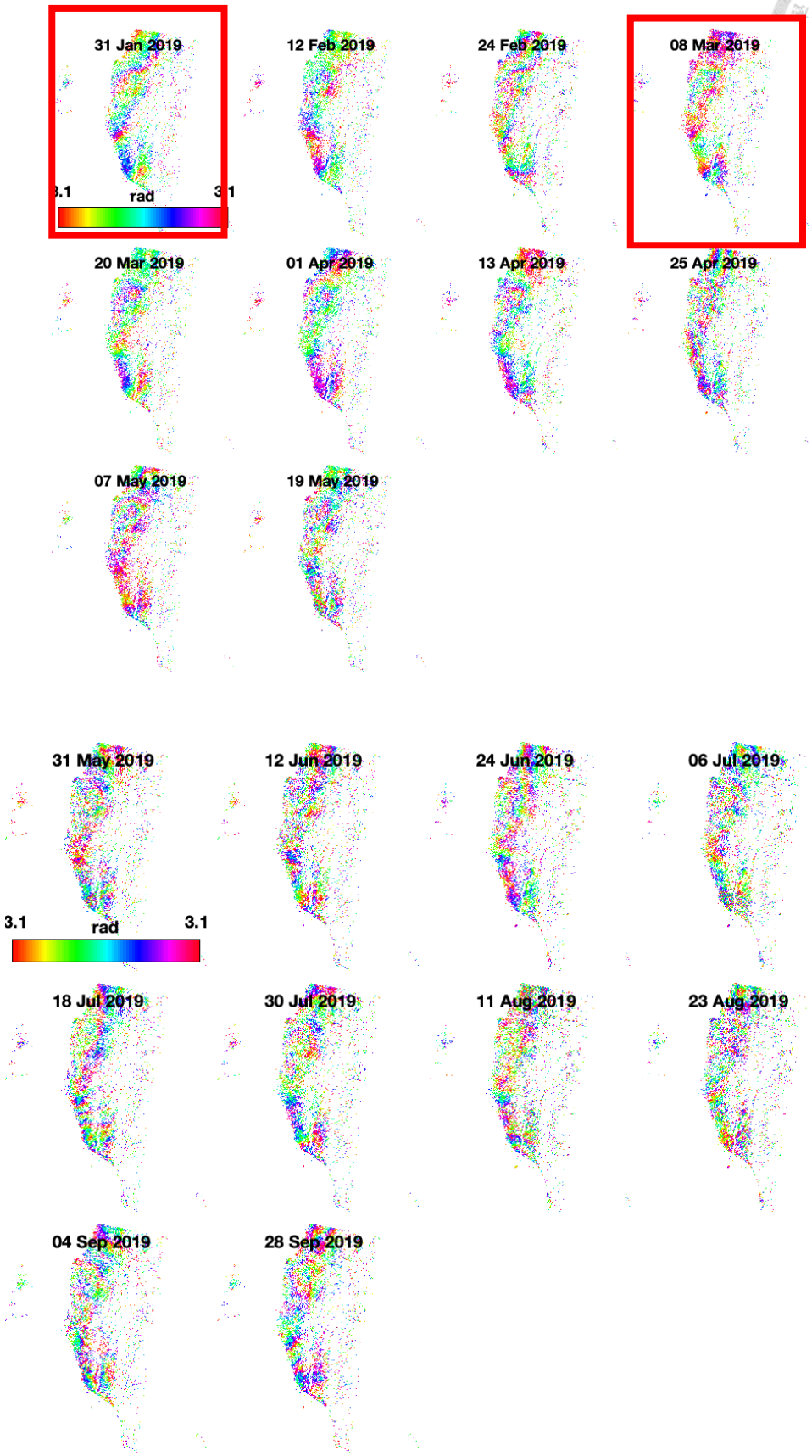

doi: 10.6342/NTU202400130

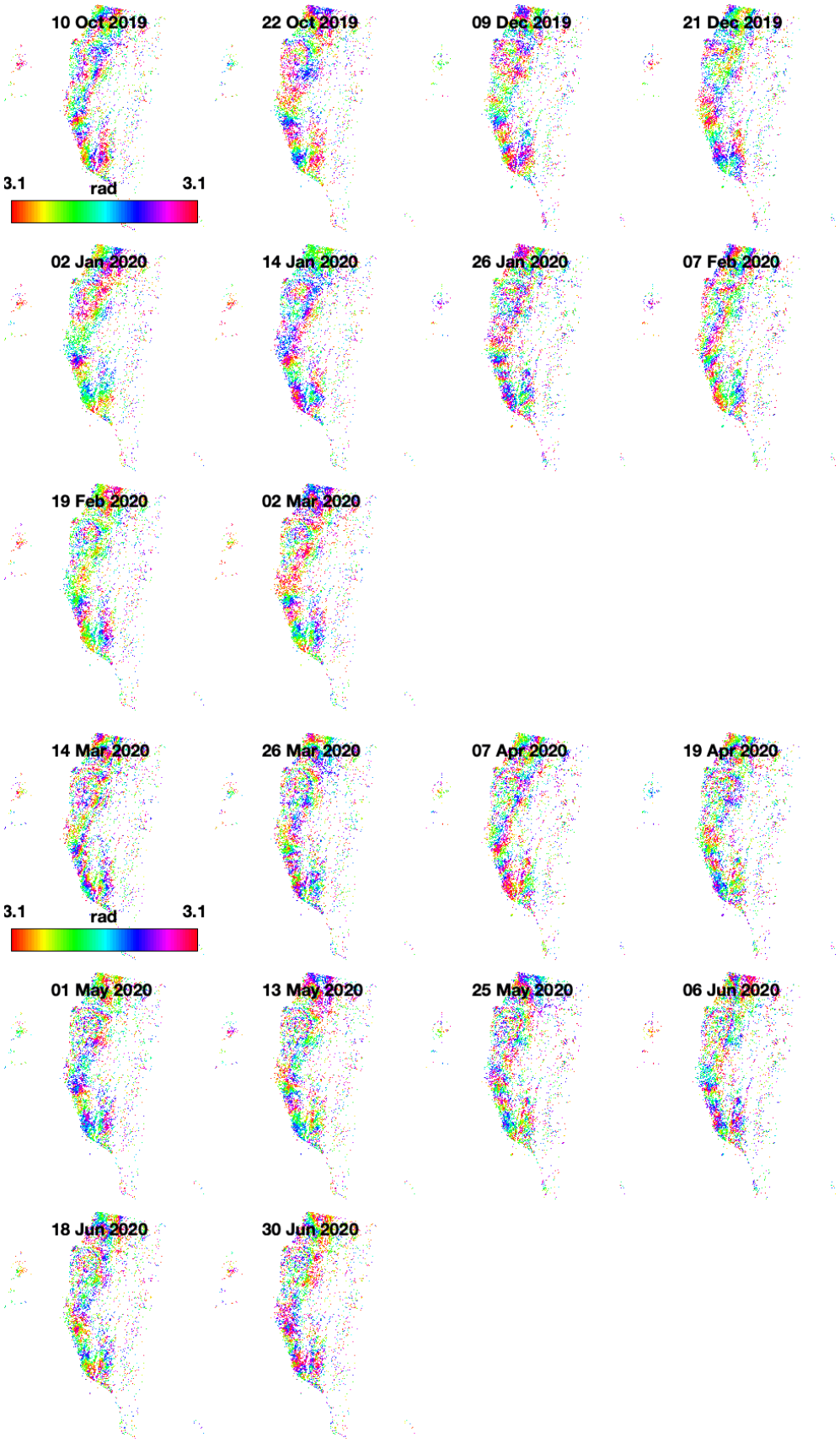

doi: 10.6342/NTU202400130

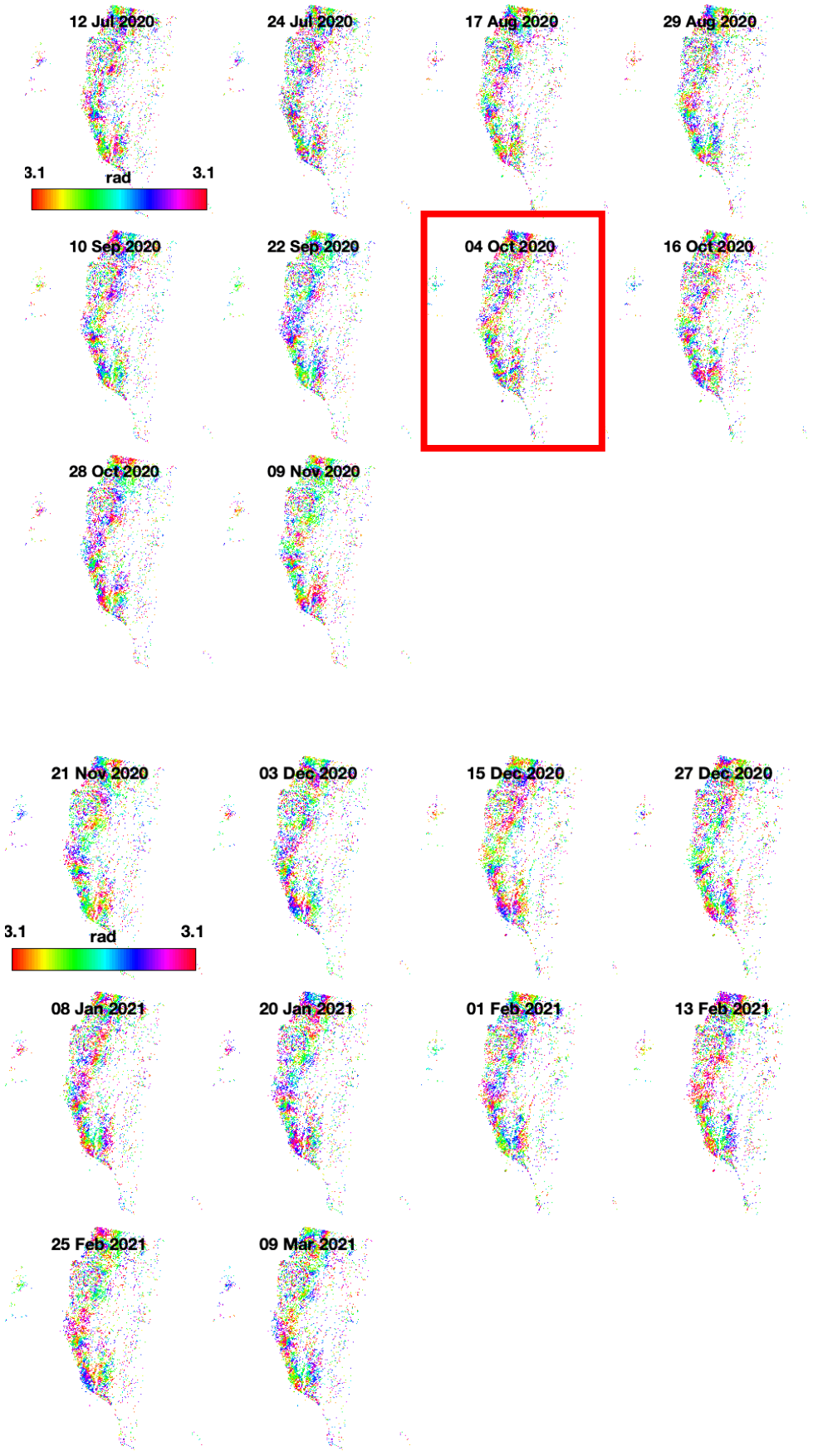

doi: 10.6342/NTU202400130

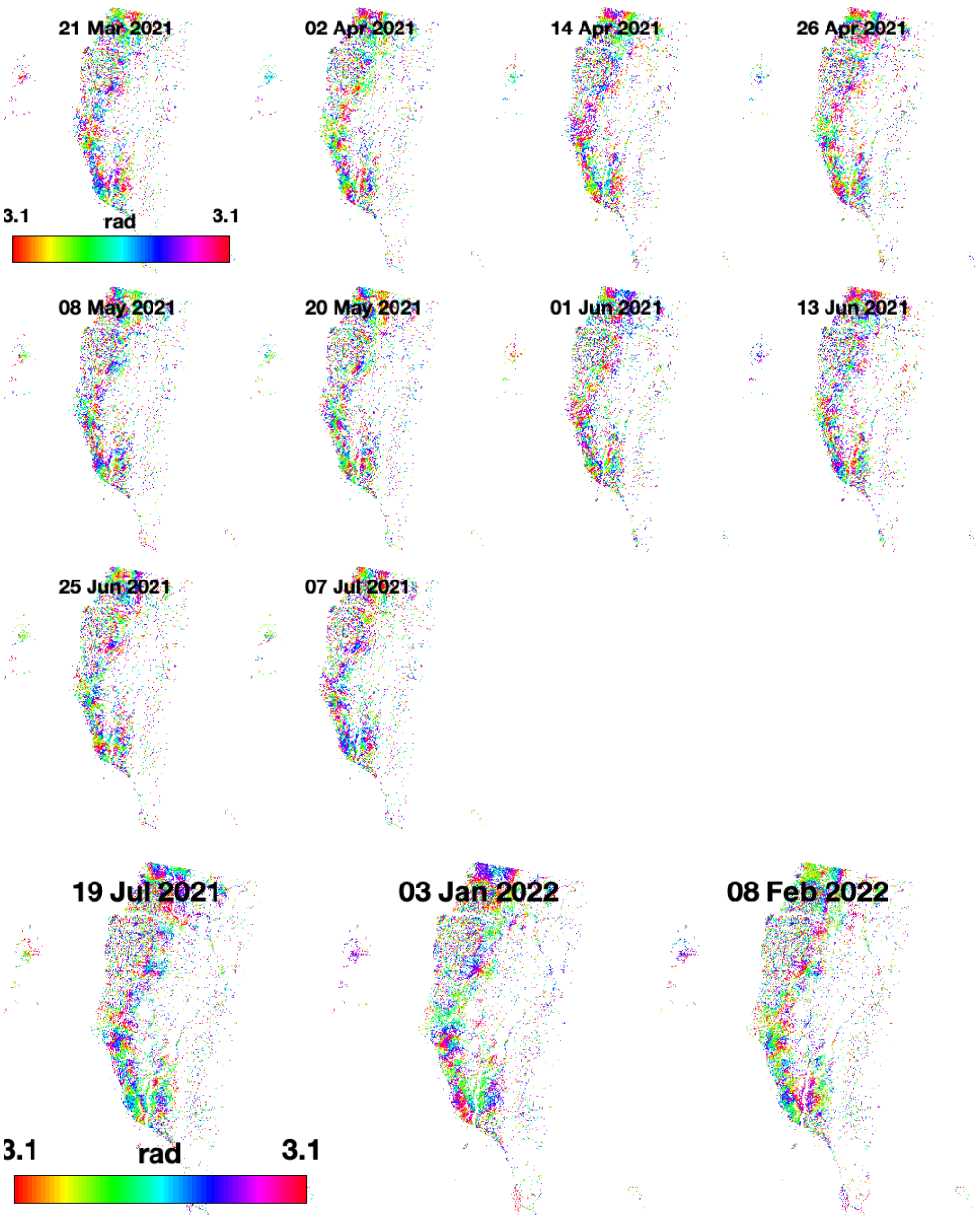

doi: 10.6342/NTU202400130